AN EXPERIMENTAL STUDY OF THE FORWARD GUIDE VANES OF AN ENGINE BYPASS NACELLE FOR LOW-BOOM SUPERSONIC FLIGHT

BY

ARTHUR ANGELO HERRERA

THESIS

Submitted in partial fulfillment of the requirements
for the degree of Master of Science in Aerospace Engineering
in the Graduate College of the
University of Illinois at Urbana-Champaign, 2011

Urbana, Illinois

Advisers:

Professor Michael B. Bragg
Professor Gregory S. Elliott

Abstract

Current FAA regulations limit the speed of civilian passenger jets to subsonic or transonic speeds due to the effects of the sonic boom produced by aircraft during supersonic flight. An engine nacelle design has been proposed that removes low-quality flow from the engine core and reduces the signature of the sonic boom caused by the external protuberances of a traditional engine housing. This new concept incorporates an outer nacelle surrounding the asymmetric engine surface, which creates a highly-complex, secondary bypass flow. Due to the complexity of the flow within this region of the engine, an experimental study has been conducted on the integration of guide vanes within the subsonic portion of the bypass region as the flow is diverted around a partial annular blockage. A wind tunnel facility at the University of Illinois at Urbana-Champaign accommodates an approximately 1/6th scale model that simulates the three-dimensional flowfield around the engine components. In order to observe the influence of the guide vanes on the overall flow quality, tests were also conducted on a model without forward vanes.

Pressure data were collected upstream and downstream of the guide vanes at several axial locations, with high resolution in both the azimuthal and radial directions. In addition to flow speed, flow direction was also analyzed via a five-hole multi-directional probe and surface flow visualization techniques. Experimental flow analysis in this study was conducted to support computational models and to provide insight into techniques that may further improve the flow characteristics within the bypass flow region. Results from the study indicate upstream flow uniformity due to the presence of the guide vanes as well as highly-complex flow features downstream of the vanes.

Acknowledgements

A variety of people have been my backbone of support during my graduate studies. First, I would like to acknowledge and thank my two advisers, Professor Michael Bragg and Professor Gregory Elliott, for accepting me into their group and giving me the opportunity to work on such an exciting project. Their knowledge, guidance, and support are tremendously appreciated. This project was supported by both Gulfstream Aerospace Corporation and Rolls-Royce Plc. Thank you to Tim Conners, Tom Wayman, and Robbie Cowart from Gulfstream and John Whurr from Rolls-Royce for their assistance on this project. I would like to acknowledge the SURGE Fellowship Program as well as the Illinois Space Grant Consortium for their additional support of my research. Also, thank you to my friends and fellow group members for offering their insight and collaboration during the last two years as well as undergraduate, Jason Hewkin, for his assistance during the summer of 2010.

Last, but not least, I would like to thank my family. My wife and best friend, Kelli, has always been the source of my confidence and determination. Her love and encouragement have been priceless over the years and this work could not have been completed without her by my side. Our parents and families have also been a tremendous source of support and love and, for that, I am deeply grateful.

Table of Contents

List of Tables

List of Figures

Nomenclature

Symbols

a	Speed of Sound
A	Cross-sectional area -or- Flow variable matrix (5-hole probe)
$C_{\alpha/\beta}$	Pitch/yaw angle pressure coefficients (5-hole probe)
C_o	Total pressure coefficient (5-hole probe)
C_p	Static pressure coefficient
C_q	Static pressure coefficient (5-hole probe)
K	Five-hole probe calibration constant
$\dot{m}$	Mass flow rate
M	Mach number
P	Pressure
R	Radius -or- Gas constant
q	Dynamic pressure
T	Temperature
U	Uncertainty
V	Velocity
x	In-plane horizontal direction -or- Placeholder variable
y	In-plane vertical direction

Greek Symbols

α	Pitch angle
β	Yaw angle
γ	Ratio of specific heats
θ	Azimuthal component
ρ	Density
σ	Standard deviation

Superscripts

$*$	Nondimensionalized variable
$\bar{}$	Average value

Subscripts

amb	Ambient conditions
i	Index value
inner	Inner wall of the test annulus
non	Nondimensionalized variable
outer	Outer wall of the test annulus
r	Radial component
t / o	Total/stagnation conditions
US	Upstream
∞	Freestream conditions

Acronyms

AC	Alternating Current
A/D	Analog-to-Digital
ARL	Aerodynamics Research Laboratory
CAD	Computer-Aided Design
CFD	Computational Fluid Dynamics
DARPA	Defense Advanced Research Projects Agency
ESP	Electronically-Scanned Pressure
FAA	Federal Aviation Administration
GAC	Gulfstream Aerospace Corporation
GPIB	General Purpose Interface Bus
MP	Measurement Plane
NPT	National Pipe Thread
PCU	Pressure Calibration Unit
PVC	Polyvinyl Chloride
QSJ	Quiet Supersonic Jet
QSP	Quiet Supersonic Platform
SDU	Scanner Digitizer Unit
SEI	Serial Encoder Interface
SLA	Stereolithography Apparatus
SLS	Selective Laser Sintering
SSBD	Shaped Sonic Boom Demonstrator
RSS	Root-Sum-Square
VFD	Variable Frequency Drive

Chapter 1

Introduction

Recent advancements in aerospace technology are leading toward allowing commercial aircraft to travel twice as fast and in half the time. Since the formation of modern air transportation, and even with the advent of the modern jet engine, aircraft have largely been limited to flying at subsonic speeds. As technology continued to advance and allowed for faster flight speeds, regulations have restricted civil transport aircraft from reaching the speed of sound and have limited them to cruising at speeds in the transonic regime. Modern commercial aircraft have been designed accordingly to approach sonic conditions and to reap the benefits of high-speed travel without the detrimental effects of supersonic flight, which include increased drag, decreased lift-to-drag ratio, and the unsteady aerodynamic effects of shock waves. In addition to the performance-related consequences of supersonic flight, it also has been plagued by the negative effects of the sonic boom. Therefore, boom suppression technologies have been at the forefront of supersonic aerodynamic research and one such technology has motivated the present experimental study.

1.1 Background

A sonic boom is formed by the compression of air by a body moving at supersonic speeds. Because pressure waves travel at the speed of sound, disturbances are propagated upstream of a subsonic body so that the incoming flow can be gradually redirected around the object. For a body moving at supersonic speeds, disturbances created by the object are unable to propagate upstream and, therefore, coalesce into a three-dimensional wave front known as a Mach cone (see Fig. 1.1). Immediately upstream of this Mach cone, the ambient fluid has no knowledge of the supersonic disturbance. Downstream of the wave front, the fluid is diverted in order to compensate for the air volume displaced by the

supersonic body, or, relating to this study, the supersonic aircraft.[1] The resulting increase in air pressure across the oblique shock wave is commonly referred to as an overpressure. Along the length of the aircraft, the air is continuously expanded and, at the tail, a large jump in pressure is required to return to the ambient conditions. Shown in Fig. 1.2 is the evolution of downward pressure distribution created by a supersonic aircraft. Due to its characteristic shape in the far-field, the resulting pressure signature is known as an N-wave and represents the primary double boom associated with supersonic aircraft.[2,3] The magnitude of the resulting N-wave is known as the overpressure magnitude and is commonly measured in units of pounds per square foot (psf).

In addition to the characteristic N-wave created by an aircraft in supersonic flight, the Mach cone creates an upward boom signature that is typically dampened through the atmosphere. This portion of the sonic boom is known as the secondary or "over-the-top" boom and, in certain atmospheric conditions, can be directed back toward the ground to produce low-frequency disturbances, such as vibration or a rumbling effect. This secondary boom is less-likely to be associated with supersonic flight; nevertheless, the over-the-top boom remains a topic of concern due to its focused impact on indoor observers.[4]

Since the 1950's, after the first supersonic flight by the Bell X-1, the effects of the primary sonic boom have been a prime focus of research. Not only were boom signatures found to cause discomfort and annoyance to casual observers, they also had the potential to cause damage to structures on the ground.[3] Several studies were conducted through the 1960's that focused on surveys of sonic boom observers and the acceptability of overpressure magnitudes, including the Oklahoma City sonic boom tests. Initial findings suggested that overpressures of 1 to 1.5 psf were acceptable levels for occasional sonic booms.[2,5] However, if flights within the supersonic regime become customary, a substantially lower overpressure would be required for areas inundated with over-land supersonic flights due to the annoyance factor associated with repeated sonic booms.

As a result of the effects of the sonic boom, the Federal Aviation Administration (FAA), as well as corresponding agencies around the world, have prohibited over-land flight of supersonic civilian aircraft, due primarily to the noise effects of the boom signature. In fact, when the Concorde completed commercial flights, it achieved

supersonic speeds only over bodies of water and maintained subsonic speeds during flight above land. While this allowed portions of its flights to achieve supersonic speeds, the over-land restrictions effectively limited the Concorde's operation to trans-oceanic flight paths. To support future changes in FAA regulations, research has been focused toward developing boom shaping technologies, which are aimed at lowering the overpressure magnitude of the N-wave signature and increasing the effective rise time of the initial compression wave, both of which have been shown to decrease the overall noise impact of a sonic boom.

1.2 Boom Suppression Technologies

Prior to 2003, boom shaping technologies had only been demonstrated in wind tunnel tests and computational fluid dynamics (CFD) simulations. In 2003, the Defense Advanced Research Projects Agency's (DARPA) Quiet Supersonic Platform (QSP) program developed and tested a modification to an F-5E aircraft, which was known as the Shaped Sonic Boom Demonstrator (SSBD). By specifically modifying the nose of the aircraft, the goal of this flight demonstrator was to reduce the magnitude of the initial boom overpressure by creating a flat-top boom signature.[2,4,6] Shown in Fig. 1.3c is a comparison of the boom signatures of both the un-modified F-5E and the SSBD, which demonstrates a significant reduction in the overpressure magnitude of the boom. The figure also depicts the difference in nose shape between the two test aircraft. This study proved that results from CFD and wind tunnel studies were valid in predicting boom attenuation in true atmospheric flight.

Amidst recent efforts to pursue boom attenuation technologies, Gulfstream Aerospace Corporation (GAC) has made progress toward several technologies to provide a less-intense boom signature on a supersonic business jet. Presented in Fig. 1.4 is an overall concept of an 8-passenger Quiet Supersonic Jet (QSJ), which incorporates slender fuselage and engine designs as well as wings with variable sweep capabilities.[7] Two of the primary boom attenuation technologies to be incorporated with the QSJ concept include the Quiet Spike™ and a novel engine inlet design.

The Quiet Spike™ design is a telescoping nose that remains retracted during subsonic flight and extends during supersonic flight. The primary goal of the Quiet Spike™ is to shape the overpressure signature so that the initial compression is distributed among several smaller shocks rather than a large, concentrated shock.[8,9] In effect, this achieves both goals of boom shaping by decreasing the magnitude of the overpressure as well as lengthening the time over which the air experiences the initial compression. Shown in Fig. 1.5 is a prototype of the Quiet Spike™ installed on an F-5 aircraft, along with its corresponding boom signature. This superposition illustrates the spatial distribution of downward, near-field disturbances created by the aircraft components and demonstrates the series of three small compressions formed prior to the fuselage radome. Note the large pressure magnitudes, which are due to the vertical proximity of the readings to the aircraft (approximately 95 feet). These values would be reduced significantly as the boom signature propagated toward the ground.

The second boom suppression technology used in the QSJ concept is an innovative design for the engine inlet geometry, which uses relaxed isentropic compression to better condition the flow as it encounters the turbofan inlet plane.[10,11,12,13] Not only does this inlet design aid in the deceleration of the engine core flow to subsonic speeds, it also acts to capture low-quality flow within a secondary annular bypass duct. The removal of poor-quality flow is an important feature of this novel inlet design, since engine performance is negatively affected by high levels of flow distortion at the fan inlet plane. Preliminary studies of the relaxed isentropic compression inlet indicated a high level of flow distortion near the outer wall of the core flow region. Therefore, by carefully tailoring the placement of the engine bow shock to terminate at the external cowl lip of the engine nacelle (see Fig. 1.6), the low-quality flow can be directed to and captured within a secondary annular flow path independent of the engine core flow.[14,15,16] Not to be confused with the standard bypass flow associated with turbofan engines, the resulting subsonic, secondary bypass flow is formed by the external cowling that encircles the primary engine cowling and is the focus of the current study.

Due to their potential effects on the cowl/shock interaction at the bypass inlet, the mass flow rate through the bypass region and the uniformity of the upstream flow are both critical aspects of the bypass nacelle design. By maximizing the mass flow rate through the

bypass, flow spillage will be reduced at the nacelle inlet plane, which aids in positioning the bow shock on the leading edge of the nacelle. This effect is aided by ensuring a uniform flowfield around the circumference of the nacelle inlet, which, at the same time, minimizes distortions to the core engine flow. While the beneficial effects on the upstream shock structure are important, so too are the losses incurred through the bypass flow. Therefore, in addition to characterizing the upstream flow characteristics, the flow behavior throughout the entire bypass region is critical to the overall nacelle design.[14,15,16]

By comparing this proposed nacelle design with a traditional nacelle design in Fig. 1.7, the secondary cowling also acts to reduce the complexity of the engine surfaces exposed to the freestream flow. In supersonic flight conditions, shocks tend to form on sharp surfaces or in areas with large changes in cross-sectional area. Therefore, the long, slender design of the outer nacelle aims to reduce the development of shocks along the length of the engine, in addition to its main goal of capturing the low-quality portion of the engine inlet flow. Difficulties arise within the bypass region due to the complexity of the underlying engine surface exposed within the annular flow region. As seen from the engine's laser scan in Fig. 1.7, there are many components around the circumference of the engine that would obstruct the flow and reduce overall flow performance through the secondary bypass region.

1.3 Research Motivation

With a large portion of the engine components located along the underside of the engine, a fairing was designed to isolate the "gearbox" component and redirect the flow around this obstructed region. Because the resulting blockage was designed to occupy 160 degrees of the flow annulus, simply contracting and diffusing the flow around the gearbox component would create a substantial separation/recirculation region aft of the blocked region, as seen in preliminary bypass studies completed by Yeong and Chiles.[17,18,19,20] Therefore, guide vanes were designed by GAC for integration forward and aft of the primary blockage component to increase mass flow rate through the bypass duct, improve uniformity of the upstream flow, and minimize total pressure losses through the system. A CAD model of the overall engine design can be seen in Fig. 1.8. This illustration depicts

the general orientation of the forward and aft guide vanes with respect to the gearbox fairing. Fig. 1.9 also presents the geometry and placement of the vanes in an unwrapped view of the bypass region and illustrates the differences between the forward and aft guide vane structures. The forward vanes were designed to be very thin to provide uniform flow acceleration through the forward bypass region. The aft vanes varied in thickness according to a quasi-one-dimensional analysis to reaccelerate the exhaust flow to match the supersonic freestream.[12,13] Between the two sets of guide vanes, where the flow annulus is most obstructed, the unvaned region allows the flow to readjust after exiting the forward vanes and before entering the aft set of vanes.

Early computational studies were completed on a preliminary bypass design, which examined the flow through the bypass flow region and did not incorporate guide vanes in the geometry. One such study by Chima investigated the effect of the bypass concept through various stages of flight and confirmed the benefits of removing low-quality flow from the core engine flow.[21] Full-engine computational simulations have most recently been performed by Kim with the goal of characterizing the bypass flowpath with integrated guide vanes.[13] Kim has also conducted preliminary studies aimed at optimizing and tailoring the vane geometry for improved inlet performance.[12] Such studies have further confirmed the effectiveness of the guide vanes in the bypass region to improve the performance of the engine core flow and to tailor the position of the upstream bow shock.

To provide an experimental validation of the existing computational models, the current study focuses on the characterization of pressure, speed, and directionality flow features associated with the forward set of guide vanes within the secondary bypass flow. Parallel experimental and computational studies have also been completed at Illinois that focus solely on the flow within the aft set of guide vanes.[22,23] Therefore, all portions of the bypass flowpath will be represented, starting with the bypass inlet plane and continuing through the exhaust.

1.4 Objectives and Approach

The goal of this study is to understand the effect of introducing forward guide vanes within a secondary bypass flow for a novel engine nacelle concept. By providing a better

understanding of this region of the flow, the overall nacelle design can more easily be integrated with the remainder of GAC's proposed quiet supersonic jet. Therefore, the objectives of the current study are as follows:

1. Measure the flow quality and uniformity upstream of the forward guide vanes at the bypass inlet plane.
2. Understand the complexity of the flow as it exits the forward guide vanes and approaches the aft guide vanes and examine its impact on the overall bypass flow.
3. Provide data to support existing and future computational bypass flow simulations.
4. Provide in-flow conditions to the parallel experimental study of the aft guide vanes.

For this study, both a vaned and unvaned model geometry were examined to fully assess the effect of the guide vanes within the bypass flow region. To examine the upstream flow, total and static pressures were collected to measure the azimuthal speed distribution across the flow annulus. Downstream of the guide vanes, total and static pressures were measured to determine speed and loss characteristics of the flow. Additionally, five-hole probe and surface flow visualization data were collected to further evaluate the complexity of the flow as it propagated toward the aft guide vanes.

To achieve the objectives outlined above, this thesis will provide details about the experimental facility and bypass model as well as the data acquisition capabilities of the wind tunnel test section. Then, a detailed analysis will be completed on the collected data and a discussion will follow that highlights interesting features of the flowfield. Finally, a brief summary of the experimental study will be followed by a section that forms conclusions about the performance of the bypass flow design and makes recommendations for further research.

Chapter 2

Experimental Methods

This chapter details the facility used to complete the experimental study as well as the wind tunnel models used throughout the investigation. In addition to a physical description of the facility and models, data acquisition and data reduction methods are also described in detail, providing a comprehensive understanding of the process used to collect and interpret the experimental data.

2.1 Wind Tunnel

The experiments detailed in this study were conducted in the Aerodynamics Research Laboratory (ARL) at the University of Illinois at Urbana-Champaign. The laboratory facility houses two subsonic wind tunnels in a high-bay area, a separate control room with visual access to the tunnels, a supersonic gas dynamics lab and supersonic wind tunnel, and a small model shop utilized for basic machining needs. All testing of the engine bypass geometry was performed in a subsonic, axisymmetric, open-return wind tunnel facility developed exclusively for the current research.

2.1.1 Original Facility

At the onset of the current study, preliminary data had been acquired for low-speed, off-design conditions with an initial bypass model configuration. Since these initial measurements, however, a modification to the model geometry, coupled with the need for higher, on-design flow speeds, required some modification to the wind tunnel itself. Shown in Fig. 2.1 is a comparison of the original and modified facilities. The following section will briefly discuss the original components of the wind tunnel facility, some of which have been used again in the current study.

2.1.1.1 Test Section and Rotation

The axisymmetric test section used for this study was composed of three sections of aluminum tubing, totaling over 9 feet in length. These segments were internally honed to achieve an inner diameter of 11.1 inches, which was chosen based upon an approximate $1/6^{th}$ scale factor used to simulate the bypass model. Due to the complex annular geometry of the test region, the central portion of the test section was designed to rotate 360 degrees about the centerline axis. This rotational degree of freedom was put in place to allow full azimuthal access to the axisymmetric test region. When coupled with a linear traverse attached to the outer wall of the test section, which provided full radial range of motion, a pressure probe or other flow diagnostic device could access to the entire cross-sectional area of the test region.

To permit access to the annular flow region, the rotating portion of the test section wall incorporated two 3/4-inch ports for pressure probe access, where pressure profiles could be collected upstream and downstream of the model. At both probe access ports, a mounting mechanism was located along the outer surface of the test section, which enabled the traverse to move in a radial manner. In addition to the two probe access ports, 35 static pressure ports were positioned along the length of the rotating test section in 1-inch increments. Throughout a full rotation of the test section wall, these pressure readings provided measured surface pressures on the outer cowling of the bypass duct. This mapping of static wall pressures provided an indication of major trends in the flow, including apparent acceleration zones and/or separation regions.

To allow for rotation of the center segment of the test section, custom nylon bushings with sealing O-rings were mounted on the ends of the connecting test section segments. This design permitted the test section to rotate smoothly, while minimizing leakage at the segment junctions. Also, while all three segments of the test section were supported by portable frames, the frame for the rotating portion employed rollers to reduce resistance during rotation. In order to facilitate tunnel rotation during a given test, a large ring gear was attached to one end of the rotating segment and was driven by high-torque, geared stepper motor (See Section 2.3.2 for more details of the test section rotation capabilities). The original rotating test section can be seen in Fig. 2.2. While the above has provided brief description of the original test section and rotation capabilities,

additional details of the design, fabrication, and operation of the original test section can be found in Yeong.[18]

2.1.1.2 Tunnel Inlet

Upstream of the test section, the wind tunnel inlet design was designed to provide uniform incoming flow with low levels of freestream turbulence. With a contraction from a 78-inch square flow-conditioning section to the 11.1-inch diameter test section, the inlet accelerated the flow through a contraction ratio of approximately 63, over an axial distance of approximately 10 feet. At the largest cross-sectional area, where the flow velocities were the lowest, the inlet employed a 4-inch thick, expanded aluminum, honeycomb flow straightener and five stainless steel, turbulence reduction screens. Details of the design and construction of the inlet section can be found in Jacobs.[24]

2.1.1.3 Diffuser, Fan, and Controller

Immediately downstream of the aluminum test section, the original design of the wind tunnel required the cross-section to diffuse to accommodate the 48-inch diameter fan providing the mass flow for the experiments. These diffuser sections, totaling approximately 23 feet in length, were designed according to diffuser performance specifications established by Barlow, Rae, and Pope, and incorporated an equivalent half-angle of approximately 3.7 degrees.[25] The diffuser was fixed to the downstream segment of the test section, but utilized a vibration isolation connection at the fan interface to reduce the impact of the fan vibration on the test section. This connection used Ventglas®, a flexible, fiberglass-reinforced, neoprene fabric, to isolate the diffuser from any structural vibrations induced by the fan.

Downstream of the diffuser sections was a Joy Manufacturing, model 48-26½-1750, axivane fan, with an overall diameter of 48 inches. This single-stage fan was powered by a 100-hp General Electric AC motor and was designed to operate at a maximum rpm of 1750, while supplying 63,000 cfm of air flow and 0.27 psi of pressure recovery. Additionally, the motor/fan combination was controlled by an Eaton AF5000+ Dynamatic variable frequency drive (VFD), which allowed the fan to supply a wide range of flow speeds in the test section. While the VFD could be controlled locally with a built-in keypad, it was primarily operated using a VFD control terminal, which utilized an RS-

232 cable connection interface, allowing full control through a main data acquisition computer. Again, further details of the design of the diffuser sections and the fan/motor system can be found in Jacobs.[24] Fig. 2.1a illustrates the overall setup of the original wind tunnel, including the tunnel inlet, test section, diffuser, and axial fan.

2.1.2 Modified Facility

In order to achieve a more representative flow speed for the bypass design, and to accommodate an updated model geometry, the wind tunnel required substantial modification, both in the test section and the diffuser/fan portions of the facility. For the present study, the contraction inlet described above required no modifications and remained immediately upstream of the test section. Shown in Fig. 2.1b is a model of the modified facility as compared to the original wind tunnel components.

2.1.2.1 Blower and Ducting

Due to the large pressure losses in the test section and the low flow speeds available from the axial fan design, a complete fan replacement was needed to allow for the required increase in mass flow through the test section. After some analysis of the original system, and after comparing several options, a centrifugal blower design was selected as a suitable replacement for the existing fan. For this experiment, a Cincinnati Fan, model HP-12G30 blower was selected, accompanied by a 125-hp Baldor, model M4412T-4 electric AC motor. Additional details of the blower sizing and selection process can be found in Appendix A. Due to the flexibility of the Eaton VFD control, the original drive was connected to the new motor, allowing the RS-232 interface to be used for remote control of the new blower, with some modification to the VFD input commands.

In order to integrate the new blower with the original, 11.1-inch diameter test section, ducting was required upstream of the blower in order to both diffuse the flow and to isolate vibrations from the blower to the rest of the test section. While the original axial fan had a 48-inch diameter inlet, the new blower inlet diameter was much smaller, at 14 inches. Therefore, again using diffuser performance specifications from Barlow, Rae, and Pope, a diffusing half-angle of approximately 3.5 degrees was used to minimize losses

downstream of the test section, which resulted in a diffuser length of approximately 24 inches.[25]

With the necessary diameter achieved by this diffuser segment, an additional section of constant-area ducting was required to ensure the test section was sufficiently isolated from any flow disturbances created by the blower. Because the upstream effects of the centrifugal blower design were unknown, a 36-inch section of ducting was connected downstream of the diffuser and upstream of the blower to minimize any rotational flow features induced by the blower on the upstream flowfield. Following the design of the original tunnel, vibration transmission was also minimized in the current design using the same Ventglas® fabric, which was clamped to the downstream end of the constant-area ducting section and also to a special flanged section attached to the inlet of the blower.

Downstream of the blower, an additional diffusing duct was designed and fabricated with the aim of reducing losses as the high-speed flow exited the blower. This not only reduced the speed of the exhaust flow, but also improved the overall performance of the blower. This ducting segment was also designed with a 3.5-degree half-angle, diffusing the flow from a 12-inch diameter cross-section to an 18-inch diameter exit plane, making this exhaust diffuser approximately 50 inches in length.

2.1.2.2 Test Section

Along with the increase in tunnel speed, the aluminum test section segments required modification in order to allow for more measurement capability during data acquisition. The test section modification was performed to support additional measurement locations along the length of the model. Previously, the rotating segment of the test section was 42.5 inches in length, with a shorter, 24-inch, section upstream and another 42.5-inch section downstream. With a new model geometry and configuration, the test section was adjusted so that the 24-inch segment would rotate, with the 42.5-inch sections being fixed upstream and downstream of the primary test region. This required rearrangement of the nylon bushings, ring gear, stepper motor, and support frames, but could be implemented relatively efficiently.

In addition to repositioning the test section, the new arrangement also provided for additional measurement locations within the primary test region. In previous tests, only

upstream and downstream total pressure data could be collected, with the 35 wall static pressures being acquired along the length of the rotating test section. With the new configuration, the shorter rotating section was given nine, 1-inch diameter access ports at various axial locations to allow for a higher density of measurement planes within the region of interest. Along with the nine rotating measurement locations, an upstream measurement plane was also selected in order to provide a clear, upstream representation of the incoming flow. This plane, however, was located within the fixed upstream tunnel segment. Therefore, several slots were installed into the tunnel wall to allow for multiple azimuthal measurement points within this plane. As in the previous setup, each of the access ports allowed for pressure probes or other measurement devices to be inserted into the flow during tunnel operation. They were also designed to be larger than the previous measurement ports to allow for improved optical access. (See Section 2.3.1.3 for a more detailed description of the measurement locations.) Shown in Fig. 2.3 is the new test section configuration, indicating the placement of the new measurement ports.

In order to ensure no leakage during tunnel operation, each probe access port in the test section wall required an individual, fitted plug. These plugs were fabricated in a stereolithography apparatus (SLA) from a black plastic material, which allow them to be easily shaped and made flush against the inner surface of the tunnel wall. Additionally, a separate plug was required that granted the pressure probes access to the flow. Therefore, a plug was designed for the 1-inch diameter access ports, as well as the upstream measurement slots, that incorporated a 1/8-inch through-hole for use with a pressure probe. The plugs also incorporated a tapped counterbore for a 1/8-inch NPT mounting chuck, used to prevent leaks around the probe. Fig. 2.4 shows a plug/probe assembly for one of the rotating measurement ports.

2.1.2.3 Structural Supports

In the original design of the wind tunnel, the fixed segments of the test section simply rested on aluminum A-frames, which were bolted to welded steel support frames. These frames provided the test section with the required height to match the centerline axis of the inlet and fan. However, because the A-frames were attached with a single bolt at each joint, they were relatively unstable during operation of the tunnel and were susceptible

to a substantial amount of vibration. Therefore, during the process of redesigning the test section, the support frames were reinforced with additional bolt locations at the joints and stronger cross beams. Also, rather than resting on small sections of aluminum angle, the fixed test section segments were designed to rest on leveling mounts with nitrile pads. This allowed the test section to be easily aligned and provided a vibration-resistant interface between the supports and the test section. For the rotating segment support frame, the cross beams were replaced with stronger beams while the roller assemblies remained in place to facilitate rotation of the test section.

In addition to these modifications of the original supports, two new frames were designed and fabricated to support the blower and the constant-area ducting immediately upstream of the blower. For the blower support, a frame was designed to be 16.25 inches tall in order to raise the centerline of the blower inlet to 54.5 inches and to match the axis of the test section and tunnel inlet. This frame was fabricated primarily from 3/8-inch thick steel members to withstand several times the weight of the blower and was anchored to the floor of the lab. For the ducting section support, the overall design mimicked that of the three original test section support frames. However, this frame was fabricated completely from steel and welded at all joints to reduce the instability associated with bolted connections. The entire assembly of the blower, ducting, and structural supports is shown in Fig. 2.5.

With each of these new components and modifications to the original components, the experimental model could be incorporated into the test section, allowing for data acquisition and a full study of the flow in the test region.

2.2 Experimental Bypass Model

The intent of the current study was to examine the aerodynamic characteristics of the internal flow of GAC's high-flow bypass nacelle concept. This project provides a full experimental study of the bypass flow to confirm computational models of the same flow region. In the full-scale, the bypass flow occupies an annular region with an inner diameter of 50 inches and an outer diameter of 68.5 inches. The following section details the models used in the present experimental study to replicate the full-scale annular bypass flow.

2.2.1 Original Model

In the previous, off-design experiments, a bypass model was fabricated by GAC, via SLA, to simulate an azimuthal blockage spanning 110 degrees of the test annulus. The gearbox blockage section incorporated a flow diverter segment that parted the upstream flow around the gearbox as well as an aft fairing component to diffuse the flow both azimuthally and radially. Also included in the test region were crane beam supports, which were designed to provide structural support to the core engine components within the nacelle. In the previous study, the inner wall of the flow annulus had a diameter of 8.42 inches, with the outer wall being the 11.1-inch diameter test section. Because the test section was designed to rotate around the model for data acquisition purposes, the model could not be supported within the rotating tunnel segment. Therefore, the model was required to be supported forward and aft of the primary test region. Also, due to the large cross-sectional blockage created by the model itself, a forward contraction cone and an aft diffusive cone were designed to accelerate and decelerate the flow around the model with minimal losses. The fully-assembled model can be seen in Fig. 2.6.

The contraction cone was designed via the method of matching cubic arcs to ensure uniform velocity and total pressure profiles at the start of the full annular flow. This model segment also incorporated four streamlined struts, which acted to center the model within the test section. The aft diffusive cone was designed via Barlow, Rae, and Pope diffuser specifications with a 3.5-degree half angle, resulting in a 3.5-foot long conical section.[25] Along the diffusive cone, eight struts were located a sufficient distance downstream of the test region in order to support the rest of the model on a 3-inch square aluminum tube in a cantilever-style support system. The forward contraction cone was fabricated in a rapid prototyping machine on the Illinois campus, while the aft diffusive cone was fabricated in the Aerospace Department machine shop, primarily from a solid section of polyvinyl chloride (PVC). For more details on the design of the contraction cone, the aft diffusive cone, and the cantilever model design, see Yeong.[18]

2.2.2 Modified Model

For the current study, some significant modifications were made by GAC to the overall bypass design. These changes included (1) increasing the extent of the gearbox

blockage from 110 degrees to 160 degrees, (2) decreasing the centerbody diameter to allow more flow through the bypass region, and (3) incorporating guide vanes forward and aft of the gearbox blockage section. These design modifications required slight alterations in the original model support structure (namely, the aft diffusive cone), and a total replacement of the remaining model sections, which were supplied by GAC.

Additionally, due to the presence of aft guide vanes in the modified design, the portion of the flow around the rear of the gearbox was designed to reach supersonic speeds. With the wind tunnel used in this study, supersonic speeds were not achievable due to limitations of the centrifugal blower. Therefore, an aft vaned model has been analyzed in a separate and parallel experimental study (see Hortensius).[22] With separate forward and aft models, close collaboration was required between the forward, subsonic and aft, supersonic portions of the experiment in order to compare flow conditions and flow behavior in corresponding measurement locations.

In order to provide a full description of the flow features within the forward, subsonic test region, two models were to be thoroughly tested: one which utilized no vanes upstream of the maximum gearbox blockage (the "baseline" model) and one which incorporated nine guide vanes to assist in uniform acceleration of the flow around the gearbox component (the "vaned" model).

2.2.2.1 Contraction Cone & Centerbody

With the modified model design, the overall diameter of the model centerbody required a slight decrease from 8.42 inches to 8.102 inches. This resulted in an overall model scaling factor of 16.2 percent of full-scale. Due to this small decrease in model diameter, a new contraction cone was designed by scaling the previous design in order to correspond to the correct model diameter. A simple geometric scaling was used in the interest of time and since the change in diameter was considered minor. As is common in wind tunnel testing, a 1/2-inch strip of surface roughness was affixed to the aft portion of the contraction cone in order to trip the boundary layer for consistent results throughout the tests. Using preliminary boundary-layer profile measurements and recommendations from von Doenhoff and Horton, which specify a critical Reynolds number based on roughness height and core flow velocity, a mixture of 40, 45, and 50-grit Cataphote microbeads was

appropriate for this application.[26] Fig. 2.7 depicts the new contraction cone section with the attached boundary layer trip strip.

In addition to the new contraction cone, two new centerbody segments were fabricated to simulate the outer surface of the Tay-series engine. These two model segments incorporated mounting holes for the gearbox blockage components on the underside of the model and also featured nine, axially-aligned, 2-inch slots in the downstream segment, which were intended to accommodate short aft guide vanes. While these aft vanes were not representative of the true design of the bypass flow, they were intended to isolate any downstream flow features from the primary test region as well as to indicate the plane at which the true aft vanes would begin. Therefore, nine 1/8-inch thick aluminum plates were inserted and epoxied into the slots in the centerbody surface. The front and rear surfaces of these vanes were rounded to streamline the plates as much as possible with minimal complexity and time investment.

Due to the complex geometry of the model segments, the three sections were fabricated via SLA, from a blue, semi-transparent plastic. The contraction cone segment was approximately 13 inches in length and the remaining model centerbody was composed of a forward and aft section, which were 22.7 and 17.3 inches in length, respectively. Each of the SLA components received for the new model was delivered with a relatively rough surface finish. Therefore, a small amount of sanding and polishing was required to ensure a smooth surface for the tests. After using 180-grit sandpaper to remove the larger roughness elements, a 1500-grit polishing sheet was used to provide a smooth finished surface. This combination of high-grit sanding was found to remove negligible amounts of material and the model diameter remained as needed for proper integration into the test section.

In order to properly fix the centerbody and contraction cone onto the internal support beam, an offset, 3.03-inch square cavity was designed through each of the three model segments. The offset was designed such that the model would rest on the upper corner of the support beam and allow for set screws to be used on the bottom of the beam to hold the model in place. The rounded upper corner can be seen in Fig. 2.8, which illustrates the orientation of the square center cavity within each of the centerbody segments. This design allowed for the contraction cone and two centerbody sections to be

aligned properly and to be essentially fixed within the test section. At each of the set screw locations, as well as the mounting holes for the blockage components, helicoil inserts were used to provide a threaded tap to fasten the parts in place.

2.2.2.2 Baseline Flow

While a full annular flow could have been used to provide an experimental baseline for the vaned model tests, this would not have effectively demonstrated the influence of the guide vanes directing flow around the gearbox blockage. Therefore, in the baseline test, gearbox blockage components were attached to the model centerbody via the mounting holes described above. These two SLA components, which also required sanding and polishing, were designed to represent the flow diverter section and the 160 degrees of blocked annulus, which will now be referred to as the "gearbox blockage" section. For this model, the flow diverter section was approximately 9.75 inches in length and the gearbox blockage section extended for nearly 9 inches downstream of the flow diverter before reaching the front plane of the aft guide vanes. The open, 200-degree portion of the test region will be referred to as the "constant-area blocked section." The primary region of interest ended downstream of the constant-area blocked section, at the plane where the aft guide vanes began. Fig. 2.9 depicts the baseline flow model as it is supported by the downstream struts in a cantilever configuration.

In this experimental setup, the aft portion of the model required additional consideration, since the true bypass design is not accurately represented in this study. While the true aft guide vanes would continue downstream in the full scale, the model in this study included a 5.25-inch extension to the 160-degree gearbox blockage. Then, a short boat-tail fairing was added to the rear of the gearbox in order to reduce the size of the base flow created by the blockage. Additional details of the boat-tail fairing design can be found in Appendix A.

This overall geometry, with the gearbox fairing and boat-tail fairing attached to the centerbody, was examined thoroughly to identify potential positive and negative effects of incorporating the forward guide vanes.

2.2.2.3 Guide Vanes

For the current study of the overall bypass design, GAC was interested in the effects of the forward guide vanes on the flow around the gearbox blockage. Therefore, in addition to the gearbox fairing attachments present on the baseline case, nine guide vanes were incorporated onto the model along the length of the flow diverter section. Each of the ten channels created by the guide vanes was designed with an equivalent contraction ratio, beginning with a 36-degree annular arc and contracting to a 20-degree annular arc. This design was intended to provide a uniform flow profile into the constant-area blocked section and, therefore, provide uniform flow into the aft set of guide vanes.

In the initial design stages for the vaned model segment, several designs were evaluated to determine the most effective way of incorporating the guide vanes onto the existing model. The two primary options for consideration included building a vane structure that could attach to the original centerbody segment or building a new model segment with the vanes integrated into the part. Because one of the main concerns with the vaned design was the potential for flow leakage between channels, several options were considered to address this, including those with an external shroud around the vanes. Ultimately, a design was chosen that provided an integrated centerbody/vane structure without an external shroud.

Because fabrication of the part was also a critical issue due to the tolerances required for the inner wall of the test section as well as the thin vane structures, the final design was to be manufactured with a selective laser sintering (SLS) device. Similar to stereolithography, which typically fabricates plastic parts, laser sintering also allows for metallic structures to be built in a layered manner from a powder substance, with comparable material properties as the intended base metal. The SLS model for this study was fabricated from a stainless steel powder, which provided sufficient strength along the thin vane members. Shown in Fig. 2.10 is the vaned segment of the model integrated with the centerbody and gearbox components.

When incorporated with the baseline model, each of the nine vanes were located along the length of the flow diverter section and extended less than 0.2 inches into the constant-area blocked section. The axial extent of the vanes alternated between 10.3 and 12.1 inches, with the top center vane being shorter in length. This configuration also

required a 2-inch, upstream extension of the flow diverter section. In order to maintain the 16.2-percent model scale, the vanes were designed to be only 0.042 inches thick. Fig. 2.10 depicts the channel numbering scheme, with Channel 1 being the topmost channel and Channel 5 being the channel adjacent to the gearbox fairing. Due to model symmetry, the mirrored channels will be referred to as Channels 1' through 5'.

Since this model design incorporated a new centerbody segment with the vanes already attached, the original forward centerbody section could not be used for the vaned model tests. Also, because the metal SLS component included only the vaned section of the model, two additional plastic spacer segments were fabricated to compensate for the 22.7-inch length of the original forward centerbody section. Overall, the vaned SLS section was 12.2 inches in length, which required forward and aft spacers of 3.0 and 7.5 inches in length, respectively. Each of these three segments featured the offset center cavity, support beam set screws, and gearbox fairing mounting holes, similar to the previous centerbody segments. Again, the plastic sections required sanding and polishing to ensure a smooth test surface and all of the mounting and set screw holes required tapping and/or helicoil inserts. Because the vaned portion of the model was fabricated from stainless steel, GAC provided a smooth, painted surface prior to shipment, requiring no surface finish modifications after delivery.

In order to minimize leakage between the flow channels in the guide vane section, the vane tips required sealing against the test section wall. Several sealing methods were considered, including a permanent seal using silicone or epoxy along the vane tips as well as a temporary seal that would allow for the model to be disassembled at the conclusion of the tests. Because it would be necessary to disassemble the tunnel between certain tests, the decision was made to attach a flexible material to the vane tips such that the model could slide in and out of the test section, but also provide enough elasticity to seal any gaps between the vanes and the tunnel wall. Due to the small thickness of the vanes, a method was chosen that utilized small-diameter silicone tubing attached to the vane tips. This method required the tubing to be slit along its length in order to be attached along the vanes.

Tubing with an outer diameter of 0.085 inches was chosen to seal the vanes. Having a wall thickness of 0.025 inches, the silicone material allowed for compression to

approximately 0.006 inches, allowing for some variation in gap size between the vanes and the tunnel wall. In cases where the gap was larger than 0.025 inches, larger tubing, with a wall thickness of 0.031 inches was substituted for the smaller-diameter tubing; however, use of the larger tubing was avoided as much as possible due to its greater effect on the flowfield. Fig. 2.11 shows the vaned section of the model with the silicone tubing affixed to the vane tips.

2.3 Data Acquisition

Once each of the models was installed in the wind tunnel, several measurements were made to characterize the flow within the bypass region. With the access ports located in the rotating and stationary segments of the test section, pressure profiles could be collected using a pitot-static probe, a total pressure probe, and a five-hole pressure probe. In addition to pressure measurements, flow direction on the model surface could be characterized using surface oil flow visualization. The following section details the method and apparatus used to acquire each type of experimental data.

2.3.1 Pressure Measurements

In many wind tunnels, pressure probes are used to determine freestream and local flow properties through the combination of total and static pressure readings. For the present experimental setup, the bypass geometry was expected to generate highly three-dimensional flow characteristics. Therefore, a combination of probe types, in conjunction with numerous static pressure measurements, was used to fully describe the flow within the bypass region.

2.3.1.1 PSI System 8400

All pressure data in this experiment were collected and processed by a Pressure Systems, Inc., System 8400. This system was composed of a main processor, a pressure calibration unit (PCU), a scanner digitizer unit (SDU), a scanner interface, and a variety of miniature electronically-scanned pressure (ESP) modules. Fig. 2.12 shows the main processor, PCU, and SDU located in the ARL control room. This device was controlled

remotely from the main data acquisition computer through an IEEE-488, general purpose interface bus (GPIB), connection and through the main LabVIEW code.

Each available ESP module was capable of measuring 32 differential pressures. Due to the number of pressure readings required for the current study, only one ±5-psid scanner was needed for data acquisition. In addition to the 32 primary pressure ports on the ESP module, it also included a reference pressure port and three calibration ports (C1, C2, and Cal). Shown in Fig. 2.13 is the ESP module used for this experiment as well as details of the pressure port configuration.

Due to ambient temperature and pressure fluctuations in the lab, the ESP module required calibration before each test run. During a calibration cycle, a nitrogen tank supplied a 100-psi burst to the C1 port in order to switch the operation mode from RUN to CALIBRATE. In this mode, a vacuum pump applied negative pressure through the Cal port to produce a five-point calibration for each of the 32 pressure ports. The 100-psi nitrogen supply was then applied to the C2 port in order to switch the module back to RUN mode.

Once in RUN mode, and throughout pressure data acquisition, the System 8400 was designed to collect data in sets and output them immediately to the LabVIEW program. In the current study, the processor averaged 127 measurements for each set, which was the maximum allowable by the system. Between measurements, the system was also configured for a 0.01-second delay, allowing measurement sets to be collected nearly every second. When relayed to the LabVIEW code, the pressure values were output from the System 8400 in engineering unit format rather than raw data format. Although this increased internal processing time, the output frequency was sufficiently high for the required experiments. In the case that a higher sampling frequency was required for more detailed analysis, the System 8400 could be easily reconfigured before a data acquisition run.

2.3.1.2 Pressure Probes

To fully characterize the flow behavior in all sections of the wind tunnel, three separate pressure probes collected data at various points within the flowfield. The three probes described below can be seen in Fig. 2.14. A United Sensor Corporation, model

PCC-12-KL pitot-static probe was used throughout various tests in this study. This probe utilized a 12-inch stem and a 1/8-inch tip diameter and included a total pressure port on a rounded tip and an average of four static pressure ports slightly downstream of the probe tip. This design was intended to provide an accurate representation of flow speed in freestream flow conditions with minimal directionality.

Because the flow in the main bypass region was expected to be highly three-dimensional, the rounded pitot-static probes would not provide accurate readings of total or static pressure in areas of high flow angularity. In cases such as these, a United Sensor Corp., model USNH-A-469 total pressure probe was used, which incorporated a 30-degree chamfered tip. The chamfered design was intended to capture an accurate total pressure reading at relatively high flow angles, when compared to the other probes with rounded tips. This total pressure probe was specifically designed with a 90-degree miter joint at the stem/tip junction, a reinforced stem, and a 1/16-inch tip diameter. The small probe diameter was chosen in order to minimize any flowfield interference and to allow for higher measurement resolution within the boundary-layer profiles.

The final type of pressure probe used in the current study was a United Sensor Corp., model USNH-F-207 five-hole three-dimensional probe. The five-hole probe utilized a conical tip, which included a total of five pressure ports: one was centrally located, two were above and below the central port, and two were to the left and right of the central port. The five-hole probe maintained a separate reading for each of the four downstream ports; this configuration allowed for measurement of a representative total pressure as well as four additional and distinct pressure readings, which could then be used to describe the horizontal and vertical orientation of the probe. Because of the compact internal configuration, a manifold was located at the end of the probe, which granted access to each of the five pressure readings. Also, due to space limitations, the five-hole probe had a diameter of 3/32 inches, which was slightly larger than that of the total pressure probe.

While the pitot-static and total pressure probes provided accurate results at a wide range of speeds, the accuracy of the five-hole probe was dependent on both the flow speed and the degree of the flow directionality. Because of this strong interdependence, the five-

hole probe required a detailed calibration for use in the bypass flow region. Additional details of the five-hole probe and the associated calibration can be found in Appendix B.

During a given test, each of the pressure probes was connected to the ESP module via 0.063-inch diameter polyurethane tubing. The tubing was given ample length to allow for a full rotation of the test section, but was kept as short as possible in order to minimize losses and measurement lag.

2.3.1.3 Measurement Locations

The overall aim of the current experiment was to fully characterize the flowfield upstream and downstream of the forward guide vanes and to determine the inlet conditions for the aft guide vanes. High-resolution measurements were acquired to fully describe all flow features in this region. With the rotating design of the test section, coupled with a radial traversing system, a full radial and azimuthal set of data points could be gathered during a given test. Therefore, in order to fully describe the flow behavior along the axial direction, multiple measurement planes were required throughout the test region. As briefly described in Section 2.1.2.2, one upstream measurement plane was located in the fixed upstream tunnel section and nine measurement planes were positioned within the rotating portion of the test section. Of the nine rotating measurement planes, six were located within the constant-area blocked section of the bypass flow, and three were located downstream of the aft guide vanes. Fig. 2.15 depicts the location of the measurement planes with respect to the vaned model.

Along the rotating test section, where full radial and azimuthal pressure profiles could be easily collected, the nine access ports were arranged in such a way as to allow sufficient axial resolution of flow features. Because the flow within the constant-area blocked section was identified as the most critical to this study, six of the 1-inch diameter access ports were located along this region, spaced in 1.5-inch axial increments. These ports were positioned such that the tip of the probe in the first plane was located only 0.125 inches downstream of the forward guide vanes. This allowed for a full characterization of the shear layers and boundary layers at the exit of the vane channels and throughout the constant-area blocked section. For future reference, each of the downstream rotating

measurement planes will be referred to as MP1, MP2, MP3,…, MP9 and the upstream measurement plane will be annotated MP0.

Downstream of the sixth measurement plane (MP6), and still within the rotating test section, the three remaining measurement planes were located 0.25, 5.5, and 10 inches downstream of the aft guide vanes. This allowed for a detailed analysis of the flow as it exited the primary region of interest. Because these ports were located downstream of the aft guide vanes, they were intended to characterize the flow exiting the constant-area blocked section and, more specifically, the performance of the boat-tail fairing and the corresponding base flow.

To supplement the nine rotating measurement locations, the forward measurement plane was located approximately 13.5 inches upstream of MP1, within the fixed upstream portion of the test section. The axial location of this plane was only 1.5 inches upstream of the guide vanes and was positioned to provide adequate clearance for the pressure probes. Although the upstream segment of the test section was unable to rotate, sufficient data were required at this plane in order to fully characterize the flow as it entered the guide vane channels. Therefore, fifteen separate azimuthal measurement stations were located along the circumference of the tunnel wall. Rather than using a separate access port at each azimuthal location, five slots, which could each accommodate three measurement locations, were positioned such that every other flow channel would be accounted for in a single tunnel configuration. Then, by rotating the upstream tunnel section 180 degrees about its axis, these measurement stations would allow for a detailed characterization of the flowfield at a total of 30 azimuthal locations, equally spaced in 12-degree increments. Fig. 2.16 provides a schematic of the azimuthal orientation of the measurement points with respect to the location of the guide vanes.

While each of the access ports accommodated a pressure probe during a given test, the static pressure was also needed at each axial and azimuthal location to determine airspeed and other flow characteristics. To measure the static pressure at each probe location, a small, 0.042-inch diameter hole was located upstream of each access port such that the static pressure could be measured within the same plane as the tip of the pressure probe. (An exception to this was at MP1, where, due to the measurement plane being near the forward end of the rotating test section, the static pressure was measured approximately

0.25 inches downstream of the probe tip.) At each of the static pressure measurement locations, 0.040-inch diameter stainless steel tubing was held with epoxy in the static pressure port on the tunnel wall and connected to 0.040-inch diameter urethane tubing. This was then connected to 0.063-inch tubing, which interfaced with the ESP module.

In addition to the static pressures measured near the probe locations, there were also 35 static pressure ports along the length of the fixed upstream portion of the test section (See Section 2.1.1.1). Although the measurement ports were located along the bottom of the tunnel wall in one configuration, they could also measure the static pressures along the top of the test section when this tunnel segment was rotated 180 degrees about its axis. While these measurements were no longer a critical part of the test section measurements, they were utilized to depict the behavior of the upstream flow as it approached the contraction cone, guide vanes, and the flow diverter. In fact, the axial static pressure variation could be related to the axial variation in cross-sectional area in order to compare the actual pressure change with the isentropic behavior of the flow as it traveled along the length of the model. In general, these measurements were intended to provide a better understanding of the incoming flow and to validate the assumption of isentropic compression through the test section.

2.3.2 Wind Tunnel Automation

Due to the high-resolution spacing of radial and azimuthal measurement points required for a full pressure profile in the bypass region, the data acquisition procedure was fully automated to reduce the time required to collect a complete data set. Using a program written in LabVIEW, angular rotation of the test section, radial displacement of the pressure probe, and the collection of pressure data were synchronized to fully characterize the flow features within the test section. Due to the complexity of the LabVIEW program, a separate code was written exclusively to control the blower through the variable frequency drive. This precaution was taken for safety purposes, in case the blower motor required an immediate shutdown during a test. This decoupling of the two systems would also allow for the motor to be run without the need to operate the full data acquisition code.

2.3.2.1 Controlled Devices

The test section rotation was the most critical and novel feature of the axisymmetric wind tunnel. Without this capability, a full azimuthal characterization of the flow would not be possible. Therefore, as briefly mentioned in Section 2.1.1.1, a 400-mm diameter ring gear (Quality Transmission Components, model KSSR2-200) was attached to the downstream bushing on the rotating test section and was driven by a 70-mm diameter spur gear (Quality Transmission Components, model MSGB2-35) attached to a high-torque stepper motor. The stepper motor, an Anaheim Automation, model 34YSG207S, had an internal gear ratio of 4.985:1, with a standard step size of 1.8 degrees and a maximum torque of 3500 oz-in. Accompanied by an Anaheim Automation, model DPY50601 programmable controller, the step size of the motor could be further reduced to microsteps, with a resolution of 0.028 degrees per step, if required. With the assistance of the controller, the stepper motor was operated via an RS-232 connection with the main data acquisition computer and through the LabVIEW code. The motor, spur gear, and controller are shown in Fig. 2.17.

With an internal gear ratio of 4.985:1 and a ring/spur gear ratio of approximately 5.7:1, the test section was rotated with a resolution of 0.0079 degrees per microstep. Then, through the controller, the motor speed was set to 200 microsteps per second (1.6 degrees per second), which enabled smooth rotation of the test section. Because the motor/controller device did not allow for feedback control, a US Digital, model A2T absolute optical inclinometer was attached to the upstream bushing on the rotating test section. This allowed the orientation of the test section to be known at any given time during a test. The inclinometer, shown in Fig. 2.18a, had an accuracy of 0.1 degrees, which allowed for highly-resolved azimuthal spacing of the measurement points within each plane. Using a serial encoder interface (SEI) to RS-232 connection, the inclinometer readings could be monitored via the LabVIEW program and coupled with the stepper motor controls to achieve a precise azimuthal position.

To capture flow characteristics in the radial direction, a Zaber, model KT-LSR150B linear traverse was mounted on the outer surface of the tunnel wall at each of the probe access ports. Again, using an RS-232 connection, the traverse could be controlled via LabVIEW and coupled with the stepper motor and inclinometer devices. Unlike the motor,

the traverse allowed for feedback control; therefore, the radial position was always known. Connected to the traverse was a nylon probe attachment device, which held the pressure probes during a given test. Using this setup enabled each of the pressure probes to be displaced along the radial extent of the annular channel, allowing for a full characterization of both the inner and outer boundary-layer profiles as well as the core flow. The traverse is shown in Fig. 2.18b, with the attached nylon probe mount.

In addition to collecting differential pressure data within the test section, ambient temperature and pressure are also measured and added to the data set for each measurement point. The ambient temperature of the laboratory high-bay area was collected through an Omega, T-type thermocouple and the absolute ambient pressure was collected with a Setra 270 pressure transducer in the ARL control room. The temperature reading was taken in the high-bay area and sent to a signal conditioner in the control room. The pressure reading was measured in the control room in order to reduce the impact of any ambient pressure fluctuations caused by the tunnel exhaust flow in the high-bay area. In order to interface these ambient condition readings with the test section pressure data, they were processed through an analog-to-digital (A/D) converter and input into the data acquisition computer and the main LabVIEW code. A schematic detailing the device connections is shown in Fig. 2.19.

2.3.2.2 Test Procedure

The test section rotation and data acquisition process was completely automated through the LabVIEW code. Before an automated test could begin, however, the tunnel operator was required to prepare for the test run and provide several inputs to the LabVIEW program. The following required completion before a test could commence:

a. Determine the azimuthal and radial extent required for the test.
b. Input the maximum and minimum azimuthal and radial positions and the spacing desired for each. (This could either be equal spacing or a pre-defined, variable spacing.)
c. Rotate the tunnel to the appropriate starting angle and mount the desired probe onto the traverse.

d. Fasten the probe plug into the probe access port and tighten the mounting chuck around the probe to prevent unwanted leakage.
e. Complete the System 8400 calibration procedure to calibrate and zero the ESP modules.
f. Start the blower via the separate LabVIEW code and gradually increase the tunnel flow speed to that required for the test.

Once the tunnel and probe were prepared for a test, the following steps outline the basic commands that allowed the separate devices to function throughout a high-resolution test. These LabVIEW procedures began once the test operator initiated the automation program and continued until the end of a given test.

1. Traverse the probe to the maximum radial position (nearest the outer tunnel wall).
2. Check to ensure the test section is oriented at the correct azimuthal position (within 0.1 degrees). If not, rotate test section to the desired azimuthal position.
3. Collect pressure data and traverse the probe to the next radial position.
4. Repeat Step 3 until the probe reaches the minimum radial position (nearest the model).
5. Traverse the probe to the maximum radial position and rotate the test section to the next azimuthal position.
6. Repeat Steps 2-5 until the probe fully traverses the channel at the desired ending azimuthal position.

At the conclusion of each test, the operator could save the raw pressure data, with reference to the local azimuthal and radial position for each data point, to a text file for further analysis. Using the above procedure ensured that each test was run in a consistent manner and minimized the time required to administer a given test. Also, as mentioned previously, this procedure could be used with any of the pressure probes and was flexible with regard to the resolution of a particular measurement. For instance, the vaned model was expected to require a higher azimuthal resolution than the baseline model due to the presence of shear layers and boundary layers aft of the guide vanes. In this case, smaller azimuthal spacing could be specified in certain areas of high interest near the vanes.

For the data sets collected at the upstream measurement plane, this same procedure could be run without control of the test section rotation angle. At these probe access ports, only the radial pressure variation could be measured, so the stepper motor and inclinometer commands were bypassed, with the LabVIEW program only sending commands to the linear traverse and the System 8400.

2.3.3 Surface Oil Flow Visualization

In addition to collecting pressure measurements throughout the flow region, supplementary methods of flow characterization are available using various flow visualization techniques. These methods include, but are not limited to, surface oil flow, surface tufts, and smoke visualization techniques. Although smoke visualization and surface tufts could provide a real-time portrayal of the three-dimensional flow features in the bypass region, these methods were unfeasible due to the limited optical access within the test section. On the other hand, however, surface oil flow visualization effectively takes a time-averaged snapshot of the flow features on a given surface. Therefore, this method would allow time for the test section to be disassembled in order to observe the oil flow patterns formed on the model while the tunnel was running at the designed speed.

When using oil flow visualization, the goal is to seed the oil with a visible indicator so that the flow behavior can be easily observed in the resultant oil patterns. For the current study, Interdynamics Fluorescent Leak Detector Dye was chosen as the indicator, which required an ultraviolet/black light for visualization. In many oil flow visualization experiments, common motor oil or mineral oil is used as the base oil in the mixture. However, due to the high flow speeds in the constant-area blocked section, the large surface shear stresses were shown to remove the oil from the model surface before any patterns could be established. Therefore, STP® Oil Treatment, an oil additive, was used as the base of the mixture and provided a significantly higher viscosity than other common oils. Mixing a large drop of the fluorescent dye in every milliliter of oil provided a sufficient mixture ratio for the high-speed flow regions encountered within the bypass region.

To prepare the bypass model for a test, thin sheets of black contact paper were applied to the model surface. Because the SLA model was fabricated from a blue, semi-

transparent plastic material, the black contact paper provided contrast between the oil/dye mixture and the model to improve visualization of the oil patterns. Using a grid pattern with pre-determined spacing, small dots of the oil/dye mixture were applied to the grid using a 26-gauge hypodermic needle. While a highly-resolved spacing would seem to provide a high-resolution depiction of the flow behavior, dots placed too close together resulted in streaks interacting with each other and distorting the true flow behavior. Therefore, several iterations were required to determine an advantageous combination of dot size and grid spacing. Fig. 2.20 provides an example of the dot spacing applied to black contact paper on the baseline model. If more detail was required in a certain region of the flow, the grid spacing could be decreased for subsequent tests, while also decreasing the dot size accordingly.

With the oil mixture applied to the model surface, the tunnel was assembled and the blower speed was increased as quickly as possible. The rapid flow acceleration was needed to ensure the oil patterns were created by the air flow at the desired higher speed rather than a slower, off-design speed. The tunnel speed was then maintained for several minutes in order to fully establish the oil patterns along the model surface. After a completed test, the blower motor was shut down and the tunnel was quickly disassembled. In order to expose the fluorescent oil patterns, the main lighting in the high-bay area was turned off and several black lights were positioned approximately six to eight feet away from the model. Then, using a Nikon, model D3100 digital SLR camera, images of the oil patterns were recorded using exposure times of up to five seconds. Exposure lengths were determined based upon the intensity of the fluorescent oil patterns; in this case, several seconds were required due to the distance of the black lights from the model surface. This method required no post-processing of the images; however, the oil patterns could be enhanced, if necessary, by altering brightness, contrast, and/or color levels.

2.4 Test Plan

In order to fully characterize the flow within the bypass region, several test configurations were required. As mentioned previously, the two cases being tested in the

current study include the baseline model and the vaned model. Table 2.1 below is a summary of the test matrix used to collect the pressure profile data.

Table 2.1 Test Matrix.

Model Configuration	Measurement Location	Total Probe	5-Hole Probe	Wall Static Ports	Number of Radial Pts.	Number of Azimuthal Pts.
Baseline	MP1 – MP9			X	—	160
Baseline	Upstream	X			21	30
Baseline	MP1 – MP6	X			19	51
Baseline	MP7 – MP9	X			13	35, 81, 89*
Baseline	MP1 – MP6		X		15	35
Baseline	MP7 – MP9		X		9	53, 53, 61*
Vaned	MP1 – MP9			X	—	200
Vaned	Upstream	X			21	15
Vaned	MP1 – MP6	X			13	198
Vaned	MP7 – MP9	X			9	98, 102, 114*
Vaned	MP1 – MP6		X		11	98
Vaned	MP7 – MP9		X		9	98, 102, 114*

*Due to widening of the flow region, values are listed for MP7, MP8, and MP9, respectively.

A notable feature of the above test matrix is the difference in radial and azimuthal resolution between the various tests. These differences were justified based upon (1) the presence or absence of vanes in the flow, (2) run time required for a given test, and (3) priority of the test data. For example, for the profiles in MP7-MP9, additional azimuthal measurement locations are required to fully capture the flow behavior aft of the guide vanes. Also, for any case where vanes are present, the number of radial points was reduced due to the increase in run time from the addition of azimuthal measurement locations. As an example of profile resolution, Fig. 2.21 provides an illustration of the measurement spacing used for the vaned model within the constant-area blocked section.

As a supplement to the high-resolution pressure profiles, surface oil-flow visualization was also performed on both the baseline and vaned model configurations. For the baseline case, the primary region of interest for surface streamlines was the constant-area blocked section, with some data taken slightly upstream from this region as well. The surfaces studied in this test included the centerbody and the wall of the gearbox fairing. For the vaned case, the constant-area blocked section was again a primary focus; however,

the vaned channels were also expected to contain complex surface flow features. Therefore, in addition to studying the centerbody and the wall of the gearbox fairing, the walls of the vaned channels were also analyzed in this model.

2.5 Flow Variables

Throughout the current test, the primary flow characteristics that could be measured with the available pressure probes included the local total and static pressures as well as the five measurements from the five-hole probe. From these values, and various static pressure measurements, local Mach number and local flow direction could be derived and used for analysis of the overall flowfield. The intent of the following section is to detail the derivation of flow variables calculated from the measured pressure data.

2.5.1 Tunnel Speed

In order to compare flow features between the various measurement planes, each test required similar inlet flow conditions. In many wind tunnel studies, test section speed is determined based upon the difference in static pressures across the highly-convergent tunnel inlet, since the test section typically maintains a constant cross-sectional area downstream of the inlet. The current tunnel inlet possesses the capability to measure tunnel speed in this manner; however, due to the large change in cross-sectional area downstream of the inlet, this type of reference measurement may not have provided the precision required to prepare each test in a similar manner.

For the current study, the constant-area blocked section was expected to be the most critical portion of the flow, due to this location having the smallest cross-sectional area through the entire test section. Therefore, this region could be considered the effective throat of the wind tunnel. In order to set the tunnel speed in a consistent manner, the fifteen static pressure readings used for the upstream measurement plane were selected to provide the speed reference measurements. This location was chosen for the reference conditions since the cross-sectional area of the test section was more comparable to that of the constant-area blocked section, with the model centerbody creating a full, 360-degree annulus.

The aim of the current study was to examine the flow characteristics at a given Mach number. Therefore, in order to maintain a consistent Mach number profile throughout the test section, the upstream Mach number could be held constant between tests. This method neglected changes in Reynolds number due to fluctuations in ambient conditions. Nevertheless, these changes were expected to be minor and have little to no impact on the results of the study. In order to maintain a consistent Mach number profile, a pressure ratio was developed using an average of the 15 upstream static pressure measurements and the total pressure at this measurement plane. Due to the large contraction ratio of the inlet, and based upon total pressure measurements obtained at this plane, losses from ambient conditions were found to be negligible and the upstream total pressure was be assumed to be approximately equivalent to the ambient lab pressure. Using this simplification, the upstream inlet pressure ratio is shown below and was monitored throughout each test in order to provide consistent speed conditions between runs.

$$\left(\frac{P}{P_t}\right)_\infty = \frac{1}{15}\sum_{i=1}^{15}\left(\frac{P_{USi}}{P_{t,\infty}}\right) \cong \frac{1}{15}\sum_{i=1}^{15}\left(\frac{P_{USi}}{P_{amb}}\right) = \frac{P_\infty}{P_{amb}} \tag{2.1}$$

2.5.2 Static Pressure Correction

When performing a preliminary investigation of the pressure probe measurements within the primary test region, a discrepancy was revealed in the static pressure readings measured along the outer wall of the test section. Fig. 2.22 demonstrates this discrepancy, where the static pressures shown were taken from (1) the outer wall tap without a probe in the flow, (2) the outer wall tap during full radial motion of the probe, and (3) the pitot-static probe as it was traversed through the annulus. Note that the static pressure measured without the probe was assumed to be constant across the radius of the annulus. This assumption will be discussed at the end of this section. Also note the values depicting the radial position of the probe; for future reference, the radial position has been nondimensionalized with the procedure in Eq. 2.2, where $R^*=0$ and $R^*=1$ indicate the inner and outer walls of the test annulus, respectively. In addition to the static pressure surveys, the total pressure measured by the pitot-static probe was also given in order to establish the locations of the inner and outer boundary layers.

$$R^* = \frac{R - R_{inner}}{R_{outer} - R_{inner}} \tag{2.2}$$

Due to the small radial extent of the flow annulus, radial variations in the static pressure were presumed to be negligible. Although this assumption ignored the presence of three-dimensional flow features, such as streamline curvature and vorticity, the 1.5-inch annular channel was not expected to contain flow features that would cause the flow to deviate significantly from this assumption. Therefore, with this in mind, the static pressure variations measured in Fig. 2.22 were assumed to be a result of probe interference within the flow annulus. Although the chosen tip and stem diameters of the probes were designed to have minimal effect on the overall flowfield, the small internal dimensions of the flow annulus allowed for significant local blockage within the proximity of an individual measurement point. For instance, when the probe tip was collecting boundary-layer measurements near the model, an entire radial section of the annulus was obstructed by the probe stem.

Several features were observed from the data presented in Fig. 2.22. First, the static pressure reading from the pitot-static probe was relatively constant within the core flow and only exhibited significant deviations within each of the boundary layers. Also, for the wall static pressure readings with the probe in the flow, the values varied throughout the annulus, with high pressure readings when the probe was within both boundary layers. Finally, the constant wall static pressure, measured without a probe in the flow, tended to be, in general, higher than the static pressures recorded in the other two cases.

According to investigations by Chue and Bryer and Pankhurst, each of these features had been previously demonstrated in experimental studies.[27,28] For instance, due to the sharp pressure gradients within boundary-layer flow, the average of four static pressures collected around the diameter of a pitot-static probe could be artificially weighted based upon the strength of the local pressure gradient. Therefore, for the pitot-static probe, valid static pressures may have only been measured within the core flow, where flow properties tend to be more uniform. In order to describe the behavior of the wall static measurement when the probe was traversing through the annulus, two factors were considered, including effects due to the probe tip and effects due to the probe stem. These two factors have varying effects on the measured wall static pressure depending on the

position of the probe tip within the flow region. For example, when the probe was collecting measurements very near to the model surface (Case 1), the probe stem spanned the entire annulus. In this situation, the effect of the probe tip was minimal, since the tip was essentially submerged within the inner wall boundary layer. Conversely, when the probe was collecting measurements near the outer wall of the test section (Case 2), the blockage effect of the probe stem was virtually nonexistent. This also meant that the effect of the probe tip was very significant, since the probe tip was positioned just 0.10 inches downstream of the wall static pressure port.

Studies have shown that, for Case 1, the stem blockage effect acted to increase the measured wall static pressure. Studies have also shown that, for Case 2, a stagnation region could be formed immediately upstream of the probe tip, causing the measured pressure at the wall to be high. Then, as the probe was traversed away from the outer wall, the stagnation-type behavior transitions to venturi-type behavior, where the blockage caused by the probe tip increased the flow speed and decreased the measured static pressure at the wall. Therefore, when the probe was far from both the inner and outer walls, a combination of these effects caused the discrepancies measured within the core flow.

A final justification of the static pressure measurement error lies in the possibility of non-axial flow. Also demonstrated in Chue, a pitot-static probe with a rounded tip records static pressure error if the probe tip is not aligned parallel to the flow.[27] Because the overall bypass flow was expected to contain three-dimensional features, non-axial flow was anticipated, and later measured (see Section 3.2.3), within the constant-area blocked section, within the regions where the static pressure readings were in question.

With the compounding effect of each of these sources of error, the decision was made to use empty tunnel measurements of wall static pressures without a probe inserted in the flowfield. Therefore, one measurement at each azimuthal location was deemed sufficient to describe the static pressure throughout the test section. Then, using static pressure coefficients, corrected static pressures were used in conjunction with the total pressure profiles to develop corresponding Mach number profiles. As stated previously, this method did not account for three-dimensional variations in static pressure and only presented a general depiction of Mach number distribution within the bypass region.

2.5.3 Static and Total Pressure Coefficients

In standard wind tunnel testing, static pressure coefficients are typically used to provide a comparison of bodies in flow at varying speeds and flow conditions. In most situations, the pressure coefficient is defined as follows, which relates a local, measured pressure to the freestream flow conditions.

$$C_p = \frac{P - P_\infty}{q_\infty} \tag{2.3}$$

$$q_\infty = P_{t,\infty} - P_\infty = \frac{1}{2}\rho_\infty {V_\infty}^2 \tag{2.4}$$

In the case of the internal compressible flow examined in this study, however, the standard definition of the freestream condition was not appropriate to compare data sets, due primarily to the high contraction ratio downstream of the forward contraction cone. Therefore, the freestream designation in this study was selected as the condition at the upstream measurement plane (MP0). This was suitable for the current application since 15 static pressures were continuously monitored at this plane around the circumference of the test section. These pressure measurements were used to determine the average upstream static pressure as well as the upstream dynamic pressure, as defined in Eq. 2.5 for compressible flows.

$$q_\infty = \frac{\gamma}{2} P_\infty {M_\infty}^2 \tag{2.5}$$

In order to define the freestream Mach number, the freestream total pressure was taken as the ambient lab pressure, as described in the previous section.

In addition to the static pressure coefficient, total pressures also required direct comparisons between tests. As with the static pressure, the total pressure measurements were nondimensionalized with the same dynamic pressure term, but as a difference from the freestream total pressure rather than the freestream static pressure. Therefore, the nondimensionalized total pressure was defined as shown below.

$$P_{t,non} = \frac{P_t - P_{t,\infty}}{q_\infty} \cong \frac{P_t - P_{amb}}{q_\infty} \tag{2.6}$$

Using the above definitions for the pressure coefficients allowed static and total pressure contours to be compared between tests, regardless of fluctuations in ambient conditions.

2.5.4 Mach Number

In low-subsonic flows, with Mach numbers less than approximately 0.30, air is typically assumed to be incompressible. This assumption neglects small variations in density and is valid given the small static pressure gradients within the relatively slow-moving flow. In these cases, the local flow speed could be derived from the incompressible Bernoulli's equation in Eq. 2.7, which also assumed the flow was inviscid and a streamline was selected with negligible change in elevation (i.e. no hydrostatic effects).

$$P_1 + \frac{1}{2}\rho {V_1}^2 = P_2 + \frac{1}{2}\rho {V_2}^2 \tag{2.7}$$

By setting one of the flow conditions as a stagnation point, with zero velocity, the local velocity can be determined by utilizing the difference between the local total and static pressures, or, in other words, the dynamic pressure. Then, using the relationship between the local velocity and the local speed of sound, the flow Mach number can be obtained as well.

While this procedure is valid for low-speed flows, it can introduce large errors if used with compressible flows having Mach numbers above 0.30. For the current study, the flow within the constant-area blocked section was expected to reach speeds in excess of Mach 0.70; therefore, a compressible alternative to Bernoulli's equation was required to determine accurate formulations of the Mach number within the test region.

In order to characterize the high-speed flows within the bypass region using only static and total pressure measurements, an alternate formulation was chosen that utilized the properties of an isentropic flow. In isentropic flow, all processes are assumed to be reversible and adiabatic; in other words, there is no change in overall entropy of the fluid system. For this type of flow, the pressure, density, and temperature at a given point within the flow were related such that

$$\frac{P_1}{P_2} = \left(\frac{\rho_1}{\rho_2}\right)^{\gamma} = \left(\frac{T_1}{T_2}\right)^{\frac{\gamma}{\gamma-1}} \tag{2.8}$$

where γ=1.4 is the ratio of specific heats for air. As a simplification of the above equation, the flow in the bypass region was assumed to have been accelerated from rest isentropically. Therefore, one state could be considered the stagnation condition, with zero

velocity. Using this simplification, in conjunction with the one-dimensional energy equation, the temperature ratio could be found as a direct function of Mach number.[1]

$$\frac{T_o}{T} = 1 + \frac{\gamma - 1}{2} M^2 \tag{2.9}$$

Then, using the isentropic relationship from Eq. 2.8, the pressure ratio could also be found as a function of Mach number.

$$\frac{P_o}{P} = \left(1 + \frac{\gamma - 1}{2} M^2\right)^{\frac{\gamma}{\gamma - 1}} \tag{2.10}$$

Finally, rearranging this equation then yielded the local Mach number, which required only the ratio of static and total pressures measured at a given point in the flow.

$$M = \left\{ \frac{2}{\gamma - 1} \left[\left(\frac{P_t}{P} \right)^{\frac{\gamma - 1}{\gamma}} - 1 \right] \right\}^{1/2} \tag{2.11}$$

In contrast with the method for determining flow speeds in low-subsonic flows, this method provided a more direct formulation for Mach numbers using the relationship between two measured pressure values.

2.5.5 Mass Flow Rate

By using local flow conditions within the constant-area blocked section, mass flow rate could be determined in order to validate the calculated flow speed measurements. By ensuring the values of mass flow remained constant throughout the test region, the measured and calculated flow characteristics could be confirmed.

In general, the mass flow rate at any measurement plane could be calculated using Eq. 2.12 below. Note that the velocity term must be derived from the Mach number calculated previously.

$$\dot{m} = \rho V A \tag{2.12}$$

In order to obtain a local velocity from the local Mach number, the definition of Mach number was used in conjunction with the definition of the local speed of sound.

$$V = M \cdot a \tag{2.13}$$

$$a = \sqrt{\gamma \cdot \frac{P}{\rho}} \tag{2.14}$$

Note that the density value used in the preceding equations was a local density, which could be determined through isentropic flow relationships. By assuming the ambient conditions in the lab were stagnation conditions, the stagnation density could be found using the ideal gas law.

$$\rho_o = \frac{P_{amb}}{RT_{amb}} \tag{2.15}$$

Then, using the isentropic relation given in Eq. 2.8 and the local static pressure, the local density could be found at each measurement point within the bypass region. Knowing the local density and velocity, and the discrete local area, the total mass flow could be determined by summing the individual mass flow values across the entire cross-section.

2.5.6 Area-Averaged Variables

In order to determine average values of pressure or Mach number within a given measurement plane, a simple average of the derived variables would not provide an accurate representation of the true average. Instead, a weighted average, based on local cross-sectional area was required to account for variable measurement spacing throughout the test region. For instance, total pressures measured within the boundary layers were expected to be different from those measured in the core flow. However, because the measurement spacing was more highly-resolved near the tunnel walls, the local cross-sectional area was less; therefore, the boundary-layer pressures contributed less to the overall average.

Using the procedure described by Eq. 2.16, an average value of flow variable *x* could be determined across the area of the test region.

$$\bar{x} = \frac{1}{A}\sum_{i=1}^{n} x_i A_i \tag{2.16}$$

As a measure of variance within a given measurement plane, the weighted standard deviation was formulated for each plane using a combination of the measured value residuals and the local area ratio, as described by Eq. 2.17.

$$\bar{\sigma} = \sqrt{\sum_{i=1}^{n} (x_i - \bar{x})^2 \left(\frac{A_i}{A}\right)^2} \tag{2.17}$$

2.5.7 Flow Direction

When collecting data with the five-hole pressure probe, five discrete pressures were measured from the conical probe tip while it was immersed in the flowfield. Using a thorough calibration procedure, the relationship between these pressure readings could then be used to determine flow qualities such as total and static pressures and yaw and pitch angles. Details of the five-hole probe calibration can be found in Appendix B. Using a similar procedure, with the probe calibration constants known, yaw and pitch flow angles relative to the probe tip were then calculated as well as predictions of total and static pressures. Due to the orientation of the probe throughout the experiment, yaw and pitch angles corresponded to azimuthal and radial flow, respectively.

Bias in the flow angle predictions were expected from the five-hole probe, primarily due to its placement within the traversing mechanism. In order to remove this bias, the flow within a given measurement plane was assumed to be symmetric about the with an average yaw angle of zero. Utilizing this assumption, the average yaw angle measured by the probe was taken as the bias, and the true local flow angle was taken as the relative angle with respect to this bias.

In order to transform yaw and pitch angles to vector fields representing the flow direction, the local flow angles were used in conjunction with the total Mach number magnitude to determine the in-plane Mach number components at a given measurement point. Using trigonometric relations and the flow angle schematic shown in Fig. B.1a, the azimuthal and radial components of the Mach number were determined and are given in Eqs. 2.18 and 2.19.

$$M_\theta = \frac{M \cdot \tan\beta}{\sqrt{\tan^2\alpha + \tan^2\beta + 1}} \tag{2.18}$$

$$M_r = \frac{M \cdot \tan\alpha}{\sqrt{\tan^2\alpha + \tan^2\beta + 1}} \tag{2.19}$$

Chapter 3

Results and Discussion

This chapter focuses on the outcome of the experiments conducted within the simulated bypass flow region. In addition to presenting the data, an analysis will be completed in order to examine the features present in the annular flow and compare the benefits and drawbacks of using guide vanes to redirect the flow around the gearbox fairing.

3.1 Initial Observations

Before high resolution pressure data were collected within the bypass region, several tests were completed with the baseline model in order to determine initial flow parameters related to the performance of the tunnel and bypass model upstream of the primary bypass flow region.

3.1.1 Upstream Inner Boundary Layer

While collecting preliminary total pressure data at the upstream measurement plane, several azimuthal measurement stations seemed to lack a boundary layer along the model centerbody. Fig. 3.1 illustrates the inability of the total pressure probe to resolve a pressure gradient along the inner wall of the annulus (in the "clean" configuration), which indicated that the probe tip was not entering the thin boundary-layer profile growing along the model centerbody. Due to this finding, the behavior of the upstream boundary layer was unknown and a determination could not be made as to whether it had transitioned from a laminar to turbulent flow regime. As briefly mentioned in Section 2.2.2.1, a trip strip with roughness elements was attached to the aft portion of the contraction cone, slightly upstream of MP0, in order to force boundary-layer transition and provide a consistent, turbulent boundary layer at the inlet of the test region.

Fig. 3.1 depicts the change in boundary-layer behavior with the added strip of roughness for the "tripped" model case. As intended, the inner boundary layer generated with the trip strip exhibited the characteristics of a turbulent boundary layer, with a steep total pressure gradient and a relatively abrupt change in pressure as it reached the core flow. This behavior indicated that the roughness elements had ensured laminar to turbulent boundary-layer transition at the upstream measurement plane. Additionally, at this specific azimuthal location, the inner boundary-layer thickness increased to 0.08 inches using the microbead roughness elements, compared to being less than 0.03 inches for the "clean" model case. This was a significant increase given that the trip strip was located only 2 inches upstream of MP0. With the confirmed effectiveness of the trip strip located on the contraction cone, the turbulent boundary-layer behavior along the model centerbody was expected to remain consistent through all of the experiments in order to effectively compare results between test runs, without considering the effects of an unsteady boundary-layer transition point.

3.1.2 Upstream Static Pressure Variation

Using the 35 upstream static pressure ports along the wall of the fixed upstream test section, the axial variation in static pressures was measured in order to examine the flow as it contracted around the model sections. Referring to Fig. 3.2, the axial position of these static pressure ports enabled an analysis of the flow around the contraction cone and partially through the flow diverter section.

As a comparison for the measured static pressure values, an ideal pressure variation was obtained using area ratio analysis from isentropic flow relations. This ideal case represented a flow in which there existed no total pressure losses and the static pressure variations were quasi-one-dimensional and solely due to the change in area of the flow channel. Using isentropic flow analysis, the change in cross-sectional area of a flow region is related to the local Mach numbers, as shown in Eq. 3.1.

$$\frac{A_1}{A_2} = \frac{M_2}{M_1} \frac{\left(1 + \frac{\gamma-1}{2} {M_1}^2\right)^{\frac{\gamma+1}{2(\gamma-1)}}}{\left(1 + \frac{\gamma-1}{2} {M_2}^2\right)^{\frac{\gamma+1}{2(\gamma-1)}}} \tag{3.1}$$

Then, using the Mach number/pressure ratio relation of Eq. 2.11, the downstream pressure variation was predicted based upon the axial variation in cross-sectional area within the test section. In order to initialize this isentropic prediction model, the first wall static pressure measurement was used in conjunction with the ambient lab stagnation pressure; then, the downstream pressure ratios were developed from this initial data point. Fig. 3.2 illustrates the axial variation of pressure ratios from measured static pressures compared with those predicted using an isentropic flow model. Note that an average of the static pressures measured along the upper and lower portions of the test section was used to depict the experimental values.

The two curves shown in the figure indicated that the incoming flow behaved in an isentropic manner. At two segments within the flow, the curves seemed to deviate slightly; however, the discrepancy was most likely explained by the obstruction caused by the struts on the contraction cone as well as the obstructed measurement ports along the bottom side of the tunnel. The quasi-one-dimensional flow assumption may have also failed due to the complex model geometry encountered through this region. Nevertheless, the strong overall agreement indicated a nearly-isentropic flow around the contraction cone and into the blocked annulus. Similar upstream analysis was also completed for the vaned model configuration. Again, only small deviations were noticeable between the two curves, mostly in the downstream section near the guide vanes. Overall, the two separate tests confirmed that the flow behaved in an isentropic manner through the upstream geometry, with little to no losses through the forward portion of the guide vanes. While this method was a simple way to investigate the general behavior of the flow, detailed pressure analysis was required in order to examine the flow features within the test region.

3.2 Baseline Flow

Once the preliminary investigations were complete, a full characterization of the bypass flow region could begin. In order to gain a general understanding of the flow, total and static pressures were collected at each of the measurement planes, allowing for flow speed calculations and a determination of boundary-layer growth throughout the constant-

area blocked section. Then, focus was placed upon determining flow directionality characteristics, both within the core flow as well as along the surface of the model.

3.2.1 Wall Static Pressures

As a first indication of the flow behavior within the bypass region, static pressures were collected along the outer wall of the rotating section. Due to the spacing of the pressure ports, a relatively coarse resolution of the axial pressure variation was provided within the rotating section. However, with the highly-accurate rotation capabilities, an azimuthal spacing of 1.25 degrees was used to fully map the static pressure profile along the outer wall of the test section and capture any azimuthal variations within the flow.

Fig. 3.3 presents an unwrapped illustration of the variation in wall static pressure coefficients throughout the constant-area blocked section. Note that the top center location will be referred to as the zero-degree position, with clockwise and counter-clockwise angular motion being positive and negative rotation, respectively (when viewing the test region from an upstream vantage point.) Also, an axial location of zero refers to the first measurement plane (MP1) within the constant-area blocked section. Therefore, the contour mapping depicts the static pressures from the beginning of the constant-area blocked section to the inlet of the downstream guide vanes, bounded by the gearbox blockage at ±100 degrees.

As shown in the figure, the flow seemed to be symmetric about the vertical mid-plane, with azimuthal variations being much more severe at the forward measurement locations. Also, at the forward-most measurement plane, the low pressure regions adjacent to the fairing seemed to indicate high-speed regions as the flow was accelerated around the flow diverter section of the gearbox blockage. However, this required confirmation by the total pressure profiles, since the total pressure would indicate whether the flow had separated or if the flow had, in fact, accelerated within these regions.

Farther downstream within the test region, the static pressures assumed better uniformity as the flow approached the aft guide vanes. In fact, the range in static pressure coefficients across the annular arc at MP5 was approximately 85 percent less than that at MP1. This downstream trend toward static pressure uniformity was clearly illustrated in Fig. 3.3. An interesting feature of the static pressure distribution near the aft guide vanes

was the low pressure regions that emerged near the ±100-degree locations. Although similar behavior was observed on both sides of the model, the magnitudes of these low pressure regions were not perfectly symmetric.

At the upstream measurement plane (MP0), static pressures were collected from all 30 wall port locations, which were equally-spaced around the circumference of the test section. Fig. 3.4 illustrates the azimuthal variations in static pressure coefficient. As with the pressure readings within the constant-area blocked section, these data portrayed symmetric flow behavior about the vertical mid-plane. At this measurement plane, lower pressures were measured along the upper side of the model (near the 0-degree location), with higher pressures measured along the lower side of the model (near the ±180-degree location). This suggested that the flow speed was diminished ahead of the gearbox blockage; however, conclusive results could not be established without accompanying total pressure measurements.

3.2.2 Total Pressure and Mach Number Profiles

After the static pressures were measured throughout the test section, total pressure profiles were collected at each of the ten measurement planes in an attempt to characterize the total pressure losses encountered within the flow in addition to the Mach number distribution within the test annulus. Because small-scale flow features were not anticipated within the constant-area blocked section of the baseline configuration, a modest, 5-degree azimuthal spacing was used to capture the total pressure profiles away from the gearbox. Since boundary layers were expected to grow along the gearbox fairing, however, the azimuthal measurement spacing was more highly-resolved within 3.5 degrees of the blockage components. For the upstream measurement plane, the flow was expected to be generally uniform; therefore, the 12-degree spacing was anticipated to provide sufficient measurement resolution at this point in the flow region. With regard to the radial variations in total pressure, measurements were more highly-resolved near the inner and outer walls in order to capture the pressure gradients associated with the boundary-layer profiles. This measurement scheme allowed for a full characterization of the azimuthal and radial variations in pressure throughout the bypass flow region.

3.2.2.1 Upstream Measurement Plane

Shown first in Fig. 3.5 is the nondimensionalized total pressure contour for the upstream measurement plane. At this point in the test section, the core flow (which excludes the boundary layers) exhibited little to no losses in total pressure from the ambient pressure in the lab. An exception to this was the presence of minor disturbances observed at the ±45 and ±135-degree locations, where the wakes of the contraction cone struts could be discerned in the contour plot. These disturbances were anticipated to have a minor overall effect on the flowfield due to the streamlined nature of the struts. Therefore, total pressure deficits were only found to be significant within the boundary-layer flows along the inner and outer walls of the test region.

In general, the measured boundary layer was thicker along the outer wall of the test section, when compared to that along the model centerbody. This was a result of the contraction cone being designed such that the boundary layer growth was minimal once the model centerbody reached its full diameter and the full annular flow was established. Also, the boundary layer along the outer wall began to develop farther upstream within the tunnel inlet, whereas the inner boundary-layer growth began no earlier than the tip of the contraction cone.

An interesting feature of the inner boundary-layer profile was the apparent lack of a measured boundary layer along the lower half of the model. Conversely, along the upper portion of the model, where the effect of the trip strip had been investigated previously, the boundary-layer profile seemed to be fully captured. This could most likely be explained by a slight vertical displacement of the model during full-speed operation of the tunnel. Considering the overall cantilever design of the test model, and the distance of the upstream measurement plane from the primary model support struts, small vertical displacements could be caused by forces imposed along the length of the model. Because the bypass design incorporated an annular blockage within the test section, the flow above the model was accelerated, which acted to decrease the static pressure in this region. Therefore, assuming the upper side of the model was exposed to lower pressures than the lower side, a net upward force would be imposed upon the model.

This theory was tested using a depth gauge inserted at various points around the circumference of the model. These investigations confirmed that the centerbody was

shifting vertically within the test section during operation of the blower, causing it to be misaligned from the tunnel centerline (albeit by only 1 or 2 millimeters). As seen from Section 3.1.2, the upper boundary layer was less than 0.08 inches (2 mm) thick; therefore, this slight vertical shift enabled the lower boundary layer to avoid detection while using the same radial spacing throughout each of the measurement ports. Nevertheless, the boundary layer was assumed to be equivalent along the upper and lower surfaces of the model.

Because the total pressure profile within the core flow was essentially axisymmetric throughout the test annulus, the Mach number profile was dominated by the non-axisymmetric behavior of the static pressure measurements. Shown in Fig. 3.6 is the Mach number contour for the upstream measurement plane, which confirms lower flow speeds along the bottom side of the model, which was directly upstream of the gearbox blockage. Since the flow was subsonic in this upstream portion of the bypass region, the effect of the fairing had propagated upstream, which exposed the lower half of the annular flow to the downstream blockage, causing it to be slower than the unrestricted flow along the top of the model. In fact, within MP0, the speed of the upper core flow reached Mach 0.31, while the maximum speed of the lower core flow only reached Mach 0.24, resulting in an area-averaged Mach number of 0.27.

3.2.2.2 Constant-Area Blocked Section

Within the rotating portion of the test section, the total pressures were much more resolved than within the upstream measurement plane. Shown in Fig. 3.7 are contours of the normalized total pressure through the six primary rotating measurement planes. As with MP0, the core flow regions throughout the constant-area blocked section exhibited insignificant total pressure losses, with the deficits being located within the boundary-layer regions.

As expected within this portion of the test region, the boundary layers along the model centerbody, outer tunnel wall, and gearbox fairing grew as they developed downstream. While difficult to see in contour plots, a slight increase in boundary-layer thickness was present at the ±30 and ±85-degree locations within the flow region. These disturbances were determined to be remnants of the upstream struts, but, again, seemed to have little effect on the core flow. Their effect was much more pronounced toward MP6,

where the two lower disturbances developed into relatively large features within the outer wall boundary layer.

A notable feature of the boundary layers along the gearbox fairing was their relative absence at MP1. This was to be expected, due to the geometry of the flow diverter section, which accelerated the flow around the gearbox blockage. Since the flow along this portion of the model was being constricted, the boundary layers developing along the gearbox fairing were exposed to a favorable pressure gradient, which allowed them to remain relatively thin as they progressed downstream. Then, at MP1, where the cross-sectional area of the flow region became constant, the favorable pressure gradient was eliminated, causing the boundary layer to grow in a typical manner through the remaining measurement planes.

Another interesting feature illustrated by these contours was the presence and growth of small regions of total pressure deficit at the ±100-degree locations (both along the outer wall and the centerbody). At MP1, these disturbances were relatively small and were confined to the corner junctions of the geometry. As they progressed downstream, however, they expanded in size, along with the boundary layers. Based on their characteristics and locations, these disturbances were assumed to be formed by vortical structures at the fairing/centerbody and fairing/outer wall junctions. Due to the complex geometry of the annular blockage, the vortices may also have been exaggerated by the interaction of the flow as it converged into the constant-area blocked section.

Using the wall static pressures collected previously, the total pressure profiles were then converted to Mach number contours, as shown in Fig. 3.8. Note the change in scale from the upstream measurement plane. As expected, based upon the trends in the outer wall static pressure contour, the Mach numbers in MP1 exhibited a much larger range than those farther downstream. In fact, the core Mach numbers in MP1 ranged from 0.55 to 0.75, while the range at MP4 was narrower, with Mach numbers ranging between 0.62 and 0.65. Nevertheless, throughout the six measurement planes, the area-averaged Mach number remained consistent at approximately 0.61.

As the flow approached the end of the primary test region, near the aft guide vanes, an azimuthal gradient reemerged. Within MP5 and MP6, the flow seemed to reaccelerate within the regions near the gearbox fairing. The variations in Mach numbers observed at

these planes were not as symmetric as those farther upstream, but flow acceleration was present on both sides of the model. The cause of these acceleration regions was not immediately apparent and was initially assumed to be a result of the downstream geometry. Because MP6 was designed to be the end of the subsonic test region, the supersonic, aft bypass facility contained an analogous measurement plane that could be used for comparison (see Hortensius).[22]

Using Mach number data collected in the present experiment, the speed profile behavior of MP6 was compared with the equivalent plane for an unvaned, baseline configuration in the aft bypass experiment. Although the current study contained short, aft guide vanes, the overall flow features were expected to be similar between the two tests since the separation region behind the gearbox blockage was extensive in both cases. As seen from results obtained in the aft bypass experiment in Fig. 3.9, the flow tended to accelerate near the gearbox fairing as it approached the aft portion of the gearbox blockage. Note the change in scale from Fig. 3.8 due to the aft experiment reaching higher speeds within the constant-area blocked section. Because similar behavior was observed in both experiments, the acceleration was assumed to be a product of the blocked annular flow geometry in conjunction with a large trailing separation region.

3.2.3 Five-Hole Probe Profiles

In an attempt to examine flow velocity, and especially flow directionality characteristics, within the bypass flow region, the five-hole probe was used to collect data throughout the constant-area blocked section. Since the aim of these measurements was to determine an overall trend within the flowfield, the measurement spacing for the five-hole probe was less resolved than that used for the total pressure probe. Also, because the probe tip diameter was large with respect to the radial extent of the flow region, the gradients present in the inner and outer boundary-layer profiles were expected to result in measurement errors from the probe. Therefore, a coarse measurement spacing was used to characterize the flow direction and focus was placed primarily within the core flow regions.

Shown in Fig. 3.10 are the in-plane Mach number vectors within each of the six primary measurement planes. These values were derived from the five-hole probe measurements through the calibration procedure described in Appendix B. The direction

and magnitude of the Mach vectors were obtained by projecting the total flow vectors, with magnitudes of Mach number, onto the measurement planes (see Section 2.5.7). As mentioned previously, bias was expected in the yaw angle measurements due to the physical orientation of the probe within each measurement plane. Table 3.1 outlines the yaw angle bias at each of the measurement planes. These range of values presented here illustrate the variability of the probe placement when mounted onto the traverse mechanism.

Table 3.1 Yaw misalignment of the probe for the baseline configuration.

MP1	MP2	MP3	MP4	MP5	MP6
-0.50°	+0.15°	-0.65°	-1.20°	+0.40	-1.70°

Similar to the behavior of the Mach number profiles in this region, the distribution of azimuthal flow became more uniform in the downstream measurement planes, as the flow progressed through the constant-area blocked section toward the aft guide vanes. Nevertheless, the data depicted a consistent pattern throughout the test region, indicating that the majority of the flow was being directed toward the top center location of the flow annulus. Within MP1, for example, this behavior was much more defined, with 0-degree yaw angles near the top center location of the flow annulus and regions with 6-degrees of yaw near the gearbox fairing. As the flow progressed downstream, the flow near the gearbox fairing began to reverse direction and move toward the fairing, with a slight bias in the clockwise direction, indicating asymmetric behavior near the aft guide vanes. Radial flow predictions also showed a consistent pattern within the test region, with the flow moving toward the centerbody in all of the measurement planes. Nevertheless, as anticipated, the pitch angle magnitudes were typically much smaller than the yaw angles and remained relatively consistent throughout all six measurement planes.

Overall, the initial trend of the flow toward the top center location was interpreted to be an effect of the flow diverter section redirecting the flow toward the upper side of the model. Based upon the azimuthal distribution of static pressures within the test region, the flow was initially expected to move toward the gearbox fairing, especially within the first two measurement planes, where the pressure gradients were most intense. Based upon the five-hole probe measurements, however, this was not the case. Instead, the flow seemed to

be influenced by momentum properties, rather than the measured pressure variations. Because the flow was redirected and accelerated by the flow diverter section, the core flow gained angular momentum toward the top center of the annulus. Therefore, the flow seemed to be more strongly influenced by its angular momentum and maintained the trajectory imparted onto it by the flow diverter section.

In order to validate the data collected by the five-hole probe, the experimental data were compared with a computational model of the bypass flow. Because the true bypass design included forward guide vanes within the flow path, a previous computational model was used for this comparison. This model is detailed in Chiles and Danko and was based upon the original bypass model design, with a 110-degree gearbox blockage and no forward or aft guide vanes.[19,20,29] Although the current model design utilized a 160-degree fairing, the overall flow characteristics were expected to behave in a similar manner around the curvature of the flow diverter and around the blockage components. By examining data from this CFD simulation, the core flow behaved similarly to the experimental data presented above, with an overall trend toward the top center location of the annular arc (the 0-degree position). This comparison provided a valuable validation between the computational and experimental tests, which could prove to be valuable for use with the vaned model configuration.

3.2.4 Flow Visualization

In an attempt to further verify the flow direction characterisitics measured by the five-hole probe, surface oil-flow visualization was conducted within the constant-area blocked section. These tests were completed primarily to illustrate the directional characteristics of the flow along the model centerbody in a comprehensive, time-averaged manner.

In order to optimize the flow visualization process, small dots of fluorescent oil/dye mixture were placed on the model surface on a 1/4-inch grid at every other grid point. Because small-scale features were not likely to be present for the baseline model configuration, this particular spacing was chosen to best illustrate the overall flow behavior. As discussed previously, the dots were intended to respond to shear stresses encountered on the model surfaces and to produce a streak pattern indicating flow

direction. Shown in Fig. 3.11 is an overall illustration of the results from the flow visualization experiment. Note that the test region was extended slightly upstream of the constant-area blocked section in an attempt to reduce the effects of the small step created by the thickness of the contact paper and to capture the flow behavior around the curvature of the flow diverter section.

The resulting fluorescent oil streaks provided valuable insight into the flow features along the model surface, including the overall flow structure along the model centerbody and the presence of vortical structures along the gearbox fairing. At first glance, one of the most prominent features of the resultant oil patterns was the behavior of the flow along the model centerbody. In fact, adjacent to the flow diverter section, the flow experienced a high level of curvature. Then, as the flow reached the region of maximum blockage, the oil patterns were directed toward the gearbox fairing (to a much higher degree near MP1 and MP2). This result seemed to contradict the data obtained with the five-hole probe, which indicated flow direction toward the top center location of the flow region. Nevertheless, the oil patterns seemed to be more compatible with the distribution of static pressures along the outer wall of the test section, which indicated lower pressures directly adjacent to the gearbox fairing and higher pressures near the 0-degree location within the bypass region.

In order to further investigate the flow behavior along the model centerbody, results from the the aforementioned computational simulation were compared to the oil flow patterns along the model surface.[20,29] Fig. 3.12a illustrates simulated streamlines of shear stress on a similar baseline model with 110 degrees of blockage. Although the amount of annular blockage varied between the computational and experimental models, the overall trends were expected to provide an effective comparison tool. In fact, by comparing Fig. 3.11 and Fig. 3.12a, the streamline curvature along the downstream portion of the flow diverter section was present in both cases, with the flow curving around the fairing contour and moving toward the fairing throughout the rest of the constant-area blocked section. Because the surface behavior differed significantly from the directionality of the core flow, further investigation was focused toward this seemingly contradictory result. Shown in Fig. 3.12b are the representative in-plane flow vectors developed through the computational simulation. These data are presented at a plane comparable to MP1, depicting only the region adjacent to the gearbox fairing. With a closer look at the

simulated in-plane flow vectors, the flow indeed seemed to flow upward in the core regions, and downward near the model centerbody.

From this CFD solution, there appeared to be a flattened vortex structure at the edge of the inner boundary layer, where the azimuthal flow abruptly changed direction. This behavior was observed along both the model centerbody and, to a lesser extent, along the outer wall of the bypass annulus. Because the surface flow behavior was confirmed along the model centerbody, the trends along the outer wall were expected to behave similarly, as predicted by the computational simulation. In order to justify this behavior, focus was placed on the factors influencing the flow in this region, including (1) the static pressure distribution within the test region, (2) the angular momentum of the annular flow, and (3) the effect of the boundary layer.

As mentioned previously, the flow within the constant-area blocked section was initially expected to be directed toward the gearbox fairing, where the pressures were, in general, lower than those at the 0-degree location of the flow annulus. However, measurements from the five-hole probe indicated that the core flow was being directed toward the top of the test region and, therefore, possessed upward angular momentum imparted by the flow-diverter section. Within the inner and outer boundary layers, which are inherently defined as regions with momentum deficit, the flow may have lacked the angular momentum necessary to overcome the azimuthal static pressure gradient and, instead, began to move toward the gearbox fairing.

In addition to the flow patterns along the model centerbody, the wall of the gearbox fairing also exhibited interesting behavior. Because this region seemed to contain complex flow features, dots of oil/dye mixture were placed in 1/8-inch azimuthal increments and 1/4-inch longitudinal increments to better capture the flow structure. Shown in Fig. 3.13 is a detail of the flow visualization completed near the centerbody/fairing junction with the higher-resolution grid spacing. At this junction, the surface patterns seemed to suggest the presence of vortical flow, with a downward motion along the centerbody and an outward motion along the fairing wall. Then, near the outer wall, the flow along the fairing was also directed toward the radial center of the annular arc region. Without flow visualization completed along the outer wall of the test section, the surface flow was expected to behave similarly to that on the centerbody, with a downward trend. Therefore, at this location

within the test section, the flow visualization indicated the presence of two counter-rotating vortices at the fairing junctions, both along the centerbody and the outer wall. This type of behavior was also supported by the computational in-plane velocity vectors presented in Fig. 3.12b and was expected to be present at the -100-degree location within the test section due to flow symmetry.

Overall, since the five-hole probe was not seen to be accurate within the boundary-layer flows, oil-flow visualization was able to provide a direct view of the flow along the model surface. The details exposed by the oil streaks seemed to provide a useful illustration of the surface shear stress patterns and provided insight into the complex interaction between the core and boundary-layer flows. They also validated computational results obtained from the original 110-degree fairing design. While the surface patterns on the baseline configuration were found to be interesting and useful, similar analysis on the vaned model was expected to reveal complex flow patterns along the model centerbody and the guide vanes themselves, as a supplement to the five-hole probe measurements within the core flow regions.

3.3 Guide Vanes

With the baseline measurements completed, focus was placed on characterizing the effects of the guide vanes within the bypass flow. Again using total and static pressure readings, five-hole probe data, and surface flow visualization, the constant-area blocked section was thoroughly examined. In addition to characterizing the boundary-layer growth along the model centerbody and the gearbox fairing, shear layers and wakes created by the guide vanes were also studied, with a specific focus on their impact on the overall performance of the bypass duct.

3.3.1 Wall Static Pressures

As with the baseline model configuration, the static pressures were collected along the outer wall of the constant-area blocked section in order to provide a general depiction of the flow as it left the guide vanes. Due to the expectation of additional flow features caused by the vanes, the azimuthal spacing was reduced to 1 degree in order to better resolve the pressure gradients.

Shown in Fig. 3.14 is an unwrapped view of the outer wall of the test section, which illustrates the variation in static pressure coefficients within the constant-area blocked section. As a reminder, MP1 corresponds to the exit plane of the forward guide vane channels, while MP6 represents a plane immediately upstream of the aft guide vanes. The static pressure distribution was found to be relatively symmetric about the vertical mid-plane with overall characteristics similar to those from the baseline configuration (see Fig. 3.3). Regions of low pressure were again apparent near the gearbox fairing (±100-degree locations), with higher pressures near the top center of the test region (0-degree location). Assuming that the static pressure distribution provided a first-order interpretation of the flow speed (neglecting total pressure losses), the flow adjacent to the gearbox fairing seemed to have accelerated to a greater extent than the rest of the flow. Then, as the flow progressed downstream, the azimuthal variation in static pressures tended to decrease, indicating a more uniform flowfield as the flow approached the aft guide vanes. This trend continued until MP6, where low pressure regions appeared in the data near the ±100-degree locations, similar to the asymmetric behavior observed with the baseline model configuration. Because both configurations exhibited similar behavior at this measurement plane, this effect was assumed to be a result of the downstream model geometry, aft base flow effects, or blower disturbances propagating upstream into the primary test region, rather than a direct result of the upstream model geometry.

An additional feature present in the vaned model static pressure contour was the presence of intermittent discontinuities in the azimuthal pressure variations. While difficult to discern from the contour plot, the most evident of such discrepancies occurred near the -20 and ±40-degree locations, with less apparent distortions occurring every 20 degrees. These discontinuities in the contour data originated from the azimuthal positions of the forward guide vanes and, therefore, indicated disturbances caused by their wakes and shear layers as they propagated through the constant-area blocked section. Nevertheless, static pressure readings are not an effective method of characterizing regions with momentum deficit. Therefore, total pressure readings were required for a full examination of the wake and shear layer profiles aft of the guide vanes.

As with the baseline model, a survey of static pressures was also collected at 30 azimuthal locations within the upstream measurement plane in order to provide a

representation of the incoming flow. Fig. 3.15 illustrates this azimuthal pressure distribution, which, in general, displayed relative symmetry about the vertical mid-plane. There were three interesting features of this distribution that could be directly compared with the static pressure distribution for the baseline configuration presented earlier in Fig. 3.4. First, the range in pressure coefficients around the circumference of the test section was reduced by an order of magnitude. In fact, for the vaned configuration, the range was from -0.024 to 0.028, while the range for the baseline configuration was from -0.22 to 0.26. This illustrated a significant improvement in upstream flow uniformity with the guide vanes installed, indicating that the vanes acted to diminish the upstream effect of the gearbox blockage and distributed the upstream static pressures more evenly throughout the flow annulus.

Second, the overall trends of the vaned pressure distribution differed from the baseline configuration in that high pressures were located at both the 0-degree location and the ±180-degree locations, with the lowest pressures present upstream of channels 4 and 4'. Assuming the static pressures were a preliminary indication of flow speeds at MP0, the flow was expected to be nearly axisymmetric, with a minor increase in flow speed ahead of channels 4 and 4', with slightly lower speeds near the top and bottom of the model. Nevertheless, total pressure data were required at this measurement plane in order to accurately portray the Mach number distribution. The third and final feature of this distribution was the apparent randomness of the pressure coefficient data. Rather than being discontinuities in the data, however, this was due to the significantly decreased range in static pressure coefficients, which exaggerated the small variations between measurement points. In fact, using uncertainty analysis as presented in Appendix C, uncertainties in the pressure coefficients were of the same order as the measured values, indicating that the discontinuities may have been due solely to measurement errors.

3.3.2 Total Pressure and Mach Number Profiles

With the forward guide vanes integrated into the model, the flow features were expected to be much more complex than those seen in the baseline case. Therefore, within the constant-area blocked section, the azimuthal spacing of the measurements was reduced in order to fully capture the downstream effects of the vanes. At the upstream

measurement plane, the total pressures were also surveyed in order to define the azimuthal Mach number distribution at the inlet of the guide vanes.

3.3.2.1 Upstream Measurement Plane

With the overall symmetry present in the static pressure measurements, along with negligible total pressure losses at MP0, total pressures were expected to be symmetric about the vertical mid-plane. Therefore, total pressure profiles were collected ahead of five of the ten flow channels and were mirrored for the remaining channels. Shown in Fig. 3.16 is the contour of nondimensionlized total pressure at MP0, which demonstrated similar characteristics to the same measurement plane in the baseline configuration (see Fig. 3.5). In general, the outer wall boundary layers were again larger than those along the model centerbody. In this case, however, the boundary layer was present around the full circumference of the model. In contrast with the baseline configuration, the guide vanes acted to fix the model within the test section, preventing the centerbody from shifting vertically during operation of the blower. Like the previous configuration, minor disturbances were again present in the data at the ±45 and ±135-degree locations; however, these were not visible in the contour plot and were expected to cause negligible disturbances within the overall flowfield.

Using the static pressure measurements collected separately, without the probe in the flowfield, the upstream Mach number distribution was calculated and is shown in Fig. 3.17. As expected from the distribution of static pressures at this plane, the Mach number distribution was much more uniform than that measured with the baseline configuration presented in Fig. 3.6. In order to directly compare the two models, both Mach number profiles were plotted with the same scale. For this case, the maximum core Mach number was found to be 0.28, while the minimum core Mach number was 0.27. This resulted in an area-averaged Mach number of 0.27, which also accounted for the boundary-layer flow regions.

3.3.2.2 Constant-Area Blocked Section

Before substantial time was invested in collecting high-resolution total pressure profiles within the rotating portion of the test section, a preliminary total pressure survey was collected at the mid-radial location (R*=0.50) across the annular arc at each of the six

measurement planes. The azimuthal spacing for these initial investigations was set at 1 degree in order to determine an appropriate spacing for the high-resolution tests. Shown in Fig. 3.18 is a comparison of the total pressure profiles at each of the measurement planes. From these profiles, the wakes of each of the guide vanes were immediately apparent, with little, if any, losses between the vane wake structures. As would be expected in the unvaned region between the forward and aft vanes, the wakes tended to expand as they propagated from MP1 downstream through MP6. Also, the boundary-layer regions along the gearbox fairing (near the ±100-degree locations) grew substantially through MP6. In general, the overall behavior of the wake regions was symmetric throughout the constant-area blocked section.

These preliminary total pressure data were used to determine appropriate measurement spacing within the constant-area blocked section and, in order to provide consistency within the test region, the measurement spacing was to be identical for each plane. Although the vane wake regions were found to be relatively small at MP1, they occupied a large portion of the flow annulus by the time they reached MP6. With this in mind, and while also considering the potential for complex flow features near the vane/centerbody junctions, the azimuthal spacing remained at 1 degree for the high resolution tests. When combined with a total of 13 radial measurement points, the overall spacing allowed better resolution near the inner and outer boundary-layer regions, while also capturing the features formed by the guide vanes. (For reference, an example of the measurement spacing can be seen in Fig. 2.21.)

Fig. 3.19 depicts the contours of normalized total pressure throughout the constant-area blocked section and can be compared with similar contours for the baseline configuration presented in Fig. 3.7. From the vaned total pressure data, the effects of the guide vanes were immediately observed, with a pressure deficit created aft of each of the vanes. Within MP1 specifically, these wake regions were clearly defined, while the core flow regions near the center of the flow channels exhibited negligible total pressure loss from the reference atmospheric pressure. In addition to the radial wake structures created by the vanes, additional features were also observed near the mid-radial location within the annular arc. Attached to the wake structures were regions of total pressure deficit, which tended to decrease in size toward the top center location. Also at MP1 was a small region

of total pressure deficit near the gearbox/centerbody junction on both sides of the model. These protrusions seemed to indicate the presence of longitudinal vortical flow structures, which possess total pressure deficits at their cores.

As the flow progressed downstream, several trends were evident with regard to the total pressure profiles. First, the overall vane wake structures became more distorted and tended to expand as the flow mixed within the constant-area blocked section. Second, the position of wakes did not remain constant. In fact, the inner portions of the wakes moved toward the gearbox fairing, while the outer portions moved toward the top center location of the flow region. This behavior, as in the baseline model configuration, indicated a balance between the angular momentum of the flow and the azimuthal static pressure distribution measured along the outer wall of the test section. As observed by the shifting wakes, the flow seemed to be influenced by upward momentum near the outer wall and by the static pressure distribution near the inner wall.

A third trend observed by the total pressure data was the development and expansion of the wake profiles as they propagated downstream. In general, the regions of pressure deficit attached to the wakes became less defined and moved with the wakes themselves. Also, in the second channel from the gearbox, these regions developed into hooked structures, which further indicated the presence of longitudinal vortices at these locations within the flow. The last major observation taken from Fig. 3.19 was the development of the boundary layer along the gearbox wall. As identified previously, the small features near the gearbox in MP1 expanded to the entire width of the annulus and grew substantially by MP6, where they each occupied nearly 10 degrees of the annular arc. Due to their shape in MP1, these disturbances along the gearbox were also thought to indicate the presence of vortical flow structures, which were perhaps interacting with the growing boundary layer. However, this assumption could not be substantiated without accompanying five-hole probe data.

Using the total pressure profiles, in conjunction with the static pressure distribution along the outer wall, Mach number profiles were calculated and are presented in Fig. 3.20. As expected from the static pressure distribution, the range in core Mach numbers was much larger at MP1 than farther downstream at MP5. In fact, the range in upstream core Mach numbers was 0.55 to 0.78, whereas the range downstream was 0.63 to 0.66. Then,

similar to the baseline configuration, the flow near the gearbox began to reaccelerate within MP6. Again, the downstream acceleration regions did not behave entirely symmetrically; however, they were present on both sides of the model. Because the aft geometry included the same small guide vanes and a large separation region aft of the truncated gearbox, the acceleration behavior was similar to that observed in the baseline configuration (see Fig. 3.8). Therefore, the reacceleration regions were attributed to the downstream geometry and were not used to make any conclusions regarding the upstream model geometry. Note that for the vaned model configuration, area-averaged Mach numbers within the constant-area blocked section remained consistent near 0.60. This was a slight decrease from similar measurements in the baseline configuration, but this discrepancy was most likely due to the losses encountered within the vane wake regions.

3.3.3 Five-Hole Probe Profiles

In addition to the total pressure characteristics, flow directionality was expected to be significant with the guide vanes present in the bypass flow region. Shown in Fig. 3.21 are the in-plane Mach vectors throughout the constant-area blocked section. As with the baseline configuration, yaw angles were biased due to the placement of the probe in the traverse mount. Therefore, the average yaw angles were found for each plane and are presented below in Table 3.2. By removing this bias from each measurement, the flow was assumed to be symmetric about the vertical mid-plane, with an average yaw angle of zero through any given measurement plane.

Table 3.2 Azimuthal misalignment of the probe in the vaned configuration.

MP1	MP2	MP3	MP4	MP5	MP6
-1.20°	-0.60°	-0.20°	-0.30°	-0.80°	-0.20°

From the vectors shown in Fig. 3.21, the presence of swirling motion was apparent in the wakes of eight of the nine guide vanes, especially downstream of MP2. The exception was the topmost vane, where the flow was expected to be equivalent on both sides of the vane. Therefore, rather than an abrupt variation in pressure across Channels 1 and 1', only a shear layer was created by the adjacent boundary layers as they exited the vanes. In general, the direction of swirling motion present in the flow was symmetric and

consistent across the entire flow region, with flow along the outer wall moving toward the 0-degree location and the flow along the inner wall moving toward the gearbox fairing. Interestingly, the full swirling features did not fully-develop until MP3 and were only present as minor discontinuities within MP1 and MP2.

The position of these primary swirling features corresponded well with the location of the generated wakes. Shown in Fig. 3.22 is an example of the in-plane Mach vectors superimposed with the total pressure contours at MP2. This superposition illustrates the relationship between the locations of the apparent vortices and the wake structures. Additionally, the direction of the swirling motion seemed to correspond well with the movement of the vane wakes, with the inner portions of the wakes moving toward the gearbox fairing, the outer portions moving toward the top center of the annulus, and the portions of the wakes near the center of rotation remaining relatively stationary.

As for the core flow regions (outside of the boundary-layer and wake regions), the magnitude of the in-plane Mach numbers was reduced as the flow traveled farther downstream. Then, as the flow reached the final measurement planes, the core flow near the model centerbody began to move toward to the gearbox fairing, behaving similar to that in the baseline model configuration (see Fig. 3.10). Regardless of the change in flow direction within the core flow regions, the swirling regions within the vane wakes remained unchanged as they propagated toward the aft guide vanes. This indicated that the vortical structures were more resistant to dissipation than the flow direction characteristics within the core flow regions.

In addition to the vortical motion within the vane wakes, swirling motion was also present along the gearbox fairing. As mentioned previously, small disturbances began in MP1 and developed into relatively large structures by MP6. By studying the in-plane Mach vectors, it was apparent that these regions were, in fact, products of swirling, vortical motion rather than simply the development of a boundary layer along the gearbox. Therefore, the vaned configuration seemed to have induced a large longitudinal vortex along the gearbox that was not present in the baseline configuration.

3.3.4 Flow Visualization

As a method of confirming and further interpreting the data measured by the five-hole probe, surface oil flow visualization was performed on the model within the test region. Due to the presence of the guide vanes, however, the region of investigation was extended far upstream to examine the flow behavior at the inlet of the channels, along the entire length of the vane structures, and at the entrance to the constant-area blocked section. Shown in Fig. 3.23 is an overall view of the resultant surface oil patterns within the vaned channels. This test utilized a 1/4-inch spacing with dots located at every other grid point.

Through channels 1 and 2 near the top of the model, the flow behavior was relatively uncomplicated, as it tended to be axial in nature and followed the slight curvature of the guide vanes very well. Also, there were no noticeable features observed in the vane/centerbody junctions or at the vane entrances or exits. Within channels 3, 4, and 5, however, the complexity of the flow was heightened, with curvature of the oil patterns along the centerbody diverging from the curvature of the vanes themselves. In channel 3, for instance, the surface flow was directed toward the gearbox fairing at the exit of the channel, whereas the geometry of the channel was designed to exit parallel to the axis of the model. Due to the high-speed nature of the flow through the vane channels, some of the contact paper failed to remain attached to the model during full-speed operation, as seen in channels 4 and 5 and along the flow diverter component in Fig. 3.23. Therefore, supplemental tests were conducted near the exits of the channels, where the flow was expected to have the highest degree of curvature and complexity.

Fig. 3.24 shows the flow patterns along the underside of the two most highly-curved vanes as the flow approached the constant-area blocked section. The surface patterns at these locations indicated flow moving toward the radial center of the vanes, both from the outer wall and from the centerbody. This behavior, coupled with nearby patterns along the centerbody, indicated vortical flow structures along the vane junction regions on the underside of the vanes. Interestingly, the flow patterns on the upper side of all of the vanes behaved in an axial manner, with little to no radial tendencies. This suggested that the flow along the convex vane surfaces was more uniform than the flow along the concave vane surfaces, which corresponds well with a more basic flow around a flat plate at an angle of attack. In a simplified example such as this, flow tends to remain attached and

uniform along the pressure side of the plate and tends to separate and behave three-dimensionally along the suction side; this is consistent with the behavior observed on the complex geometry of the curved vanes.

For the flow on the centerbody surface, Fig. 3.25 shows the flow exiting channels 4 and 5 and illustrates the strong curvature toward the gearbox fairing near the exit of the vanes. (Note that, in this figure, the oil mixture was applied directly to the vaned segment of the model, which caused the streaks to exhibit a mottled effect.) There were several interesting features evident in this portion of the flow region in addition to the high degree of surface flow curvature. First, directly upstream of the gearbox curvature inflection point (the region circled in the figure), the lack of oil streaks implied a possible region of flow separation, since the oil patterns are an indication of the shear stress along the model surface. At this location, several dots of oil seemed to remain stationary, indicating little or no surface shear in this localized region. The second interesting feature in the Fig. 3.25 was the general tendency of the flow to travel toward the gearbox fairing once exiting the vanes. This behavior was similar to the centerbody surface flow for the baseline configuration, and seemed to correspond with the overall static pressure distribution within the constant-area blocked section. Third, and finally, while the majority of the exiting flow was being directed toward the gearbox fairing, there seemed to be periodic streaks that were unrelated to the surrounding flow and traveled in a more axial manner than adjacent streaks. As indicated by the arrows on the figure, these individual streaks were located directly downstream of the vanes, indicating that they were located within the vane wake regions. This further validated the presence of a highly complex flow structure immediately downstream of the vane members.

In addition to the surface flow patterns along the vanes and the model centerbody, oil streaks were also obtained along the gearbox wall. Shown in Fig. 3.26 is a detail of this region, which seemed to confirm the presence of vortical flow along the fairing/centerbody junction. Near the fairing/outer wall junction, however, the oil patterns indicated flow moving primarily in the axial direction, with minor radial motion. This suggested only one vortex present along the gearbox wall, as opposed to the two counter-rotating vortices suggested by the oil patterns on the baseline configuration (see Fig. 3.13). This behavior seemed to indicate that the outer vortex in the baseline configuration may have been caused

by an interaction between the unrestricted, upper portion of the flow and the flow deflected upward by the flow diverter component. In the vaned configuration, this interaction was eliminated since the vanes were sealed against the outer wall of the test section.

3.4 Baseline and Vaned Comparison

In general, the collected pressure data and oil-flow visualization results identified several features that differed between the baseline and vaned model configurations. The most prominent of these features were the upstream static pressure and Mach number distributions as well as the total pressure profiles within the constant-area blocked section. As mentioned previously, the range in upstream static pressures was much larger for the baseline configuration. Also, there existed larger total pressure losses through the vaned model configuration. Summarized in Table 3.3 are the area-averaged means of static and total pressure coefficients, as well as the weighted standard deviations for the same variables throughout each of the seven primary measurement planes.

Table 3.3 Static and total pressure comparison between model configurations.

	Baseline Configuration				Vaned Configuration			
Location	$\overline{C_p}$	$(\overline{\sigma})_{C_p}$	$\overline{P_{t,non}}$	$(\overline{\sigma})_{P_{t,non}}$	$\overline{C_p}$	$(\overline{\sigma})_{C_p}$	$\overline{P_{t,non}}$	$(\overline{\sigma})_{P_{t,non}}$
MP0	0.02	0.007	-0.04	0.003	0.00	0.001	-0.04	0.004
MP1	-3.46	0.023	-0.24	0.015	-3.83	0.016	-0.45	0.019
MP2	-3.50	0.014	-0.32	0.018	-3.80	0.011	-0.56	0.023
MP3	-3.63	0.007	-0.38	0.021	-3.76	0.006	-0.61	0.020
MP4	-3.55	0.004	-0.43	0.023	-3.80	0.003	-0.66	0.018
MP5	-3.64	0.003	-0.47	0.025	-3.88	0.003	-0.69	0.017
MP6	-3.70	0.005	-0.51	0.026	-4.00	0.004	-0.76	0.019

In order to better visualize total pressure losses and the static pressure distribution through the test region, Fig. 3.27 presents the axial variation of the area-averaged total pressure coefficients as well as the axial variation of the standard deviation of the static pressure coefficients. These data showed equivalent total pressures at the upstream measurement plane for both model configurations. Then, at MP1, the total pressure values represented the losses accumulated along the flow diverter section and, as expected,

indicated significant total pressure losses through the vaned model segment. Throughout the remainder of the constant area blocked section, due to the expansion of the boundary layers (and wake regions in the vaned configuration), the area-averaged total pressures declined in a similar manner for both cases. Then, at the inlet of the aft guide vanes, the area-averaged total pressure for the vaned configuration was approximately 50 percent higher than that for the baseline configuration.

With respect to the distribution of the static pressures, the upstream flow for the baseline configuration was significantly less uniform than that in the vaned configuration, as indicated by the larger standard deviation. Then, within the constant-area blocked section, the baseline configuration continued to exhibit a higher level of non-uniformity within MP1, MP2, and MP3. Farther downstream, however, the flow in both configurations became very uniform as it approached the aft guide vanes, with a slight increase at MP6. This behavior was discussed previously, as the azimuthal variation in static pressures resulted in a slight reacceleration of the flow near the gearbox fairing.

In general, the trends observed in Fig. 3.27 present the total pressure losses in the flow throughout the forward bypass region as well as a measure of the overall uniformity of the flow. However, these area-averaged data do not present details of the increase in flow complexity through the constant-area blocked section. As seen from high-resolution pressure probe data within this region, the flow through the vaned model configuration exhibited localized wake and vorticity structures that were previously absent from the baseline flow. Based upon the planar flowfield measurements, these features were found to be relatively stationary, with some azimuthal motion as they propagated downstream. In general, however, they tended to expand as they traveled downstream, causing a larger portion of the flow annulus to be affected at the inlet of the aft guide vanes. Conversely, for the baseline configuration, the flow within the downstream measurement planes was extremely uniform, with smaller boundary-layer profiles than observed in the vaned configuration and only minor in-plane flow direction characteristics.

Shown in Fig. 3.28 is a comparison of the Mach number profiles for both the baseline and vaned model configurations. By utilizing a combination of static and total pressure distributions, these data clearly indicate the effect of the guide vanes on the flow speed within the test section. As discussed previously, the vanes affect the behavior of the

flow at each of the seven measurement planes. At the upstream measurement plane, the equivalent scales demonstrate the influence of the vanes on the uniformity of the incoming flow. Rather than an azimuthal distribution of Mach numbers in the baseline configuration, where the flow was slower ahead of the gearbox fairing, the vanes distributed the upstream effect of the blockage evenly around the flow annulus. Then, downstream of the guide vanes, the azimuthal variation in core flow Mach numbers remained fairly consistent between the two models. However, because boundary layers developed along the guide vanes, wake regions were located directly aft of the vanes, where the local Mach numbers were significantly reduced and flow complexity was greatly increased.

In order to further quantify the influence of the guide vanes on the bypass performance, a basic mass flow rate analysis was used to evaluate the effect of the total pressure losses within the test region. Using an observation from the centrifugal blower sizing analysis conducted in Appendix A, total pressure losses through the test section were found to be directly proportional to the freestream dynamic pressure measured at MP0. Therefore, assuming Reynolds number and Mach number effects on pressure loss were negligible for a small range in tunnel operating speeds, the total pressure values presented in Table 3.3 and Fig. 3.28 would remain consistent for each model configuration, regardless of the tunnel flow speed. With this assumption, a relationship was found between freestream dynamic pressures for both model configurations in order to match area-averaged total pressure losses at the inlet of the aft guide vanes. As a result, a 33-percent reduction in freestream dynamic pressure was required for the vaned model configuration to negate the 50-percent increase in total pressure losses. Using this change in dynamic pressure as a first-order indication of mass flow through the bypass region, the vaned configuration would require a mass flow rate reduction of approximately 18.5 percent to match total pressure losses through the baseline configuration. However, one of the motivations of adding guide vanes to the bypass flow was to increase mass flow through the overall engine system. Therefore, further analysis is required on a model that incorporates all aspects of the engine geometry, since the guide vanes could have a system-wide impact, influencing other portions of the flow.

3.5 Experimental and Computational Comparison

Since one of the goals of the current study was to examine the cumulative effects of the guide vanes on the entire bypass geometry, comparisons were drawn between the flow exiting the forward guide vanes and the experimental and computational studies performed simultaneously on the aft vane geometry. Due to the setup of the current study, MP6 was positioned to correspond with the inlet plane of the true aft guide vanes. Therefore, the flow behavior within MP6 could be compared directly with the upstream conditions in the experimental and computational studies conducted by Hortensius and Jain. Presented in Fig. 3.29 are the Mach number distributions formulated immediately upstream of the true aft guide vane geometry.[22,23] Note the change in scales due to differing speed capabilities between the experimental facilities and the computational simulation. Comparing these plots with similar data from Fig. 3.8 and Fig. 3.20, results from the aft geometry studies indicated higher flow speeds near the top center (0-degree) location of the flow region and lower speeds adjacent to the gearbox fairing. Data from the aft vane studies indicated that this azimuthal speed distribution was a product of flow separation and choking within the downstream channels nearest to the gearbox. This limited the mass flow through the most highly-curved channels while allowing more mass flow through the topmost channels. In order to mimic this behavior in the upstream portion of the experiment, a modification would be required to the downstream geometry in order to match the azimuthal distribution of mass flow through the test region.

In the two studies of the aft bypass geometry, neither case incorporated the upstream geometry (as indicated by the lack of vane wake structures) and the computational model was used to simply validate the experimental wind tunnel setup. Therefore, additional computational results were developed by Jain that studied the flow region around and through entire engine/nacelle geometry. This model simulated the intended cruise conditions of the supersonic aircraft and included boundary conditions to simulate the engine core flow in addition to the outer bypass flow.[23] Shown in Fig. 3.30 are data extracted from results simulated by Jain and are examples of the in-plane velocity vectors at axial stations corresponding to MP2 and MP5. In general, the behavior of the flow within the simulated MP2 exhibited some similarities with the experimental data in

the current study, including the presence of the vane wake structures as well as swirling regions throughout the cross-section. Unfortunately, because this simulation included the full engine geometry, a high-resolution grid was not used within the bypass region and only large flow features could be clearly identified.

For the full engine simulation at MP5, the flow began to behave very differently than that in the current experimental study. As seen from Fig. 3.30b, the in-plane velocity vectors were being directed toward the top center location of the flow region, rather than toward the gearbox fairing as seen from the experimental data. This was an additional indication that the flow into the aft guide vanes was less restricted near the topmost channels, with mass flow being restricted within the highly-curved channels nearest to the gearbox fairing. Again, achieving similar behavior in the current experimental setup would require a modification to the current model design in order to mimic the azimuthal mass flow distribution through the aft guide vanes.

Chapter 4

Summary, Conclusions, and Recommendations

4.1 Summary

To reduce the impact of the sonic boom signature produced by a supersonic business jet, Gulfstream Aerospace Corporation has developed an engine inlet design that tailors the position of the engine bow shock to terminate within the cowl lip of the external nacelle. Designed to improve engine efficiencies, the overall concept introduces a secondary annular bypass flow external to the primary engine bypass flow. This nacelle bypass removes low-quality flow from the engine core flow and, therefore, reduces distortions at the fan inlet plane. Because the engine gearbox components create a 160-degree partial annular blockage within the bypass duct, flow guide vanes were incorporated into the geometry to reduce flow separation around the gearbox fairing and to reaccelerate the exhaust flow to match the supersonic freestream. Due to the complex geometry within the bypass region, the flow behavior was also expected to be complex and highly-three-dimensional. Therefore, this study examined the aerodynamic characteristics of the subsonic flow within the forward set of guide vanes and up to the inlet of the aft guide vanes. Experimental analysis was conducted in an axisymmetric wind tunnel in the Aerodynamics Research Lab, a wind tunnel facility located at the University of Illinois at Urbana-Champaign.

In order to evaluate the effects of the guide vanes on the overall bypass flow, experiments were conducted on two separate models: one without forward guide vanes (the baseline model configuration) and one with integrated guide vanes (the vaned model configuration.) The wind tunnel and model were designed at a 16.2-percent scale, creating a flow annulus with inner and outer diameters of 8.102 inches and 11.1 inches,

respectively. To reach the design speed of the bypass flow, a centrifugal blower was sized and selected to replace an existing axial fan that was unable to provide the pressure recovery needed through the wind tunnel facility.

Due to the design of the rotating, cylindrical test section, pressure data were collected at several axial locations within the bypass flow region with high levels of azimuthal and radial resolution. With this capability, full planar profiles of pressure data were gathered throughout the test section in order to characterize the flow upstream and downstream of the forward guide vanes. In addition to static pressure measurements along the outer wall of the test section, a total pressure probe and a five-hole multi-directional probe were traversed through the flow region in order to examine pressure loss characteristics as well as flow angularity within the test section. Combinations of these pressure measurements allowed the formulation of Mach number and flow direction profiles and, more specifically, detailed examination of the flow within boundary layers, shear layers, and wake regions created by the guide vanes. In addition to pressure data, surface oil-flow visualization was also completed on both model configurations to further examine the complexity of the flowfield.

4.2 Conclusions

Based upon data collected throughout the current study, several conclusions could be made regarding the flow behavior within the forward portion of the bypass nacelle design, for both the baseline (unvaned) and vaned model configurations.

A. Baseline Configuration
    1. At the upstream measurement plane, total pressure losses were negligible within the core flow regions of the annulus. Boundary layers were evident along the inner and outer walls, with slightly thicker boundary-layer profiles present on the outer wall.
    2. At the upstream measurement plane, the static pressure distribution around the circumference of the test section resulted in core Mach numbers ranging from 0.24 to 0.31 and an area-averaged Mach number of 0.27. Here, the upstream influence of the gearbox blockage was evident, causing the flow along the

lower portion of the model to be slower than the flow along the upper portion of the model.

3. Within the blocked portion of the bypass region, total pressure losses remained negligible within the core flow regions. Boundary layers continued to grow along the inner and outer walls, and boundary-layer regions also developed along the walls of the gearbox component.
4. Using a static pressure map of the constant-area blocked section, Mach number profiles indicated azimuthal variations in core flow speed immediately aft of the flow diverter section, with speed uniformity developing toward the aft guide vanes. Throughout this region, the area-averaged Mach numbers remained consistent at 0.61.
5. Five-hole probe measurements within the forward portion of the constant-area blocked section indicated the core flow moving toward the top center (0-degree) location of the flow region. This trend remained consistent throughout the downstream measurement planes, with an exception near the centerbody/gearbox region, where the flow began to move downward toward the gearbox fairing as it approached the aft guide vanes.
6. Oil-flow visualization along the centerbody surface indicated flow moving toward the gearbox fairing throughout the entire blocked region. Using CFD results for comparison, an abrupt change in azimuthal flow direction was observed at the edge of the inner wall boundary layer, suggesting the presence of a flattened vortex along the centerbody surface. A similar, but less intense, feature was expected along the outer wall of the test section, as indicated by oil-flow visualization along the gearbox wall.

B. Vaned Configuration

1. At the upstream measurement plane, the total pressure behaved similarly to that in the baseline configuration, with significant losses only present within the inner and outer boundary-layer profiles.
2. At the upstream measurement plane, the static pressures were consistent around the circumference of the test section. Here, the resulting core Mach numbers ranged from 0.27 to 0.28, with an area-averaged Mach number of

0.27. In this model configuration, the upstream influence of the gearbox blockage was not apparent, indicating that the guide vanes had evenly distributed the effect of the gearbox blockage across the entire flow annulus.

3. Immediately downstream of the guide vanes, total pressure losses were not only significant within the inner and outer boundary-layer regions, but also directly aft of the guide vanes themselves. These wake regions tended to expand and shift as they traveled downstream toward the aft guide vanes.
4. Along the gearbox wall, small regions of total pressure deficit developed at the gearbox/centerbody junction, expanded to the entire width of the annulus, and occupied approximately 10 percent of the flow annulus at the inlet of the aft guide vanes.
5. At the inlet plane of the aft guide vanes, the area-averaged total pressure loss for the vaned model configuration was approximately 50 percent higher than that for the baseline configuration. Therefore, the vaned configuration would experience an 18.5-percent decrease in mass flow to match total pressure losses of the baseline model at the entrance to the aft guide vanes.
6. Using outer wall static pressures measured in the constant-area blocked section, Mach number profiles indicated strong variations in core flow speed immediately aft of the flow diverter section, with the speed distribution becoming more uniform toward the aft guide vanes. Within the vane wake regions, flow speeds are much lower than adjacent core flow regions, as expected from the total pressure profiles. Throughout this region, the area-averaged Mach numbers remained consistent at 0.60, a slight reduction from the baseline configuration due to the presence of the vane wake features.
7. Using five-hole probe measurements within the constant-area blocked section, the core flow regions behaved similarly to the flow in the baseline configuration, with strong upward motion immediately aft of the forward guide vanes, and transitioning toward the gearbox in the measurement planes near the aft vanes.
8. Five-hole probe measurements also depicted swirling motion within the vane wake regions and along the gearbox wall. These apparent vortices continued

to propagate through the constant-area blocked section toward the aft guide vanes.

9. Surface oil-flow visualization performed within the vane channels illustrated highly-complex flow along the centerbody and vane surfaces, with separated/vortical flow occurring on the suction side of the vanes.
10. Oil patterns aft of the guide vanes and along the centerbody surface indicated flow moving toward the gearbox fairing throughout the entire blocked region, similar to the patterns observed on the baseline configuration. Immediately downstream of the vanes, however, irregularities in the oil streak patterns indicated highly-complex flow features within the vane wake regions.

While the integration of forward guide vanes created a uniform Mach number distribution at the bypass inlet plane, the improved upstream flow uniformity came at a cost of increased total pressure losses, decreased speed uniformity, and an overall increase in complexity and flow distortion at the inlet plane of the aft guide vanes. Both model configurations were tested with equivalent mass flow rates; therefore, a simple loss analysis indicated that a significant reduction in mass flow through the vaned model would be required to match total pressure losses through the forward portion of the bypass region. Further analysis is necessary to determine acceptable levels of loss through the bypass duct in order to properly condition the upstream and downstream flowfields for optimal engine/nacelle performance. If, for instance, the 50 percent increase in total pressure loss through the vaned bypass geometry resulted in an enhanced boom signature and improved engine performance and thrust capabilities, the increased complexity of the bypass flow would most likely be tolerated in the overall engine design. Therefore, a fully-coupled analysis of the engine system is required to assess the total effect of the forward guide vanes within the secondary bypass flow.

4.3 Recommendations

Based on the observations and conclusions identified through this study, several recommendations can be made to improve further experiments in terms of the overall wind

tunnel facility, data acquisition capabilities, and simulating flow conditions of the true bypass geometry.

1. Although a new centrifugal blower was selected to provide higher flow speeds through the test section, the goal of Mach 0.70 flow within the aft portions of the constant-area blocked section was unattainable. Since the blower was limited by its total pressure recovery capabilities, steps could be taken to lower the total pressure losses aft of the boat-tail fairing. Suggestions for accomplishing this are dependent on increasing the fairing half-angle from the current 10-degree geometry, which could be supplemented by providing vortex generators, tangential blowing, or other separation-control methods along the fairing wall.
2. In order to match the downstream mass flow distribution of the current geometry with that produced in the computational and experimental studies of the aft guide vanes, variable-density screens could be added downstream of MP6 to simulate appropriate back pressures throughout the flow region.
3. While the current study examined the flow upstream and downstream of the forward guide vanes, it may be helpful to investigate specific flow features within the vane channels, such as the vortical structures that developed along the suction side of the vanes. In order to accomplish this, additional probe access ports would be required in the fixed upstream test section at specific locations within the channels. A more effective solution may be to implement a method allowing rotation of the outer test section wall around the entire model, while also maintaining a robust seal between the vaned channels.
4. Due to the chosen data acquisition methods, the current study primarily collected time-averaged pressure data. Because the wake regions are expected to be highly unsteady, time-resolved measurements would provide a better understanding of the flow unsteadiness as the flow exits the guide vanes. This could be accomplished by using particle image velocimetry, hot-wire probes, and/or probes integrated with miniature pressure transducers.
5. The current study was limited to collecting pressure data on a point-by-point basis. Therefore, a more thorough investigation of the vane wake behavior might incorporate an azimuthal array of probes to assess both the spatial and temporal

behavior of a given wake structure. Difficulties may arise due to the annular shape of the test region; however, this could be resolved by fabricating a probe mounting device with the capability to alter the curvature of the array for varying radial locations.

6. In order to provide a comprehensive investigation of the forward guide vanes in the high-flow bypass design, a fully-coupled experimental analysis should be completed with the aft guide vane geometry as well as the inlet and engine core flow regions. In the meantime, by using localized experimental results to validate CFD simulations of a decoupled system, a thorough computational analysis should provide a suitable simulation of the full engine system.

References

[1] Anderson, J. D., Jr., *Modern Compressible Flow: with Historical Perspective*, McGraw-Hill, Boston, 2003.

[2] Plotkin, K. J. and Maglieri, D. J., "Sonic Boom Research: History and Future," 33rd *AIAA Fluid Dynamics Conference and Exhibit*, AIAA-2003-3575, Orlando, FL, 2003.

[3] Seebass, A. R., (ed.), *Sonic Boom Research (Proceedings)*, NASA-SP-147, Washington, D.C., 1967.

[4] Sparrow, V. and Coulouvrat, F., "Status of Sonic Boom Knowledge: December 2006," *Committee on Aviation Environmental Protection Seventh Meeting*, CAEP/7-17/18, Orlando, FL, 2007.

[5] Seebass, R., "Sonic Boom Minimization," *RTO AVT Course on Fluid Dynamics Research on Supersonic Aircraft*, Rhode-Saint-Genese, Belgium, 1998.

[6] Pawlowski, J. W., Graham, D. H., and Boccadoro, C. H., "Origins and Overview of the Shaped Sonic Boom Demonstration Program," 43rd *AIAA Aerospace Sciences Meeting and Exhibit*, AIAA-2005-5, Reno, NV, 2005.

[7] Henne, P. A., "A Gulfstream Perspective on the DARPA QSP Program and Future Civil Supersonic Initiatives," *FAA Civil Supersonic Aircraft Workshop*, Arlington, VA, 2003.

[8] Simmons, F., III and Freund, D., "Quiet Spike™: The Design and Validation of an Extendable Nose Boom Prototype," 48th *AIAA/ASME/ASCE/AHS/ASC Structures, Structural Dynamics, and Materials Conference*, AIAA-2007-1774, Honolulu, HI, 2007.

[9] Howe, D. C., Waithe, K. A., and Haering, E. A., Jr., "Quiet Spike™ Near Field Flight Test Pressure Measurements with Computational Fluid Dynamics Comparisons," *46th AIAA Aerospace Sciences Meeting and Exhibit*, AIAA-2008-128, Reno, NV, 2008.

[10] Conners, T. R., Gulfstream Aerospace Corporation, Savannah, GA, U.S. Patent Application for "Low Shock Strength Inlet," Application No. 12/000,066, filed 7 Dec. 2007.

[11] Conners, T. R., Gulfstream Aerospace Corporation, Savannah, GA, U.S. Patent Application for "Low Shock Strength Propulsion System," Application No. 12/257,982, filed 24 Oct. 2008.

[12] Kim, H. J., Kumano, T., Liou, M.-S., Povinelli, L. A., "Optimal Shape Design of Supersonic Bypass Inlet," 13th *AIAA/ISSMO Multidisciplinary Analysis Optimization Conference*, AIAA-2010-9171, Fort Worth, TX, 2010.

[13] Kim, H. J., Kumano, T., Liou, M.-S., Povinelli, L. A., "Flow Simulation of Supersonic Inlet with Bypass Annular Duct," *Journal of Propulsion and Power*, Vol. 27, No. 1, Jan.-Feb. 2011.

[14] Conners, T. R., Merret, J. M., Howe, D. C., Tacina, K. M., and Hirt, S. M., "Wind Tunnel Testing of an Axisymmetric Isentropic Relaxed External Compression Inlet at Mach 1.97 Design Speed," 43rd *AIAA/ASME/SAE/ASEE Joint Propulsion Conference and Exhibit*, AIAA-2007-5066, Cincinnati, OH, 2007.

[15] Conners, T. R. and Howe, D. C., "Supersonic Inlet Shaping for Dramatic Reductions in Drag and Sonic Boom Strength," 44*th AIAA Aerospace Sciences Meeting and Exhibit*, AIAA-2006-30, Reno, NV, 2006.

[16] Conners, T.R. and Wayman, T.R., "The Feasibility of High-Flow Nacelle Bypass for Low Sonic-Boom Propulsion System Design," *AIAA 29th Applied Aerodynamics Conference*, 2011.

[17] Yeong, Y. H., Chiles, I. M., Bragg, M. B., Elliott, G. S., Loth, E., and Conners, T. R., "Wind Tunnel Testing of a Nacelle Bypass Concept for a Quiet Supersonic Aircraft," *39th AIAA Fluid Dynamics Conference*, AIAA-2009-4207, San Antonio, TX, 2009.

[18] Yeong, Y. H., "Wind Tunnel Testing of a Nacelle Bypass Concept for a Quiet Supersonic Aircraft," M.S. Thesis, Dept. of Aerospace Engineering, University of Illinois at Urbana-Champaign, Urbana, IL, 2009.

[19] Chiles, I. M., Loth, E., Yeong, Y. H., Bragg, M. B., and Elliott, G. S., "Computations of Engine Bypass in a Wind Tunnel Configuration," *39th AIAA Fluid Dynamics Conference*, AIAA-2009-4208, San Antonio, TX, 2009.

[20] Chiles, I. M., "Simulations of a Bypass Flow Between an Engine and a Nacelle," M.S. Thesis, Dept. of Aerospace Engineering, University of Illinois at Urbana-Champaign, Urbana, IL, 2009.

[21] Chima, R. V., Conners, T. R., and Wayman, T. R., "Coupled Analysis of an Inlet and Fan for a Quiet Supersonic Jet," 48*th AIAA Aerospace Sciences Meeting and Exhibit*, AIAA-2010-479, Orlando, FL, 2010.

[22] Hortensius, R., Bragg, M. B., and Elliott, G. S., "An Experimental Investigation of the Flow Through the Aft Portion of a High-Flow Nacelle Bypass Concept," 50*th AIAA Aerospace Sciences Meeting*, Nashville, TN, 2012 (submitted for publication).

[23] Jain, N., Bodony, D. J., "Computational Assessment of Flow through a High-Flow Nacelle Bypass," 50*th AIAA Aerospace Sciences Meeting*, Nashville, TN, 2012 (submitted for publication).

[24] Jacobs, J. J., "Iced Airfoil Separation Bubble Measurements by Particle Image Velocimetry, Ph.D. Dissertation," Dept. of Aerospace Engineering, University of Illinois at Urbana-Champaign, Urbana, IL, 2007.

[25] Barlow, J. B., Rae, W. H., Jr., and Pope, A., *Low-Speed Wind Tunnel Testing*, 3rd ed., Wiley, New York, 1999.

[26] von Doenhoff, A. E. and Horton, E. A., "A Low-Speed Experimental Investigation of the Effect of a Sandpaper Type of Roughness on Boundary-Layer Transition," NACA-TR-1349, 1958.

[27] Chue, S. H., "Pressure Probes for Fluid Measurement," *Progress in Aerospace Sciences*, Vol. 16, No. 2, 1975.

[28] Bryer, D. W. and Pankhurst, R. C., *Pressure-Probe Methods for Determining Wind Speed and Flow Direction*, H.M.S.O., London, 1971.

[29] Danko, M., "High Speed Engine Nacelle Bypass," Project Report, Dept. of Aerospace Engineering, University of Illinois at Urbana-Champaign, Urbana, IL, 2009.

[30] Hewkin, J., "Design Optimization and Wind Tunnel Testing of an Annular Fairing with Vortex Generators," Project Report, Dept. of Aerospace Engineering, University of Illinois at Urbana-Champaign, Urbana, IL, 2010.

[31] Gonsalez, J. C. and Arrington, E. A., "Five-Hole Flow Angle Probe Calibration for the NASA Glenn Icing Research Tunnel," NASA-CR-1999-202330, Glenn Research Center, 1999.

[32] Fontaine, R., Bobbitt, B., Elliott, G. S., Austin, J. M., and Freund, J. B., "Design and Demonstration of a New Small-Scale Jet Noise Experiment," 50*th AIAA Aerospace Sciences Meeting*, Nashville, TN, 2012 (submitted for publication).

[33] Kline, S. J., and McClintock, F. A., "Describing Uncertainties in Single-Sample Experiments," *Mechanical Engineering*, 1953.

[34] Moffat, R. J., "Contributions to the Theory of Single-Sample Uncertainty Analysis," *Transactions of the ASME*, Vol. 104, 1982.

[35] Zilliac, G. G., "Modelling, Calibration, and Error Analysis of Seven-Hole Pressure Probes" *Experiments in Fluids*, Vol. 14, No. 1-2, 1993.

Figures

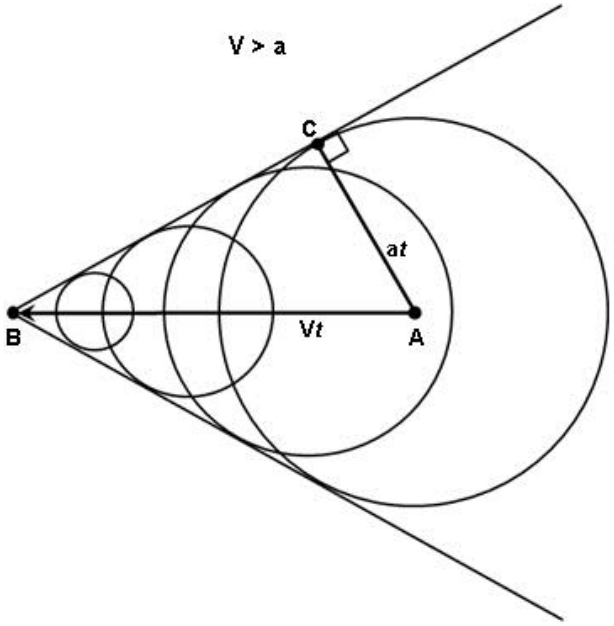

Fig. 1.1 Formation of a Mach cone.[1]

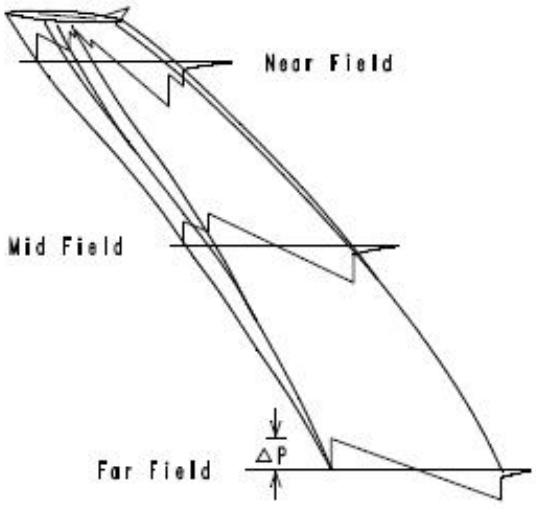

Fig. 1.2 Evolution of a characteristic N-wave boom signature.[2]

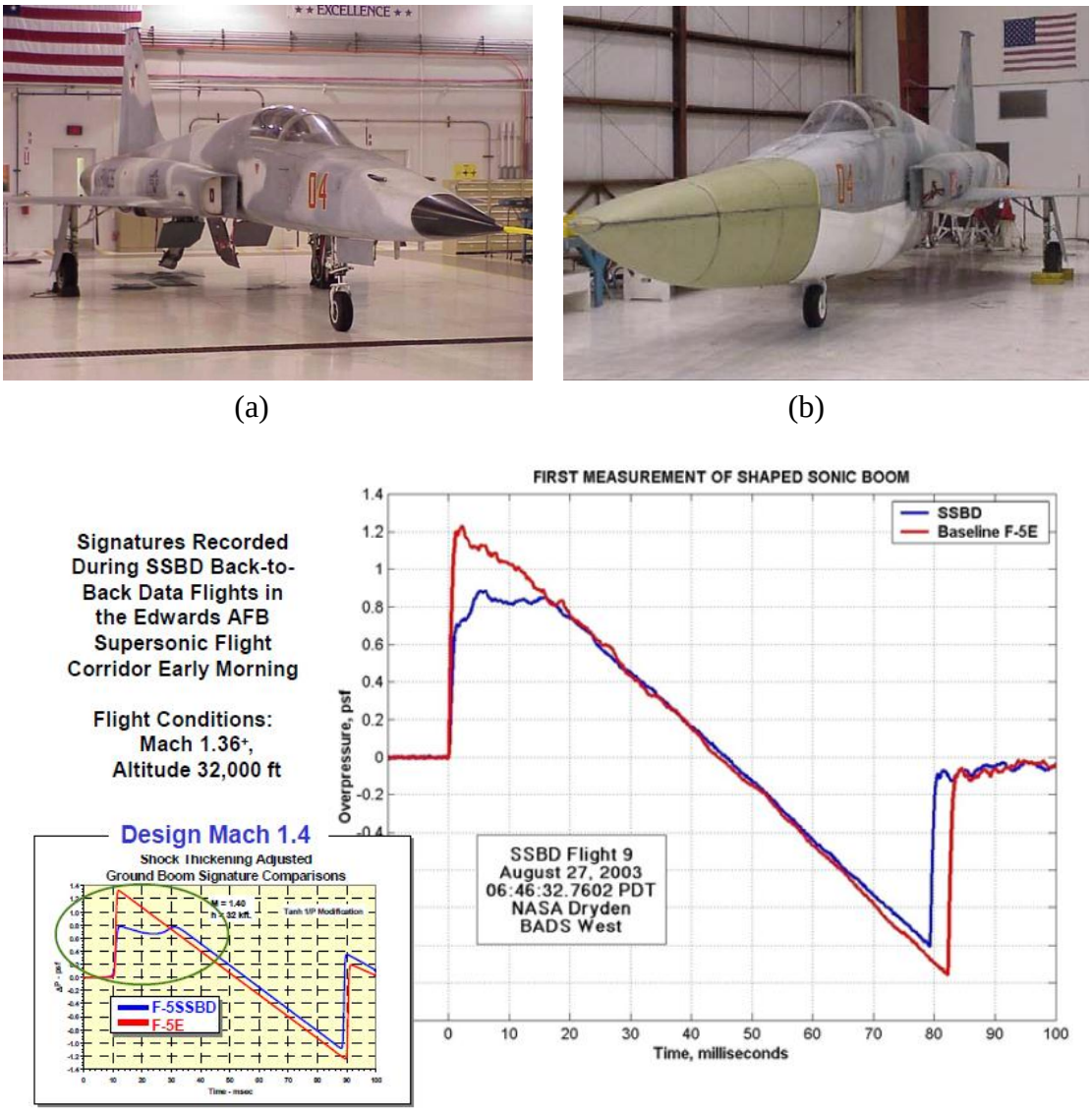

Fig. 1.3 (a) Unmodified F-5E, (b) modified SSBD, and (c) computational and experimental comparison of the two boom signatures.[6]

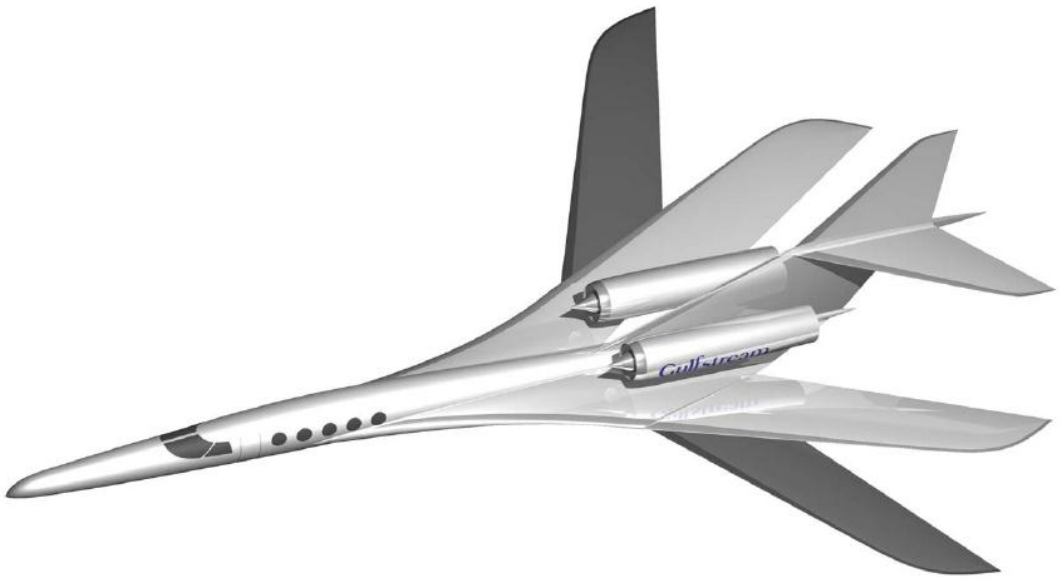

Fig. 1.4 Gulfstream quiet supersonic jet concept.[7]

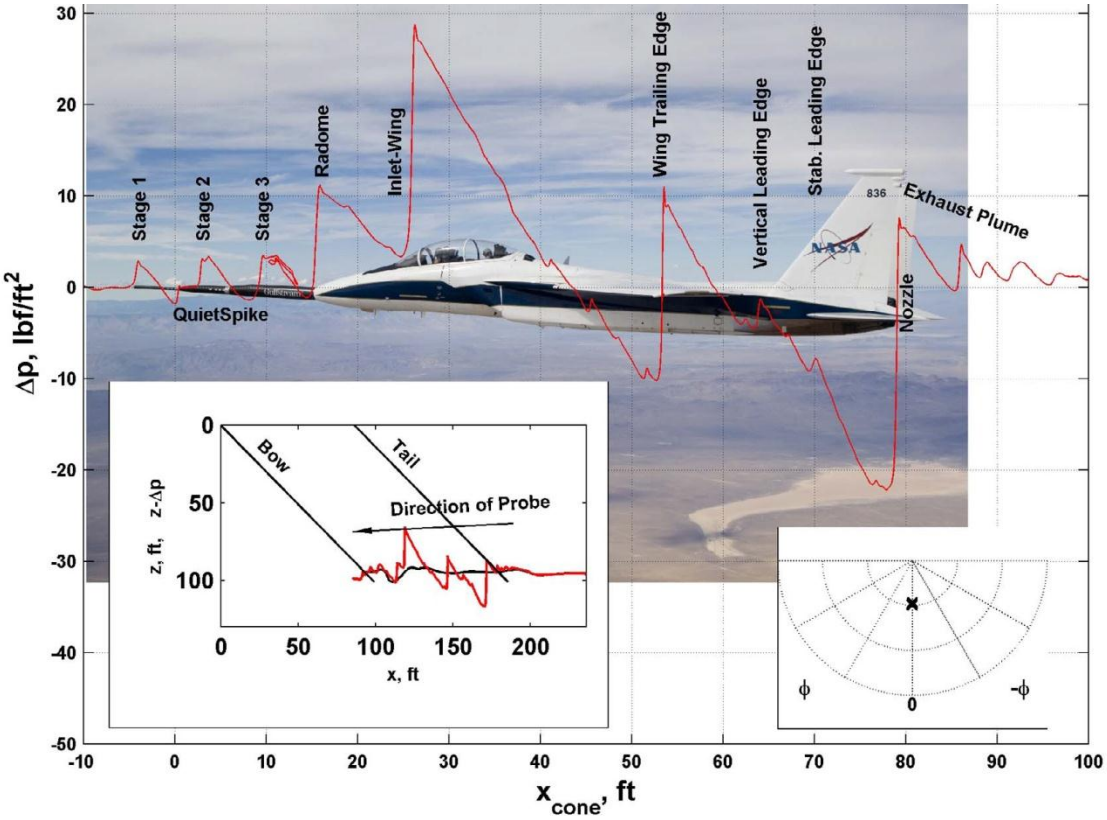

Fig. 1.5 Boom signature created by an F-5 aircraft with attached Quiet Spike™.[9]

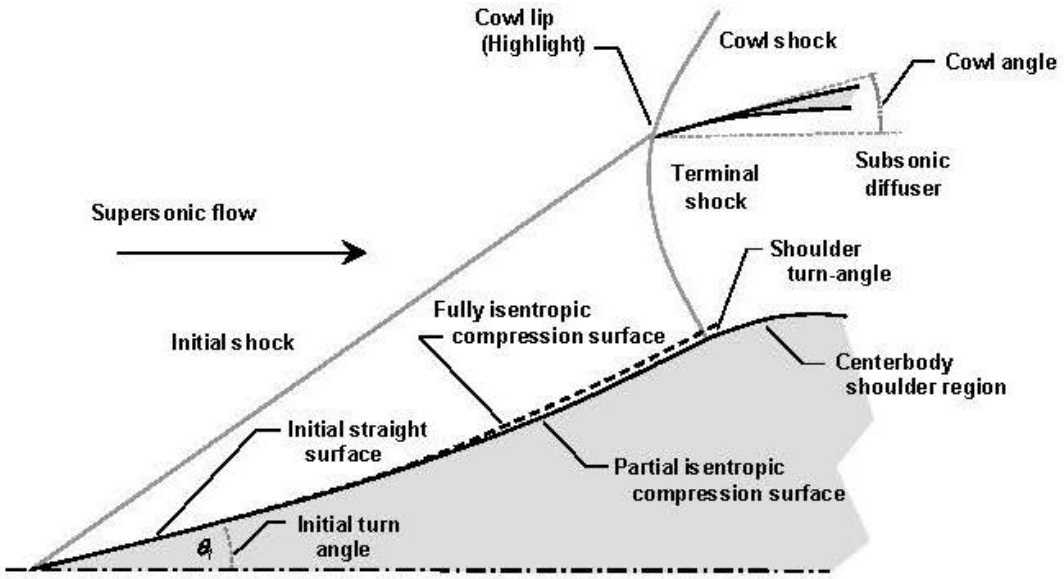

Fig. 1.6 Relaxed isentropic inlet design.[15]

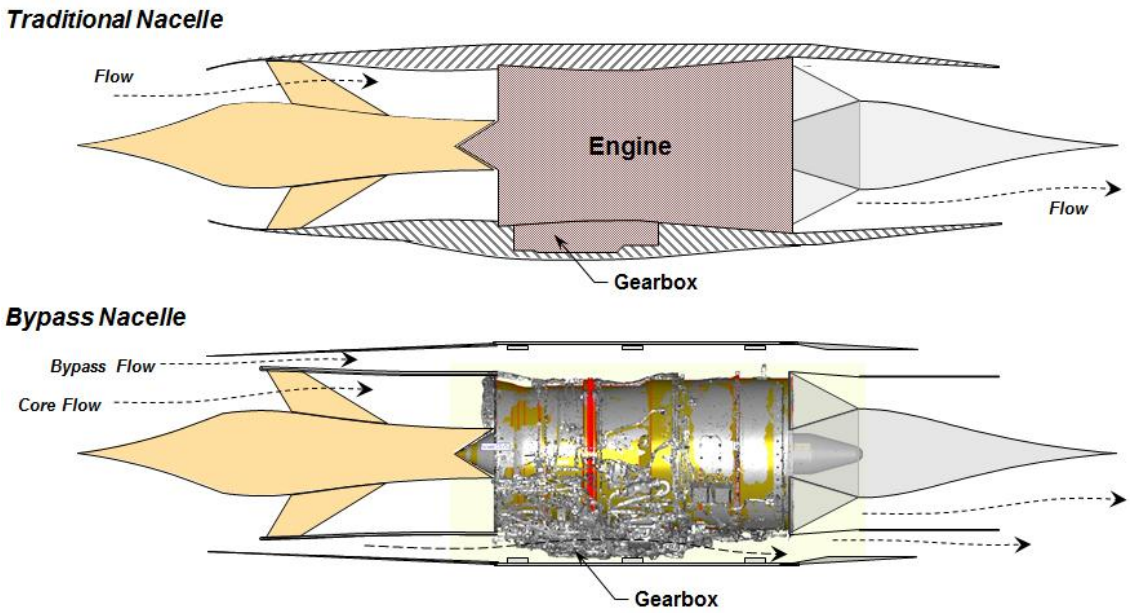

Fig. 1.7 Comparison of nacelle designs. (Courtesy of GAC)

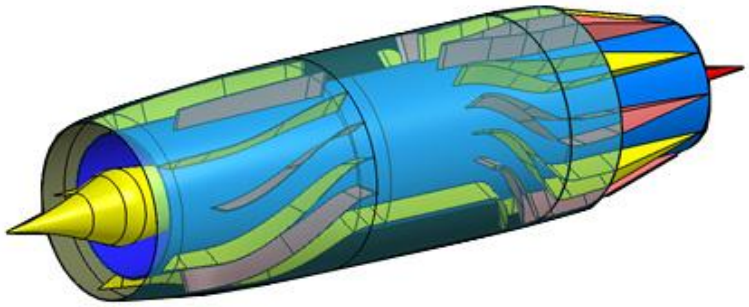

Fig. 1.8 CAD model of the vaned bypass design. (Courtesy of GAC)

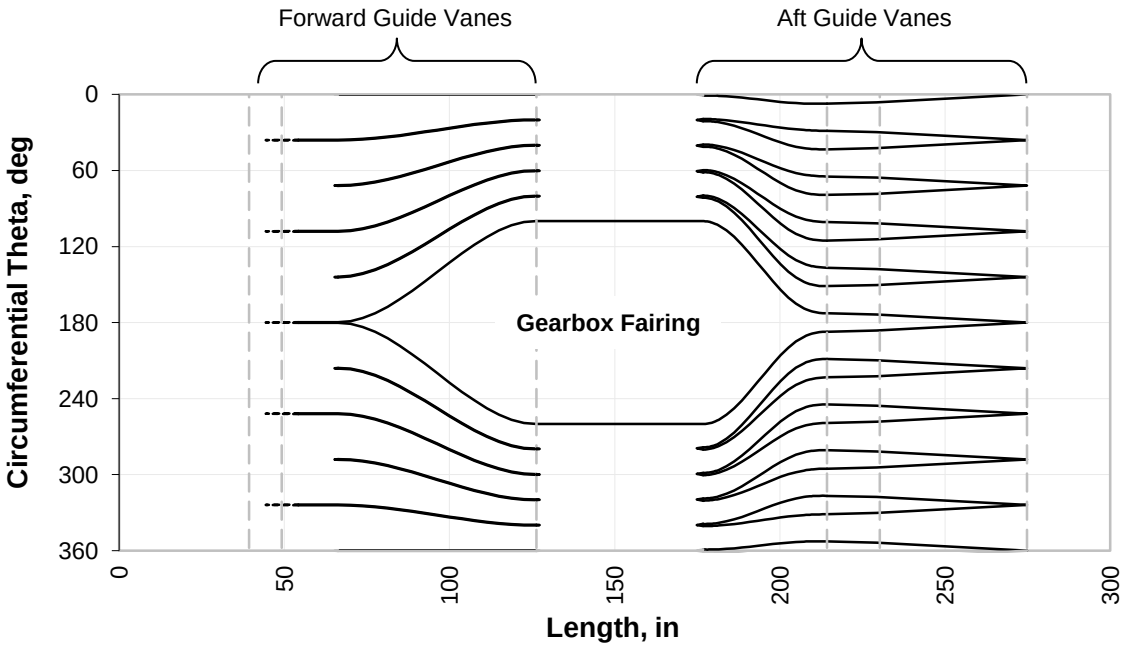

Fig. 1.9 Vane configuration within the annular bypass duct. (Courtesy of GAC)

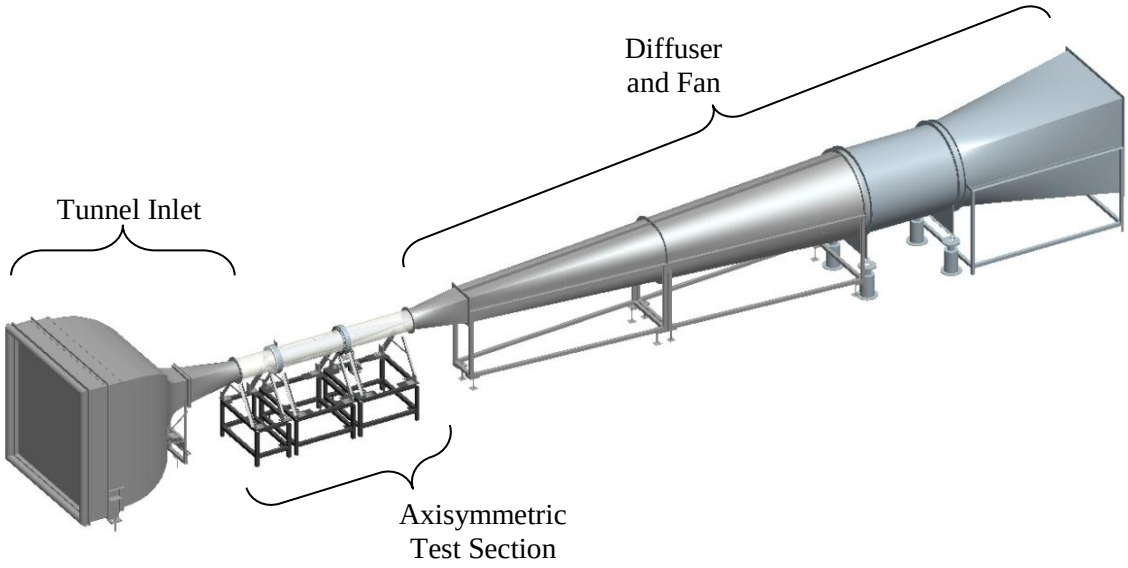

(a)

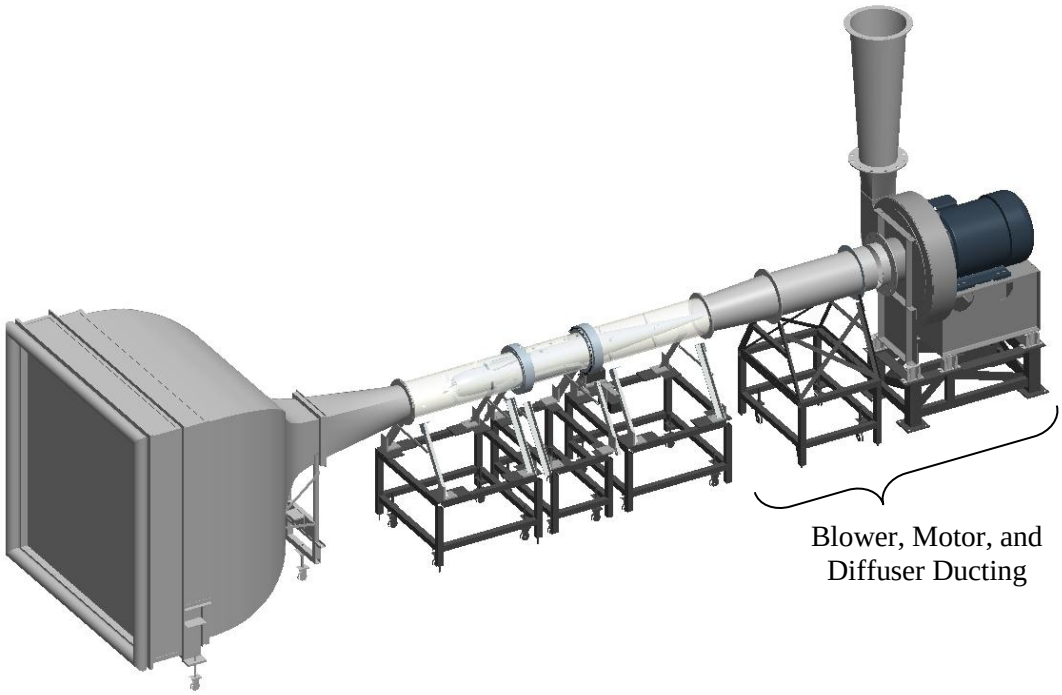

(b)

Fig. 2.1 Model of the wind tunnel facility in the (a) original and (b) modified configurations.

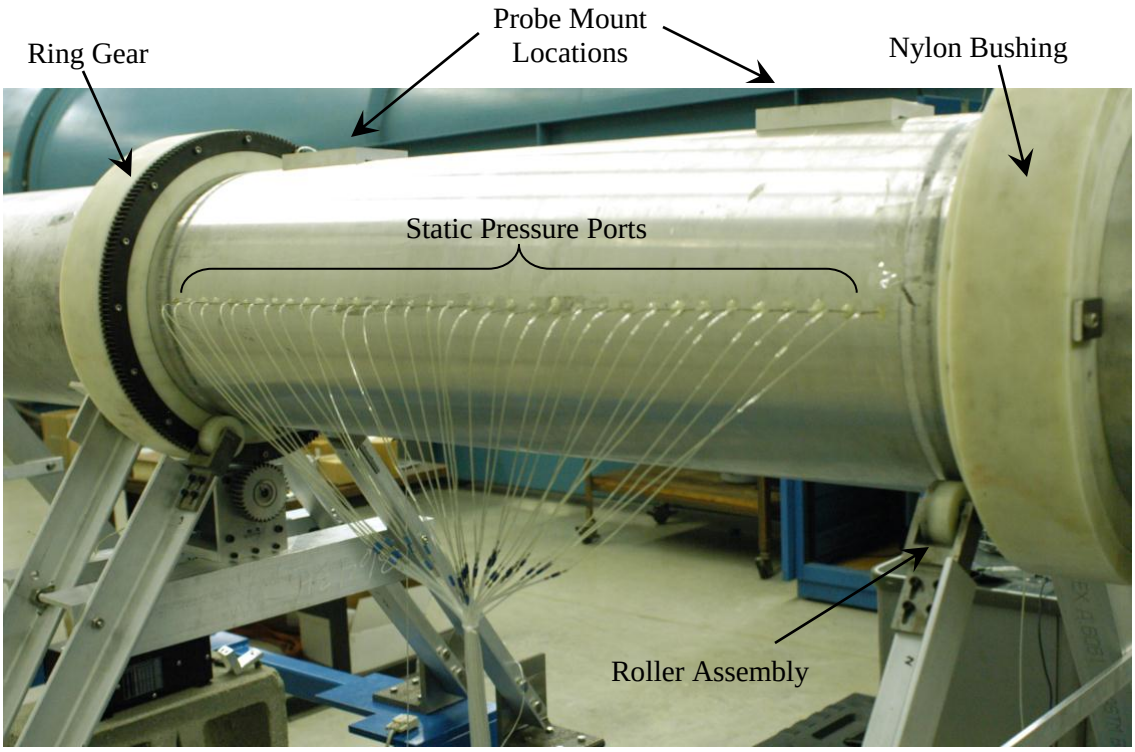

Fig. 2.2 Original test section configuration.

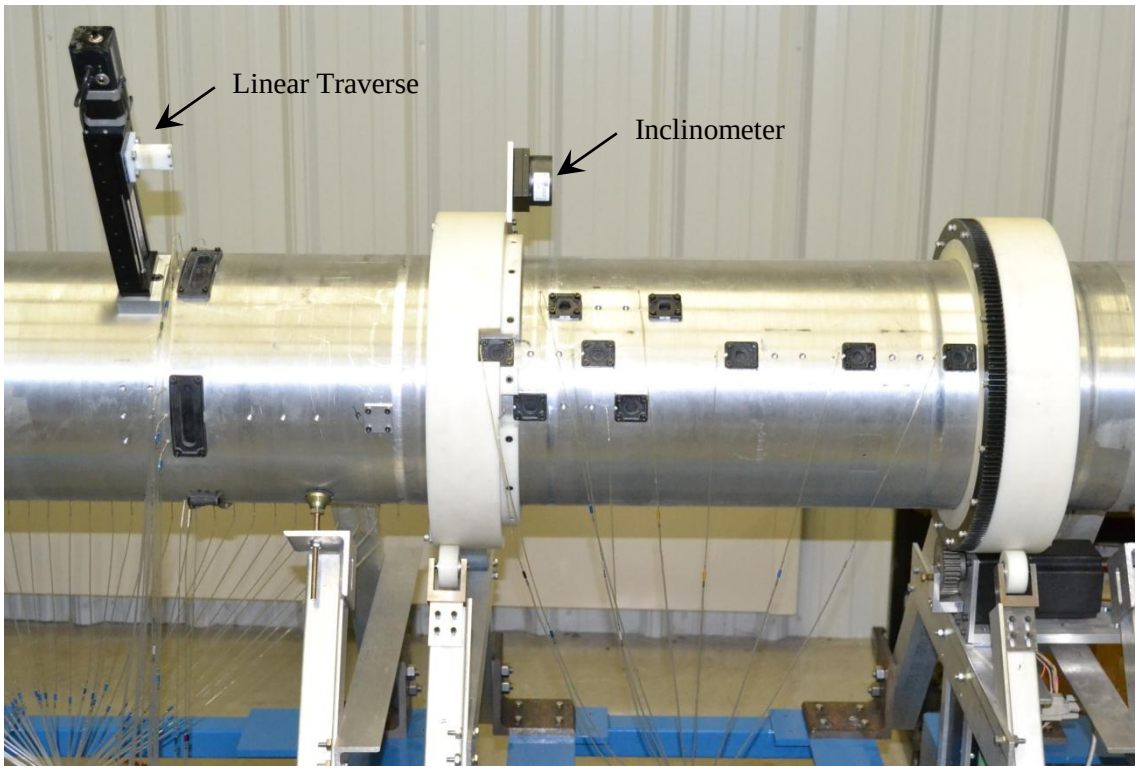

Fig. 2.3 Modified test section with additional measurement ports.

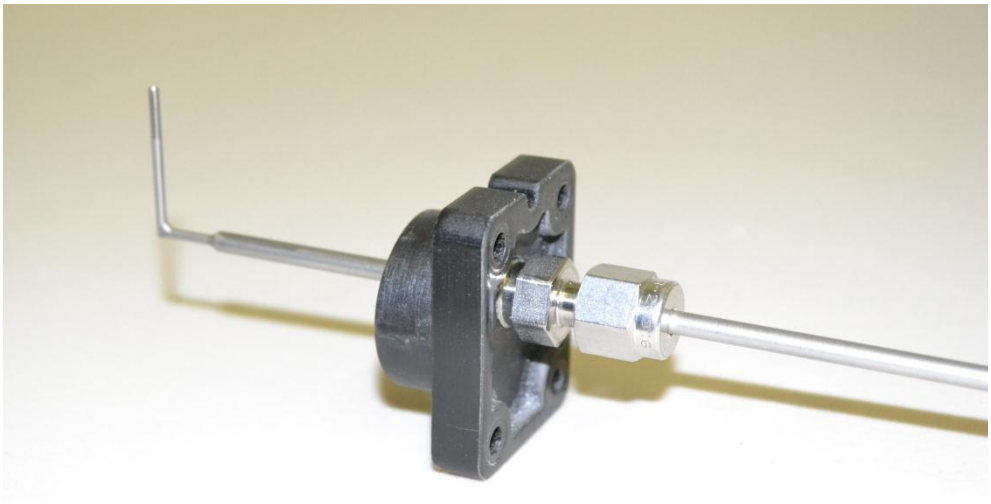

Fig. 2.4 Probe plug assembly with mounting chuck.

Fig. 2.5 Centrifugal blower with ducting and support frames.

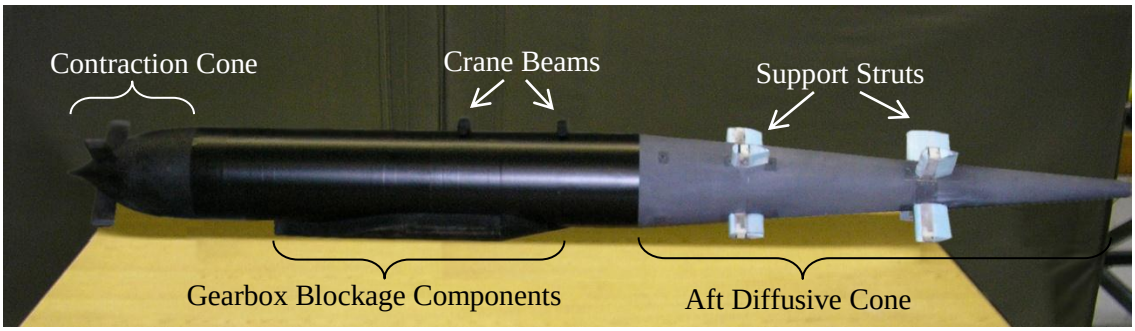

Fig. 2.6 Original model with 110-degree blockage.

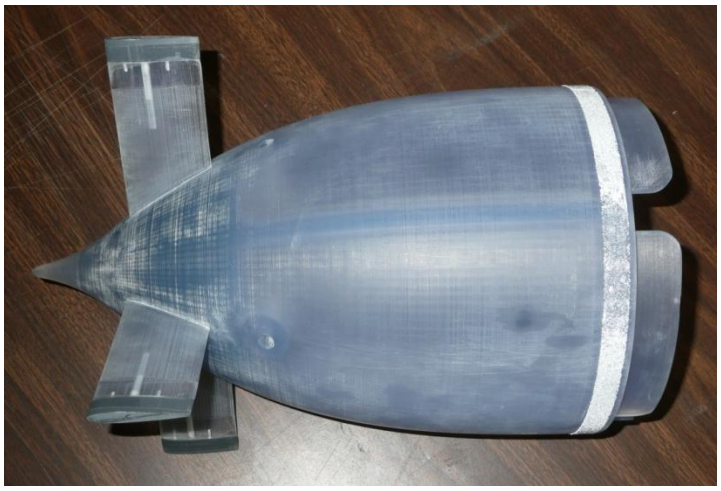

Fig. 2.7 Forward contraction cone with boundary-layer trip strip.

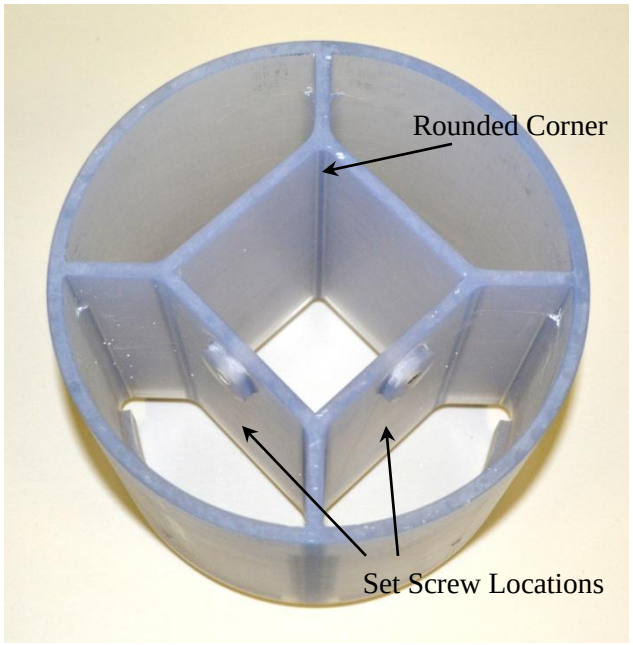

Fig. 2.8 Model center cavity design.

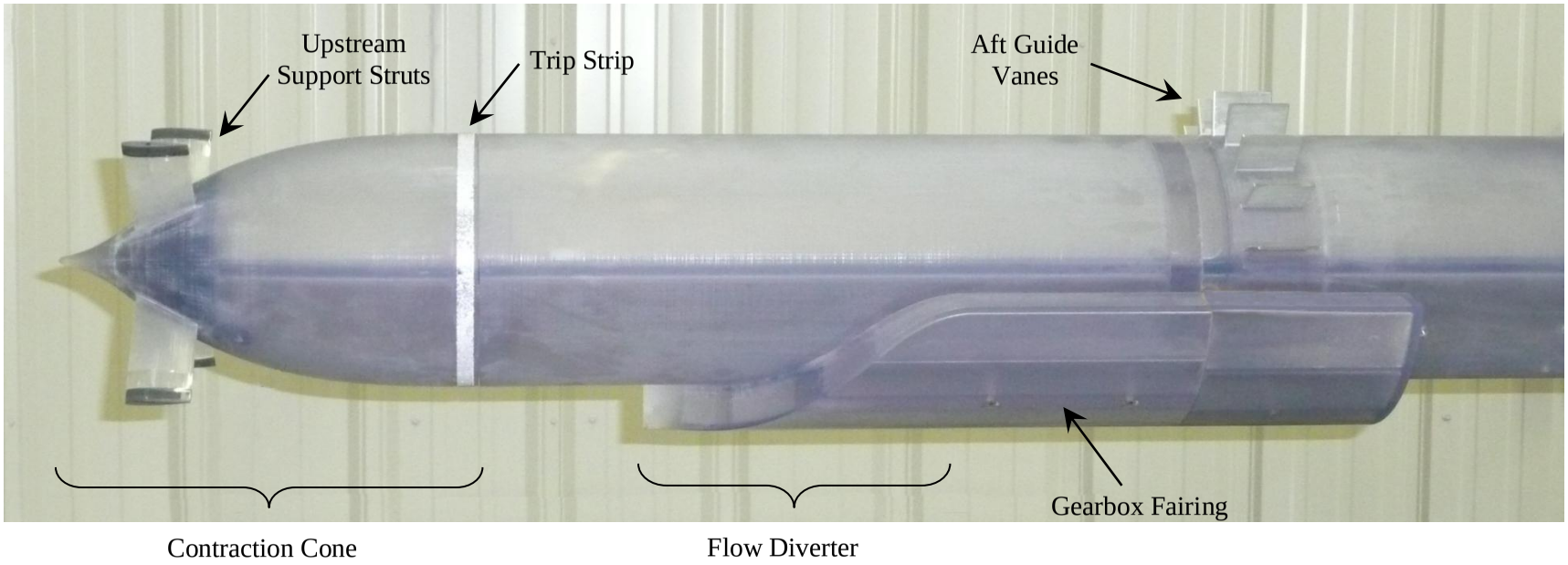

Fig. 2.9 Bypass model in the baseline flow configuration.

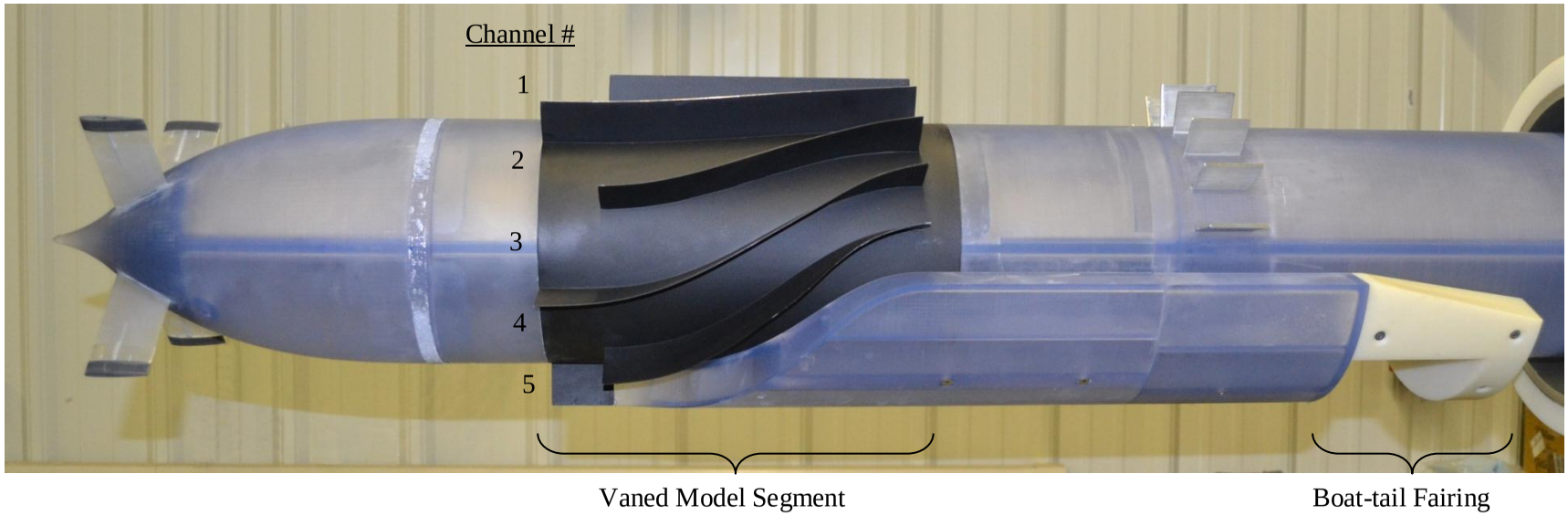

Fig. 2.10 Bypass model in the vaned flow configuration.

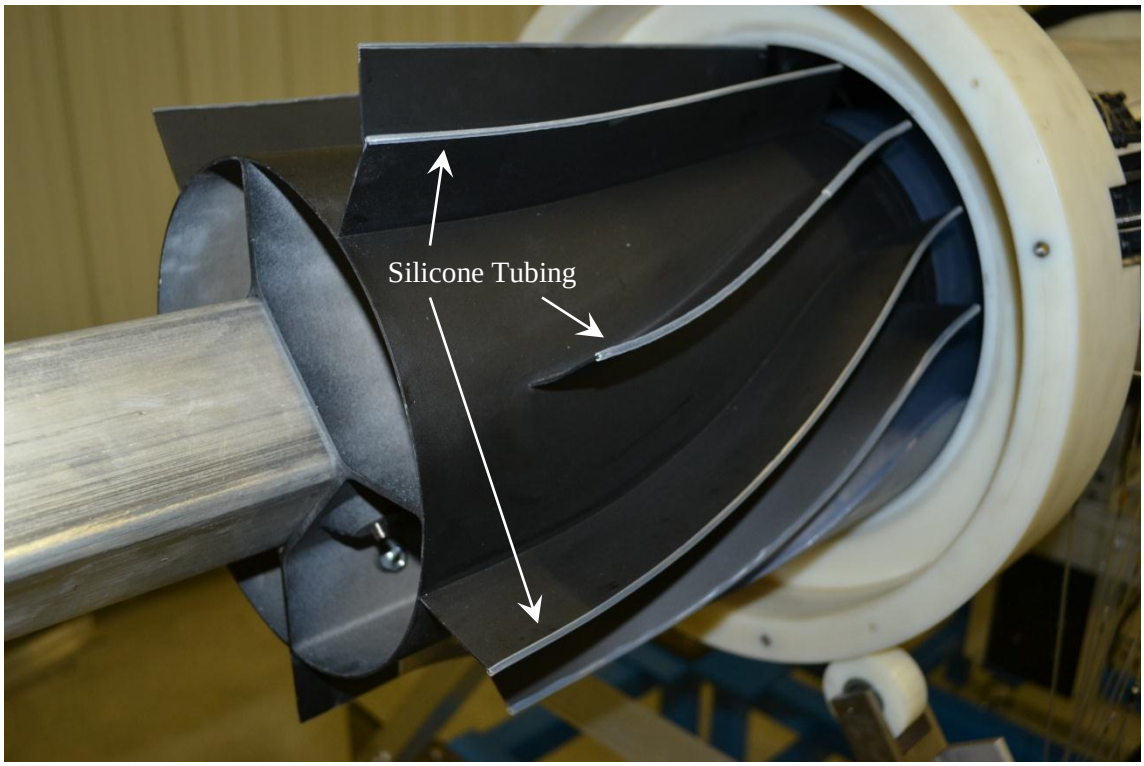

Fig. 2.11 Vaned model section with tubing affixed to the vane tips for sealing purposes.

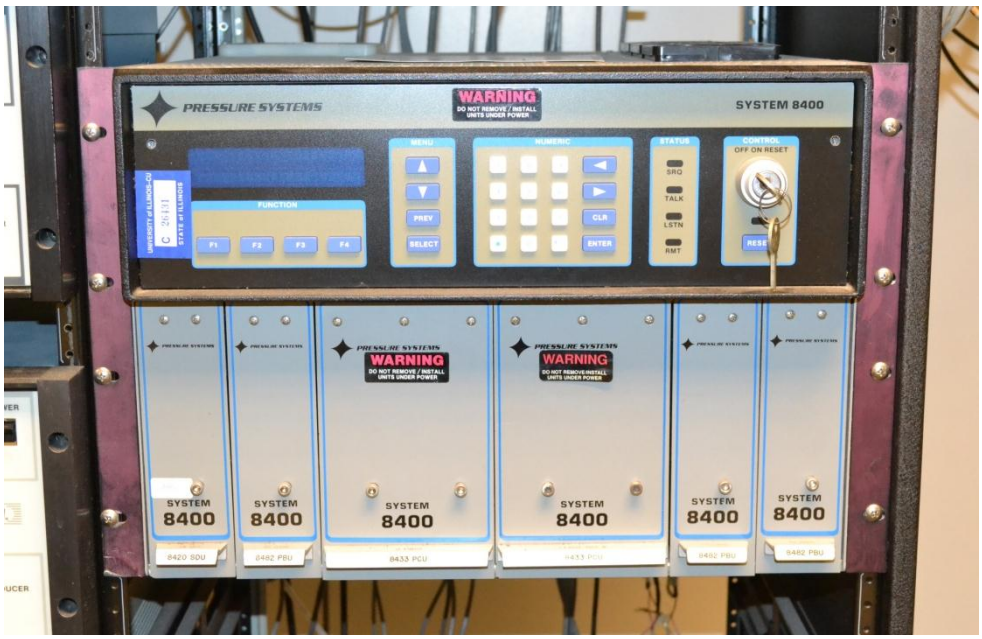

Fig. 2.12 System 8400 pressure acquisition system.

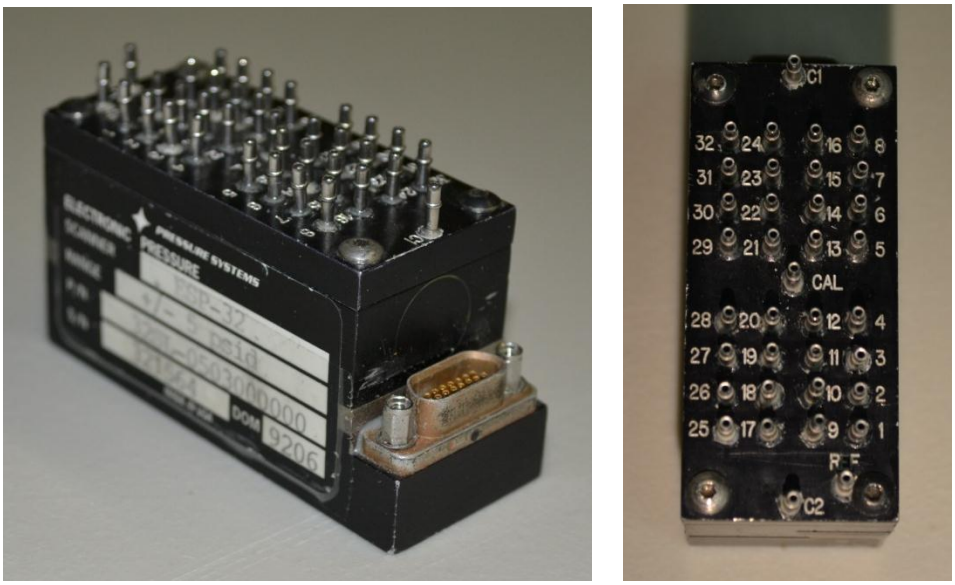

Fig. 2.13 Five-psid ESP module and pressure port layout.

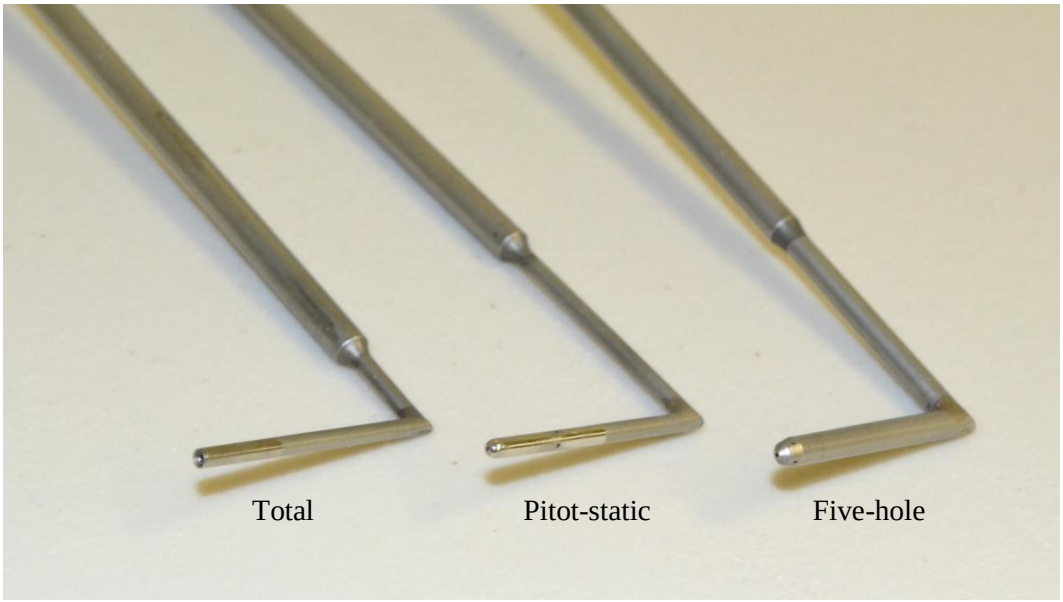

Fig. 2.14 Pressure probes used for data acquisition.

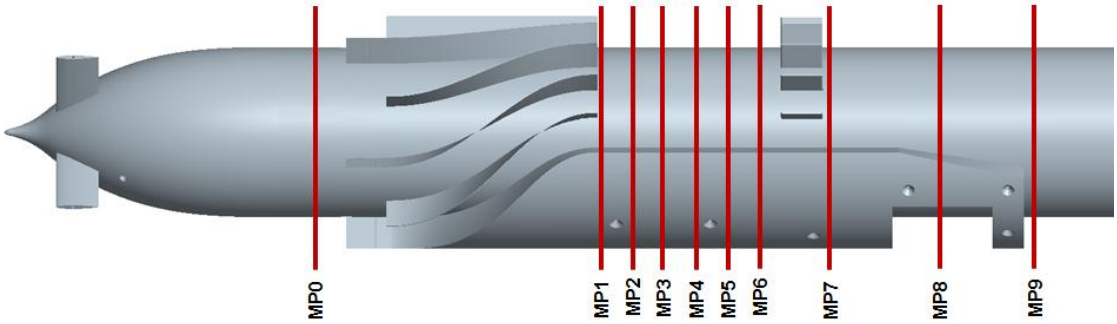

Fig. 2.15 Model of the vaned configuration depicting pressure measurement locations.

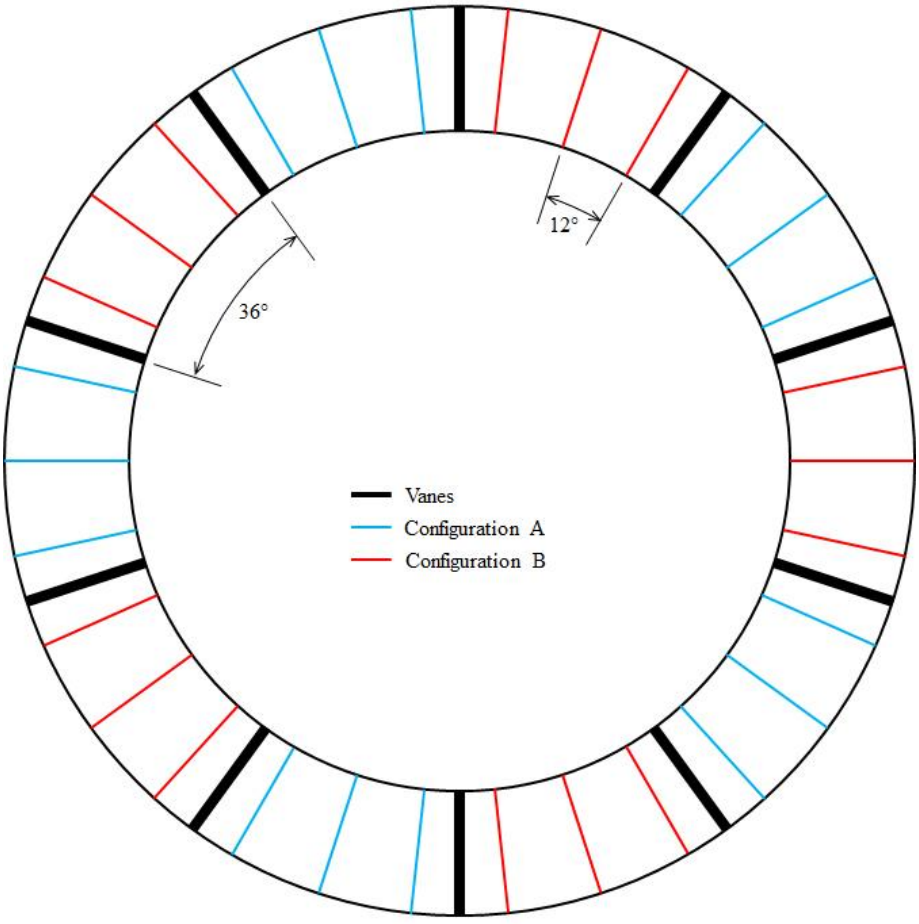

Fig. 2.16 Probe measurement locations at the upstream measurement plane.

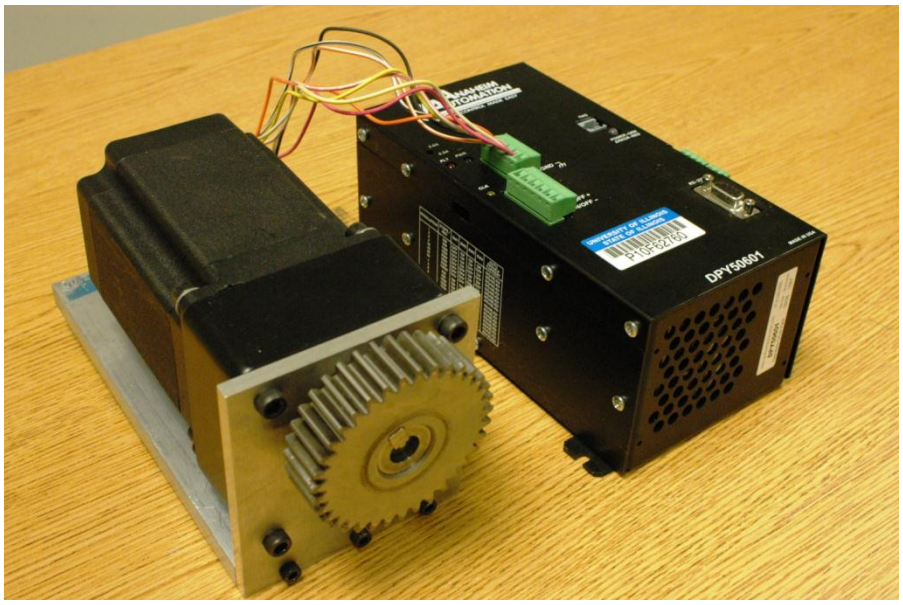

Fig. 2.17 Stepper motor and controller.

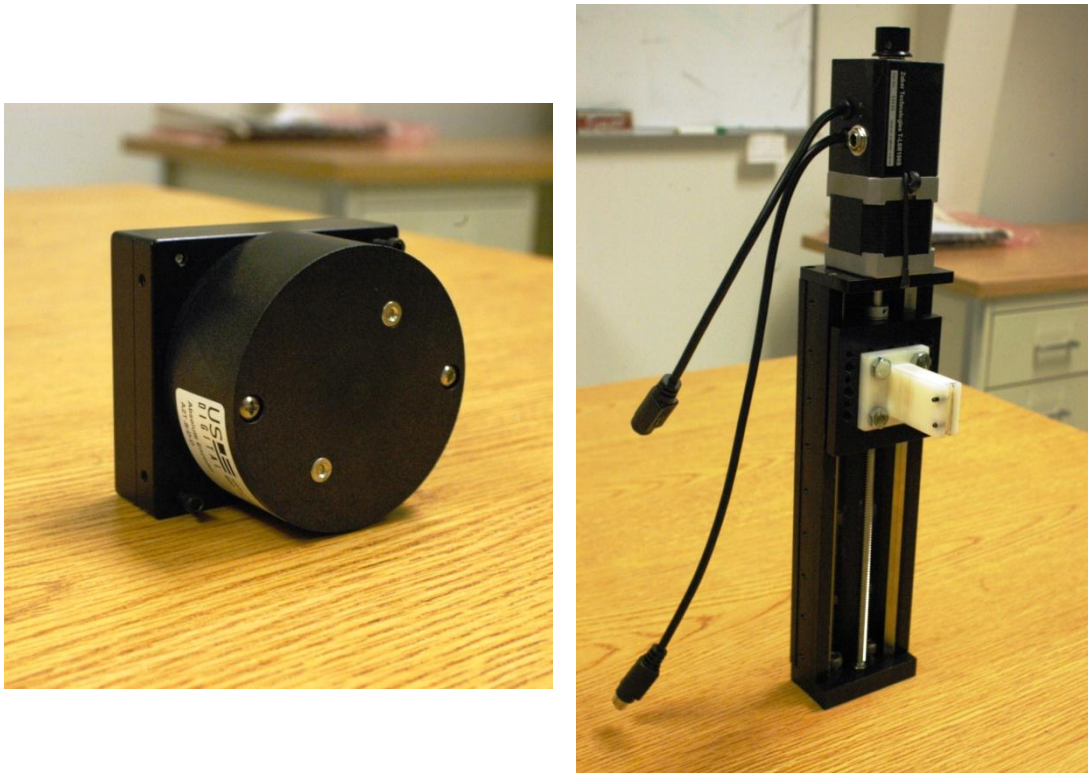

(a) (b)

Fig. 2.18 (a) Digital inclinometer and (b) linear traverse with probe mount.

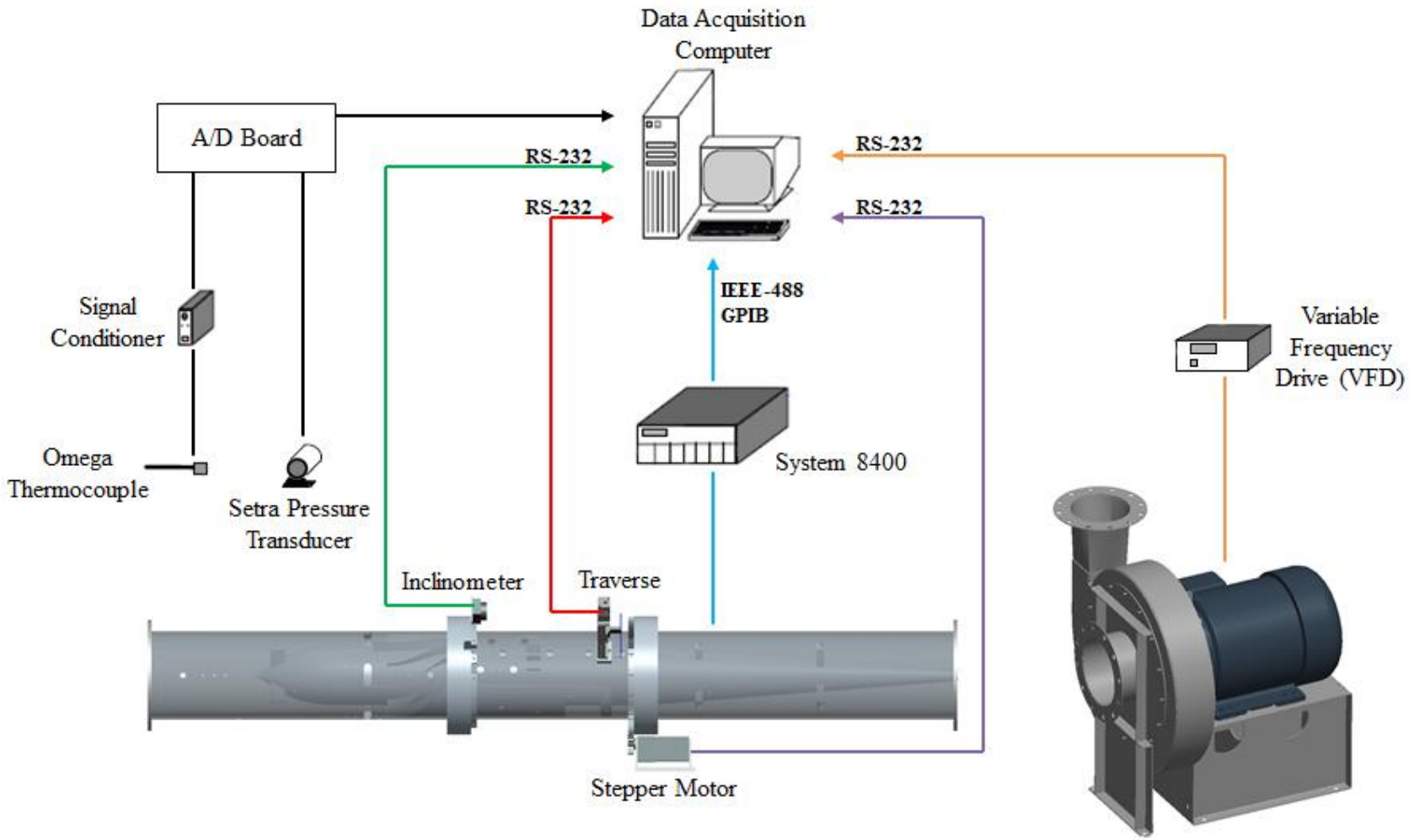

Fig. 2.19 Schematic of the computer-controlled devices.

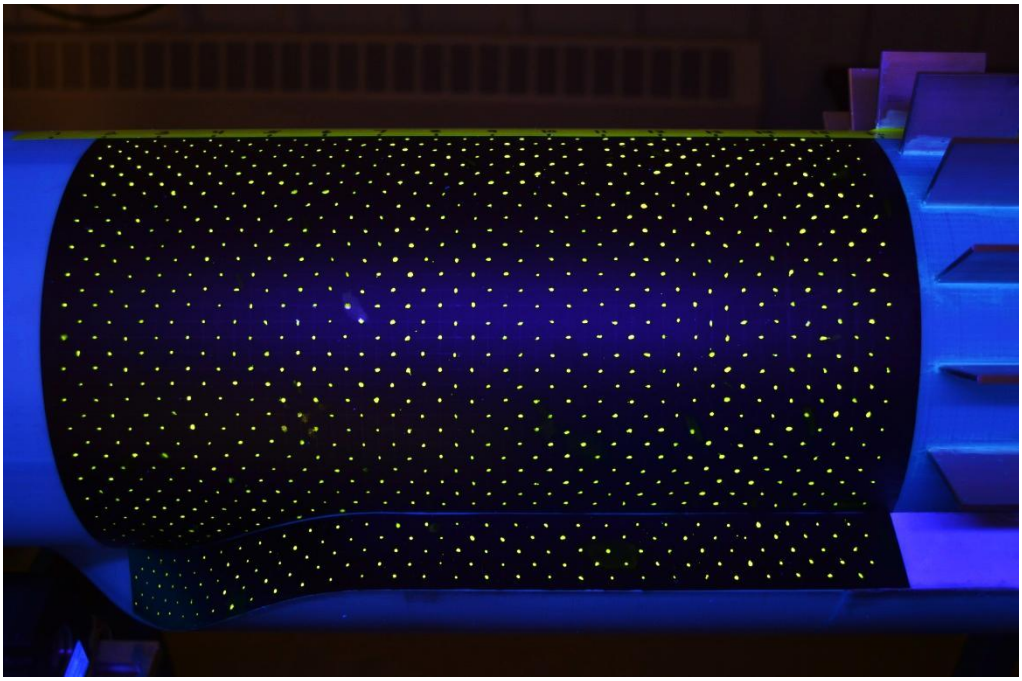

Fig. 2.20 Example of dot spacing applied to the baseline model for oil-flow visualization.

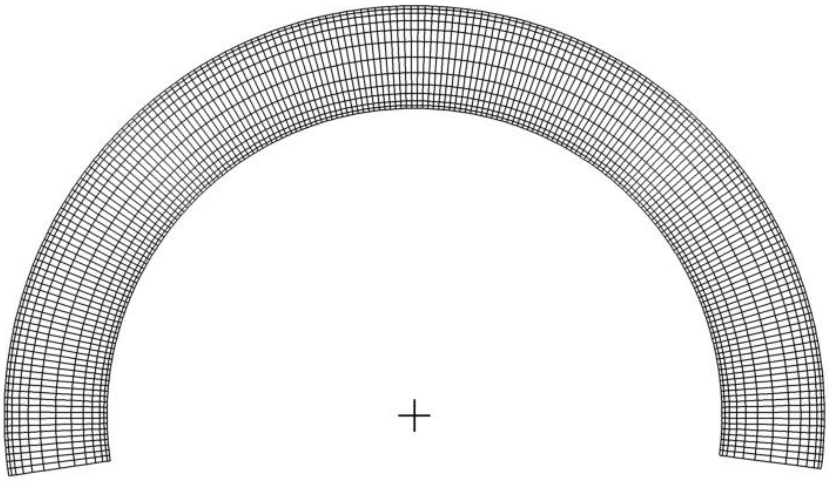

Fig. 2.21 Example of probe measurement spacing for the vaned model configuration.

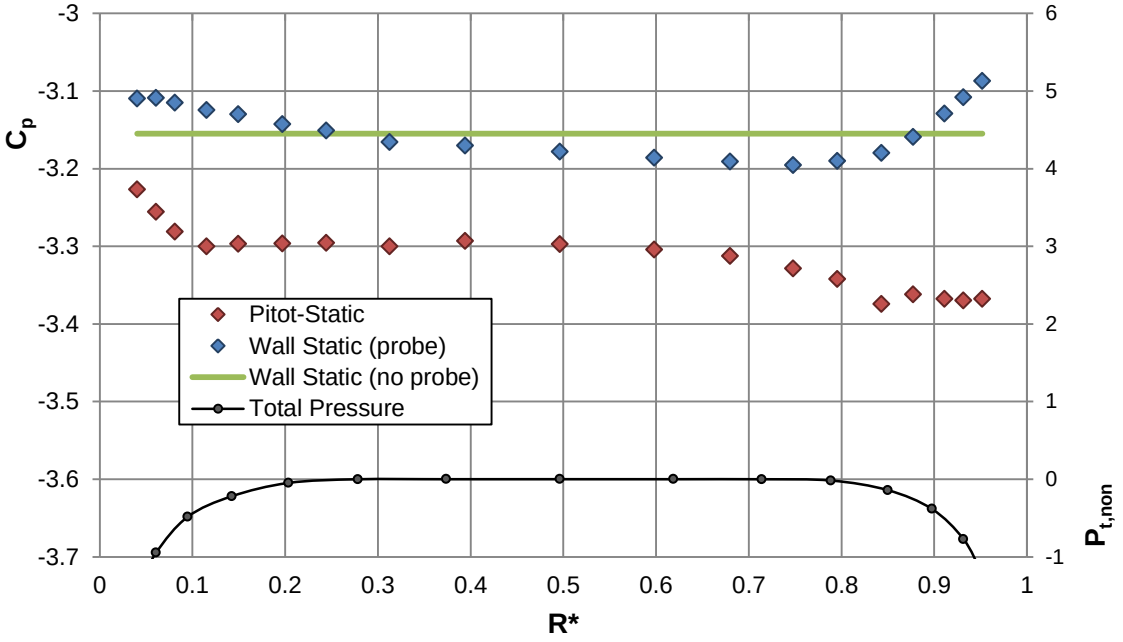

Fig. 2.22 Comparison of static pressure measurement methods.

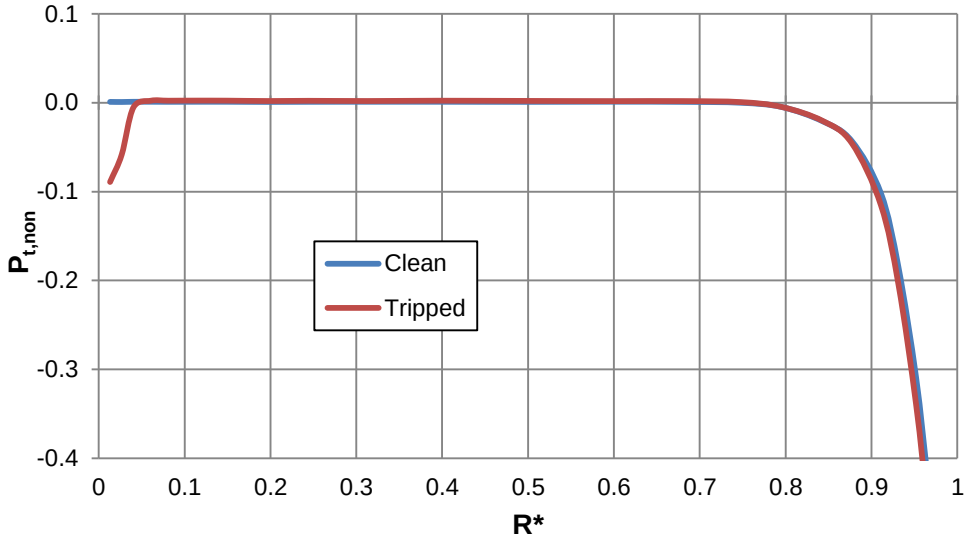

Fig. 3.1 Comparison of upstream total pressure surveys with and without a trip strip.

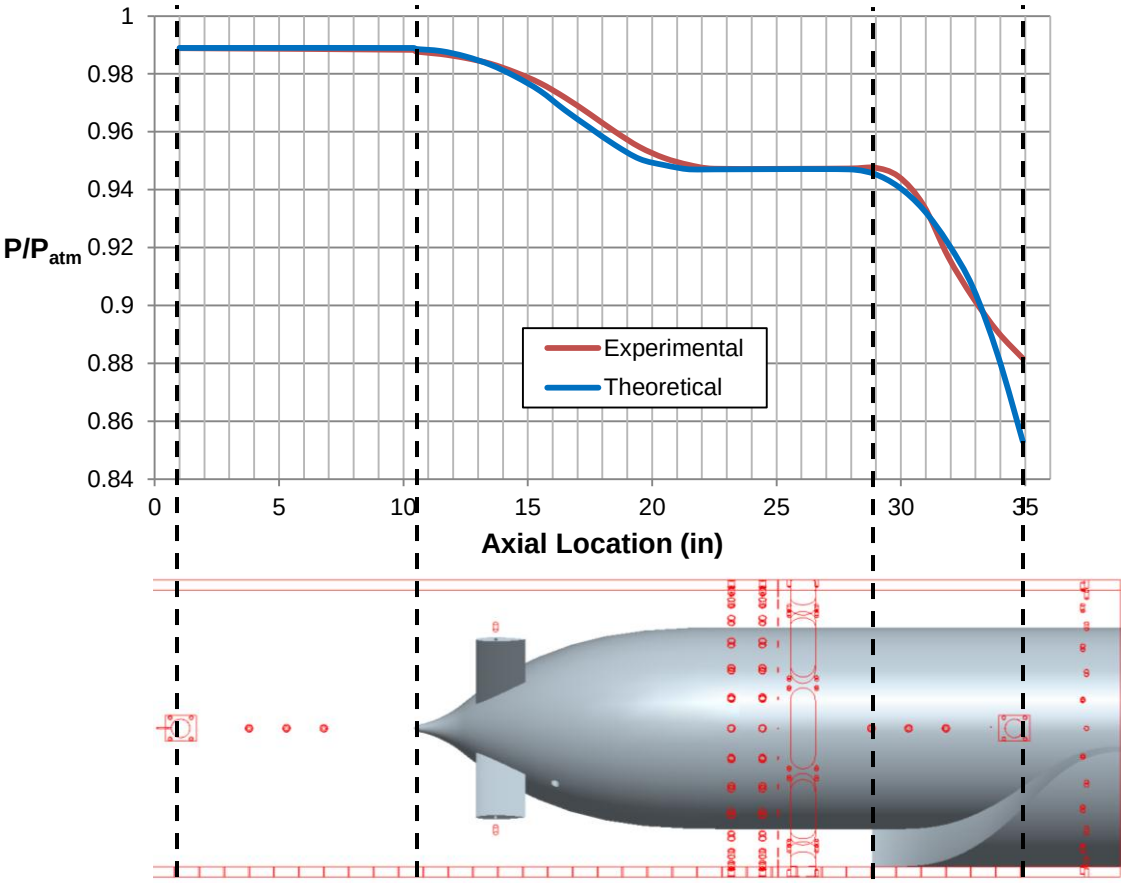

Fig. 3.2 Measured upstream pressure ratios compared with those calculated through isentropic relations.

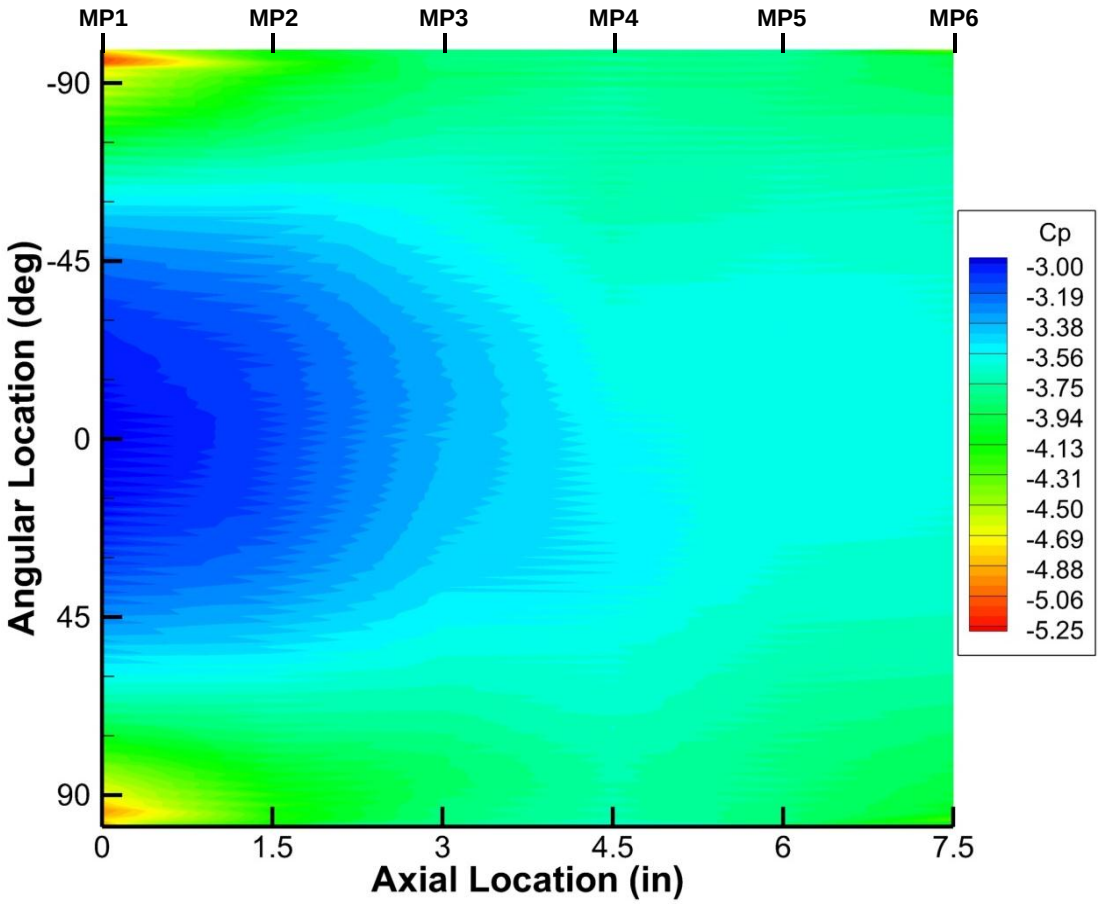

Fig. 3.3 Static pressure distribution in the constant-area blocked section for the baseline model configuration.

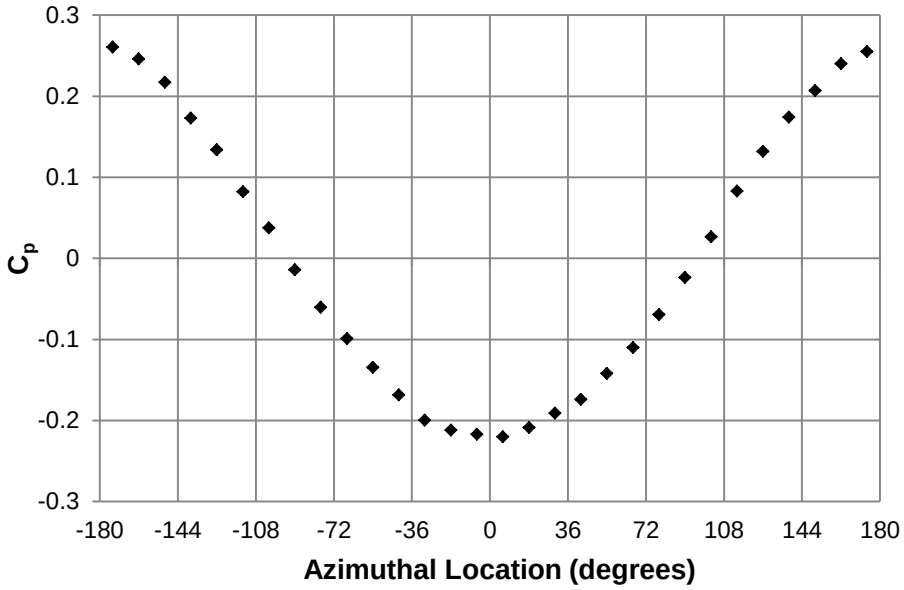

Fig. 3.4 Azimuthal static pressure distribution at MP0 for the baseline model configuration.

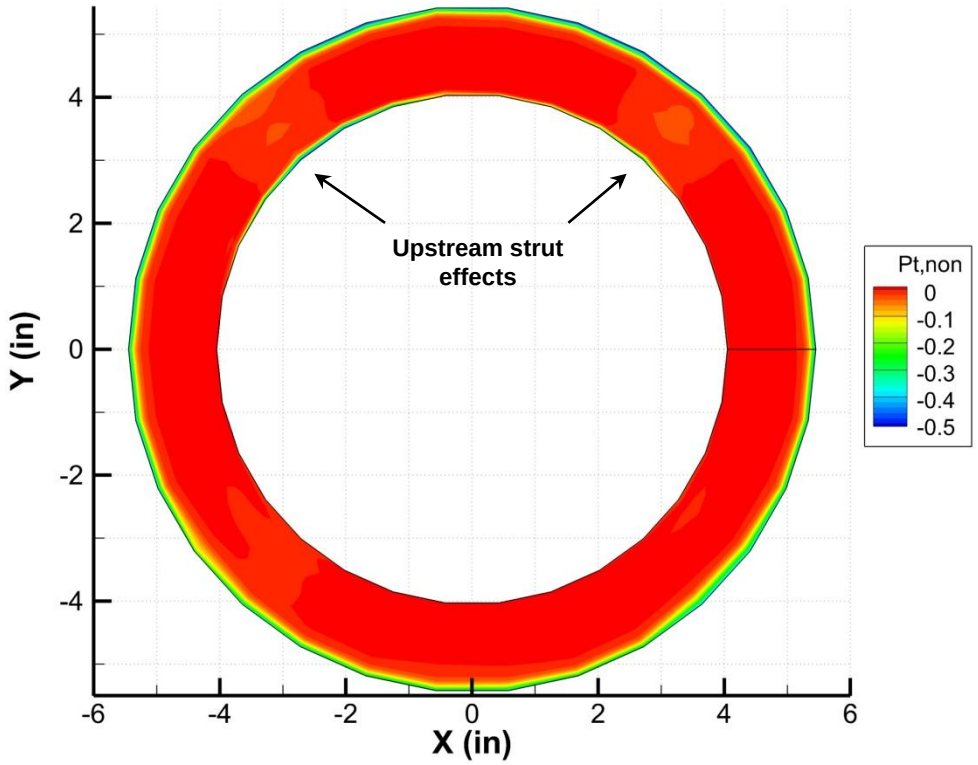

Fig. 3.5 Nondimensionalized total pressure contour at MP0 for the baseline configuration.

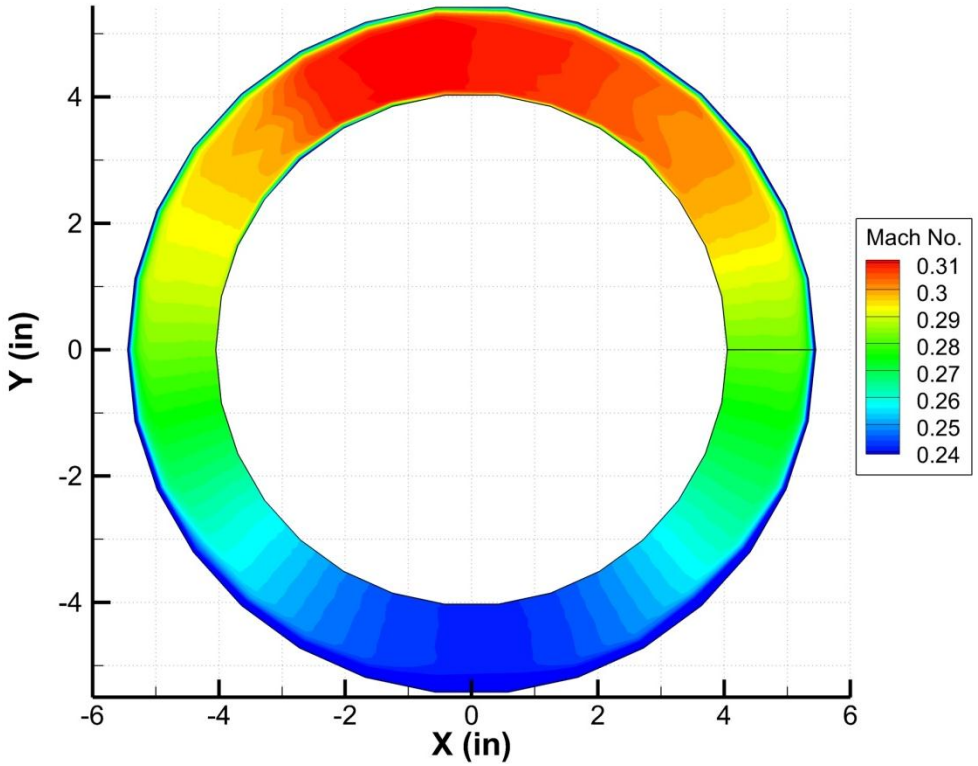

Fig. 3.6 Mach number contour at MP0 for the baseline configuration.

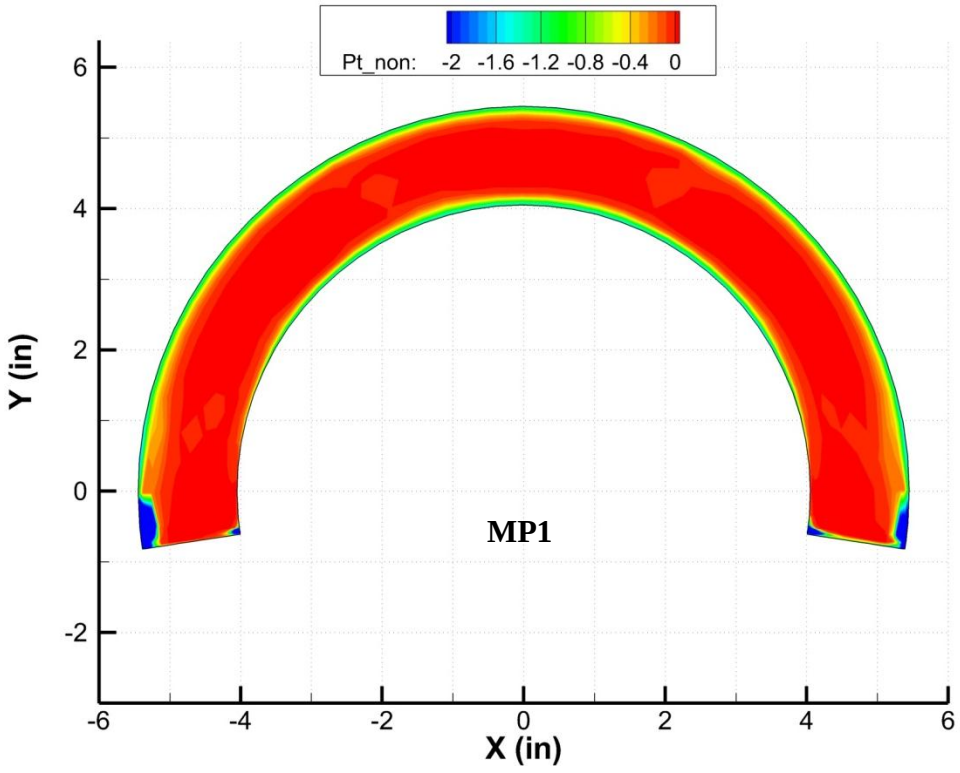

(a)

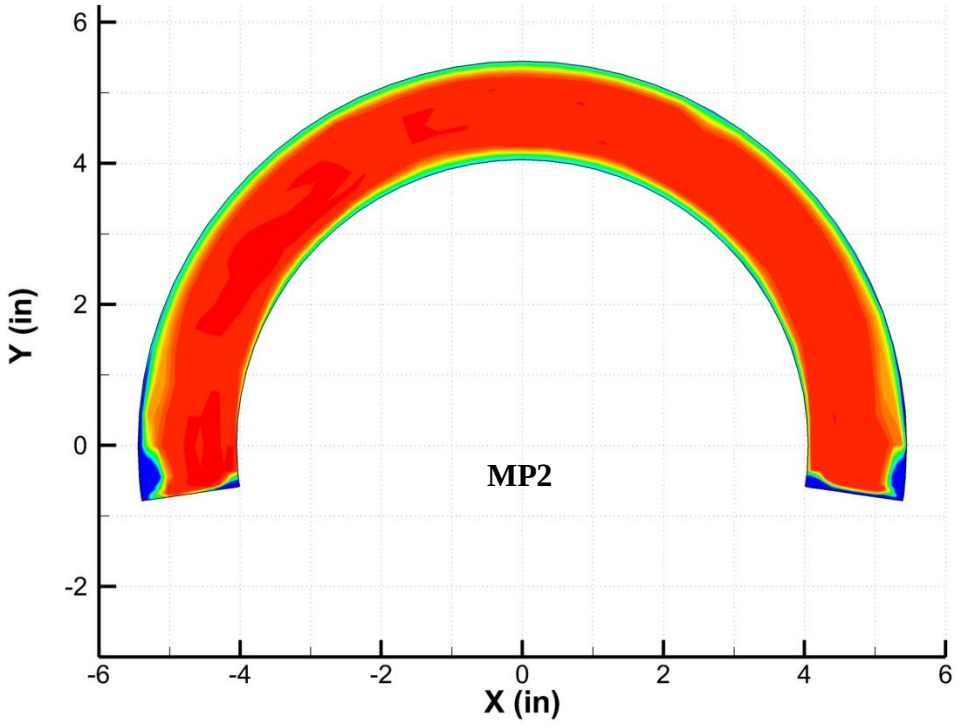

(b)

Fig. 3.7 Total pressure contours within the constant-area blocked section for the baseline configuration.

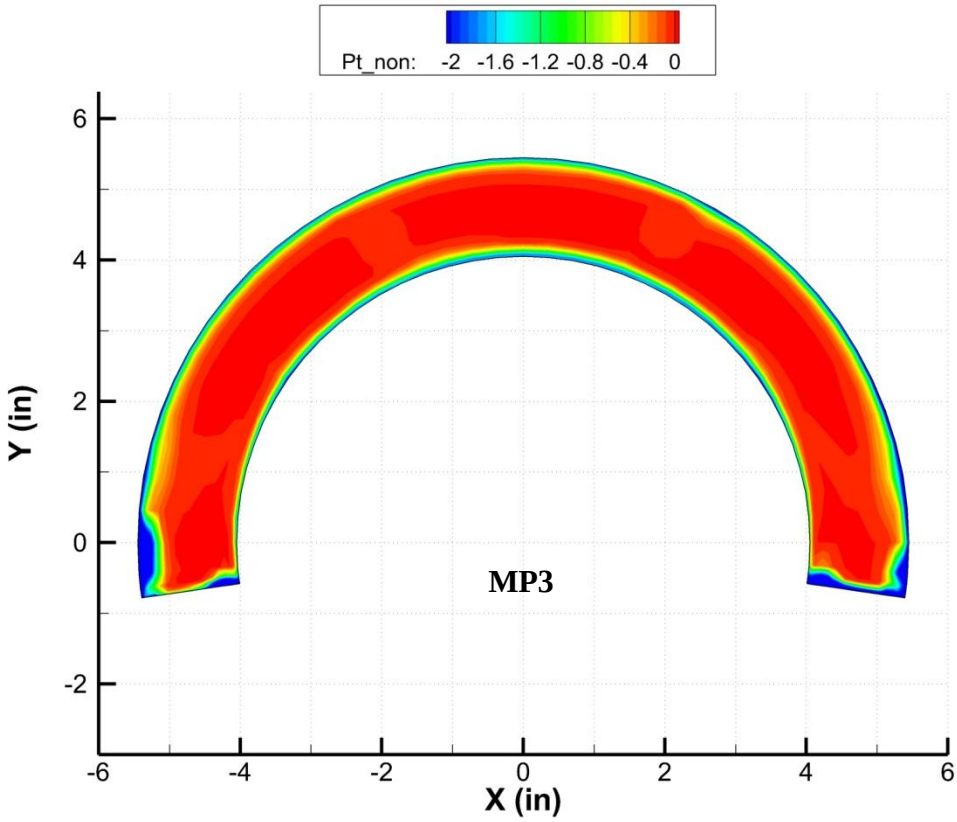

(c)

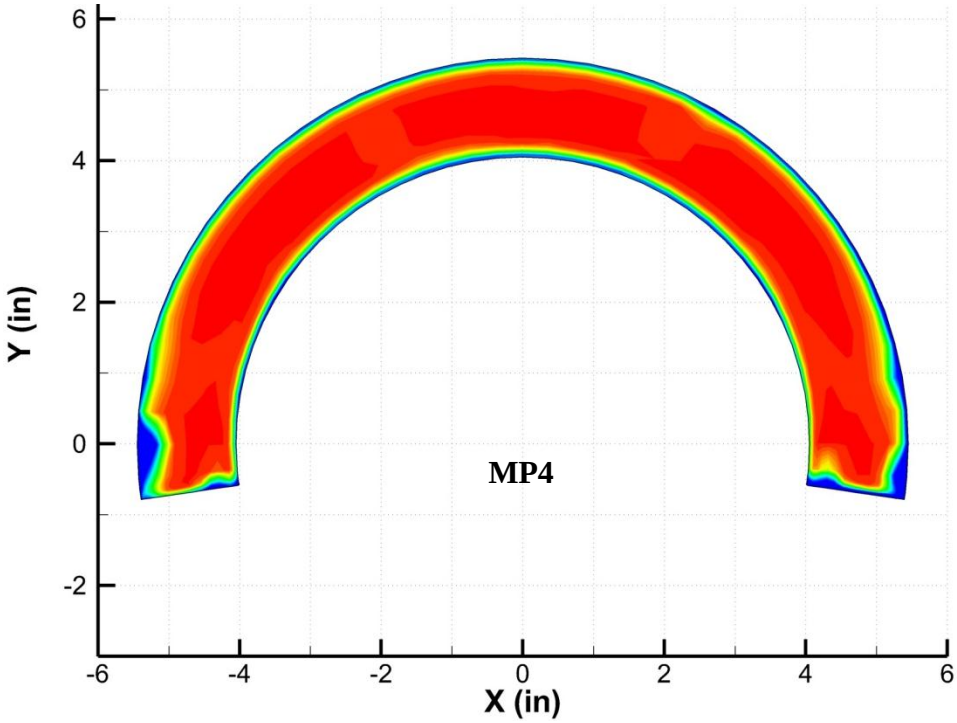

(d)

Fig. 3.7 (continued)

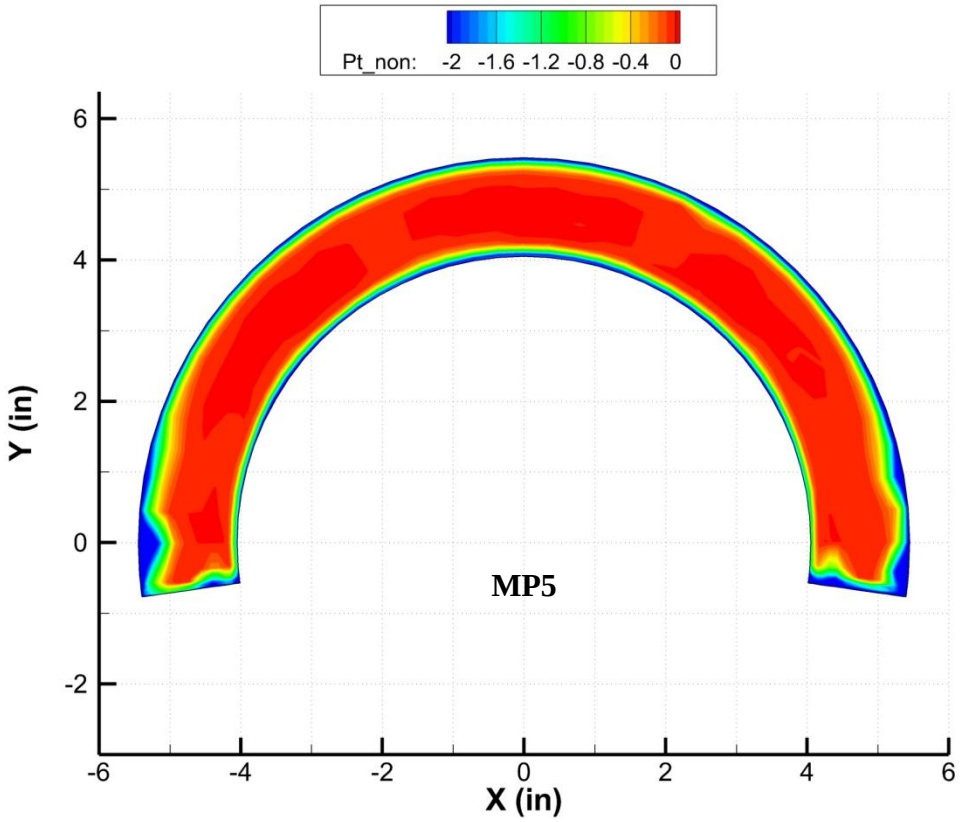

(e)

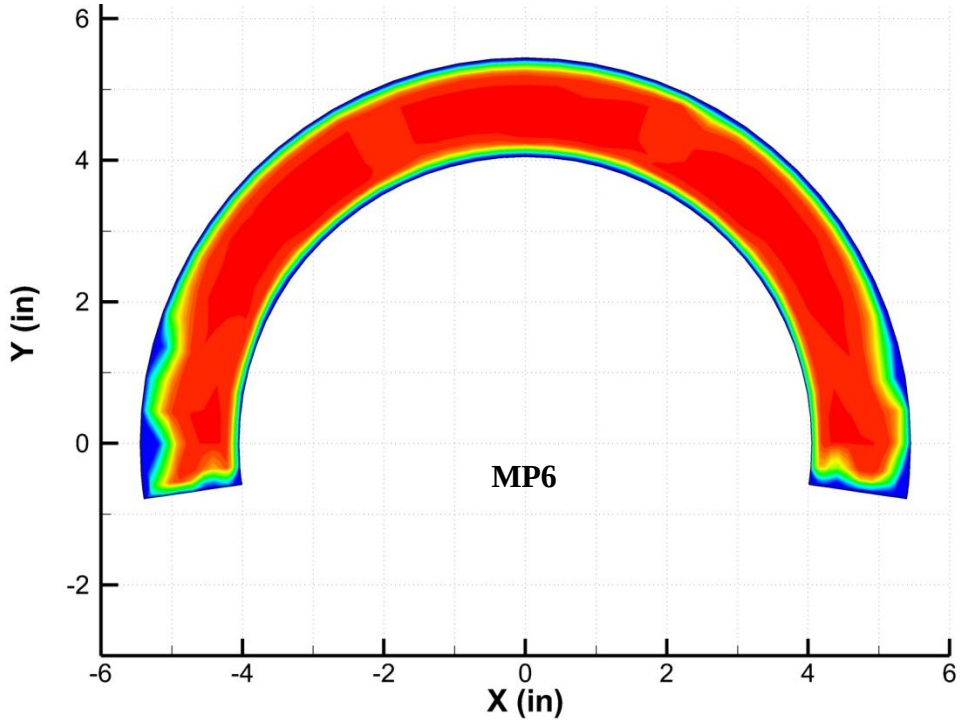

(f)

Fig. 3.7 (continued)

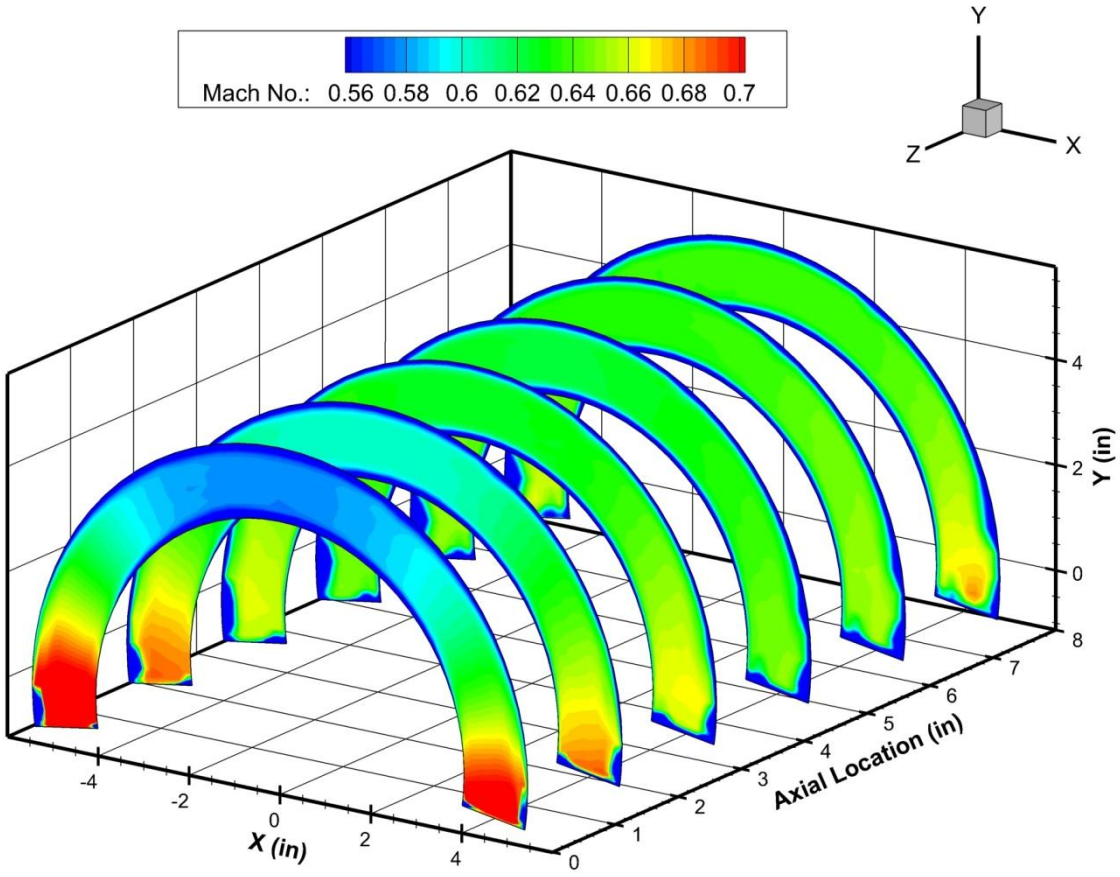

Fig. 3.8 Mach number contours within the constant-area blocked section for the baseline configuration.

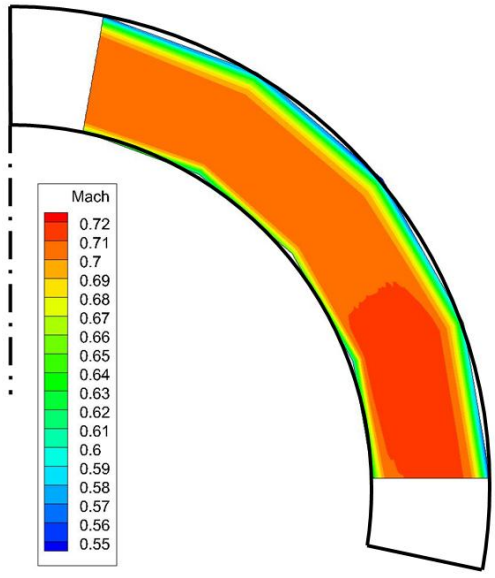

Fig. 3.9 Mach number contour at a plane comparable to MP6 within the aft bypass experiment.[22]

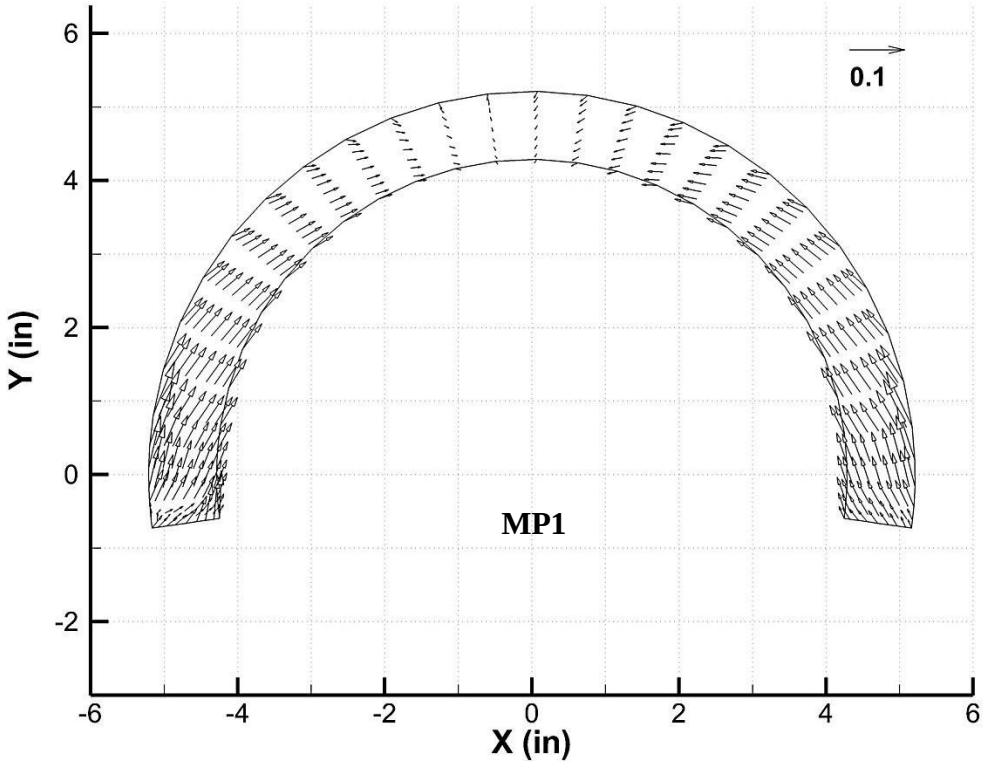

(a)

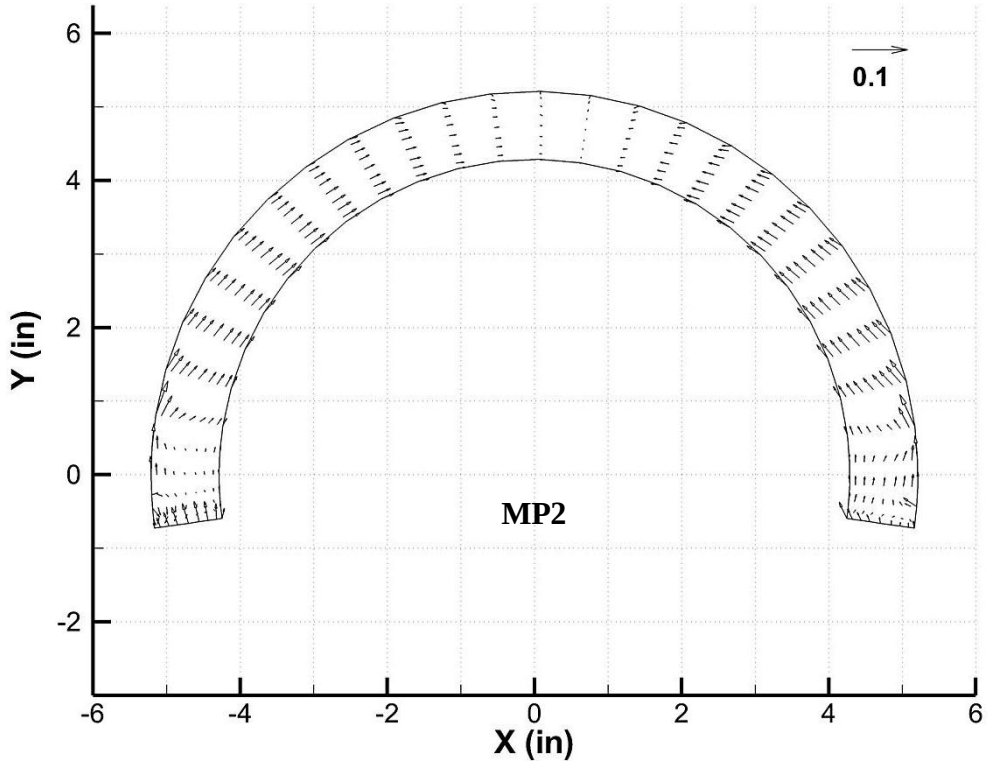

(b)

Fig. 3.10 In-plane Mach number vectors measured with the five-hole probe for the baseline model configuration.

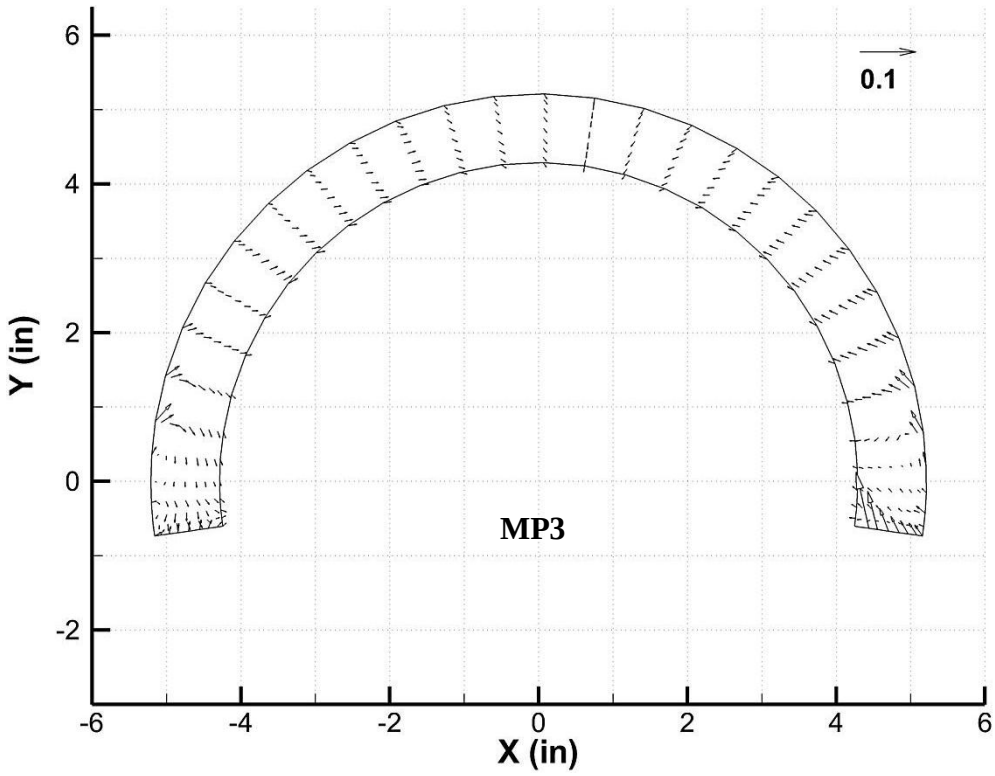

(c)

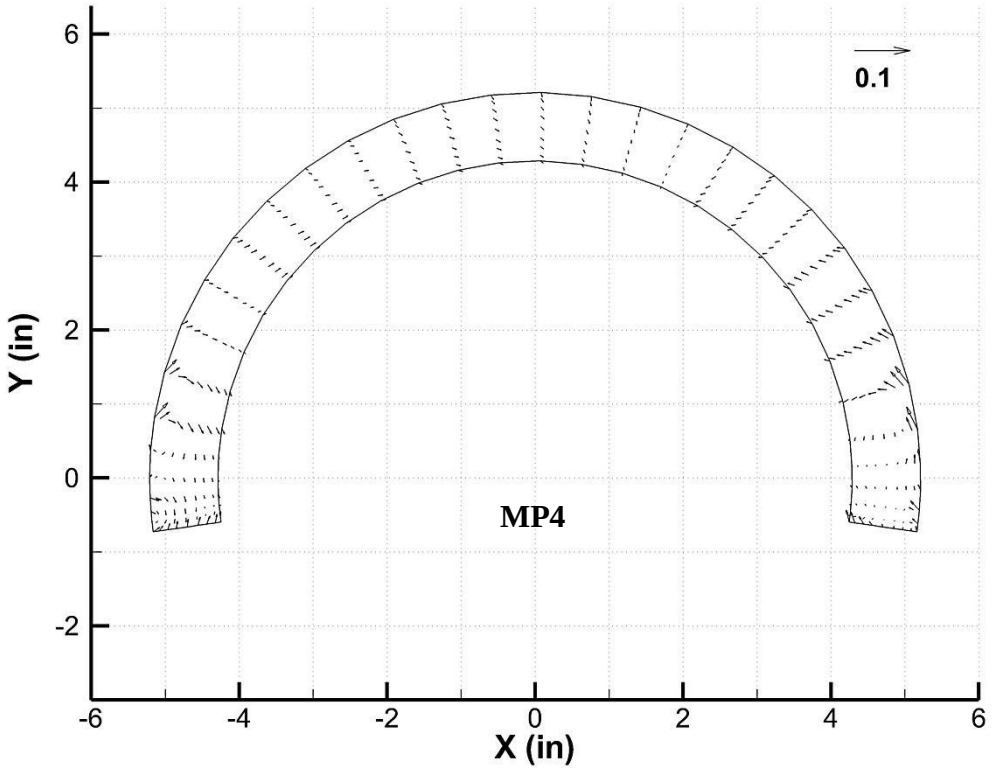

(d)

Fig. 3.10 (continued)

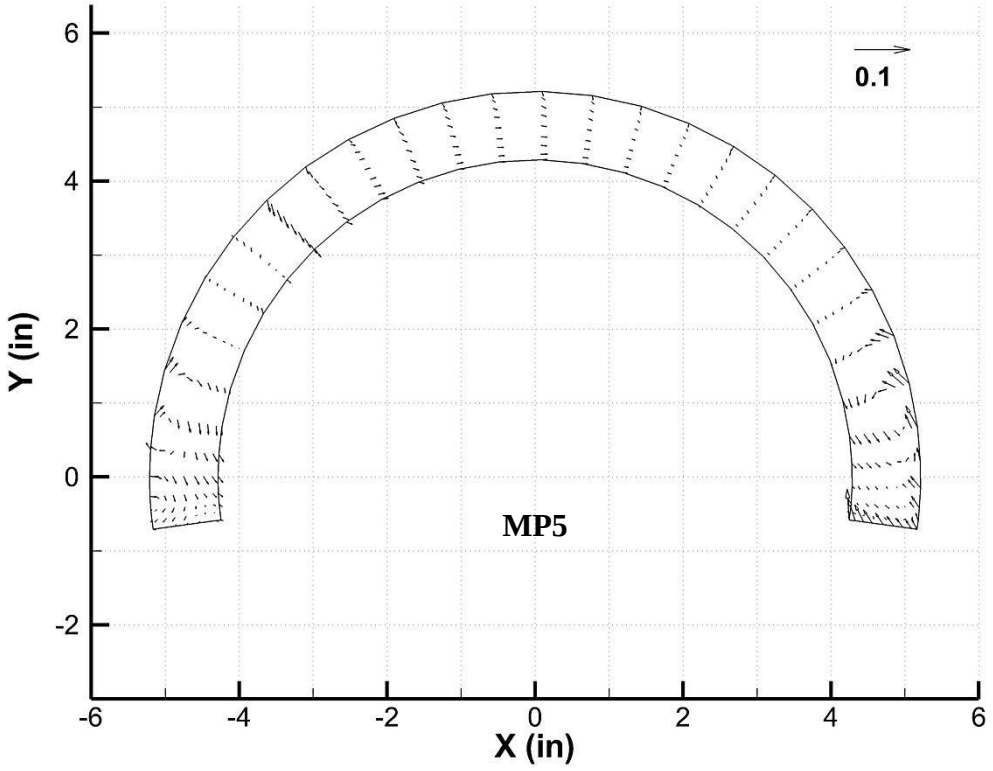

(e)

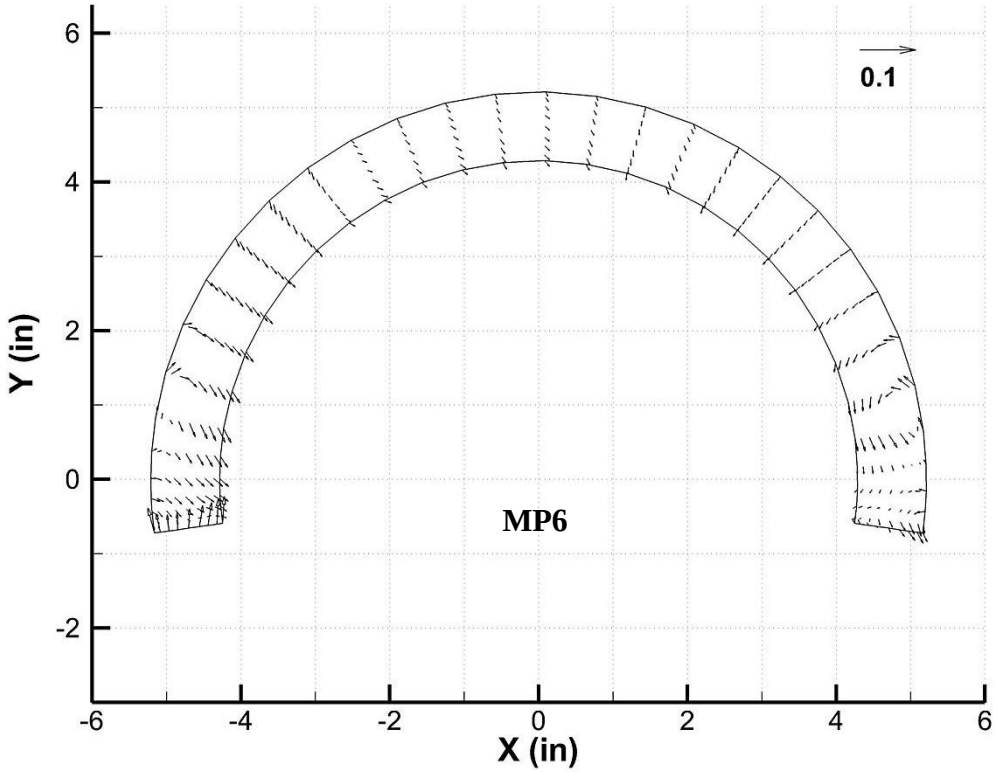

(f)

Fig. 3.10 (continued)

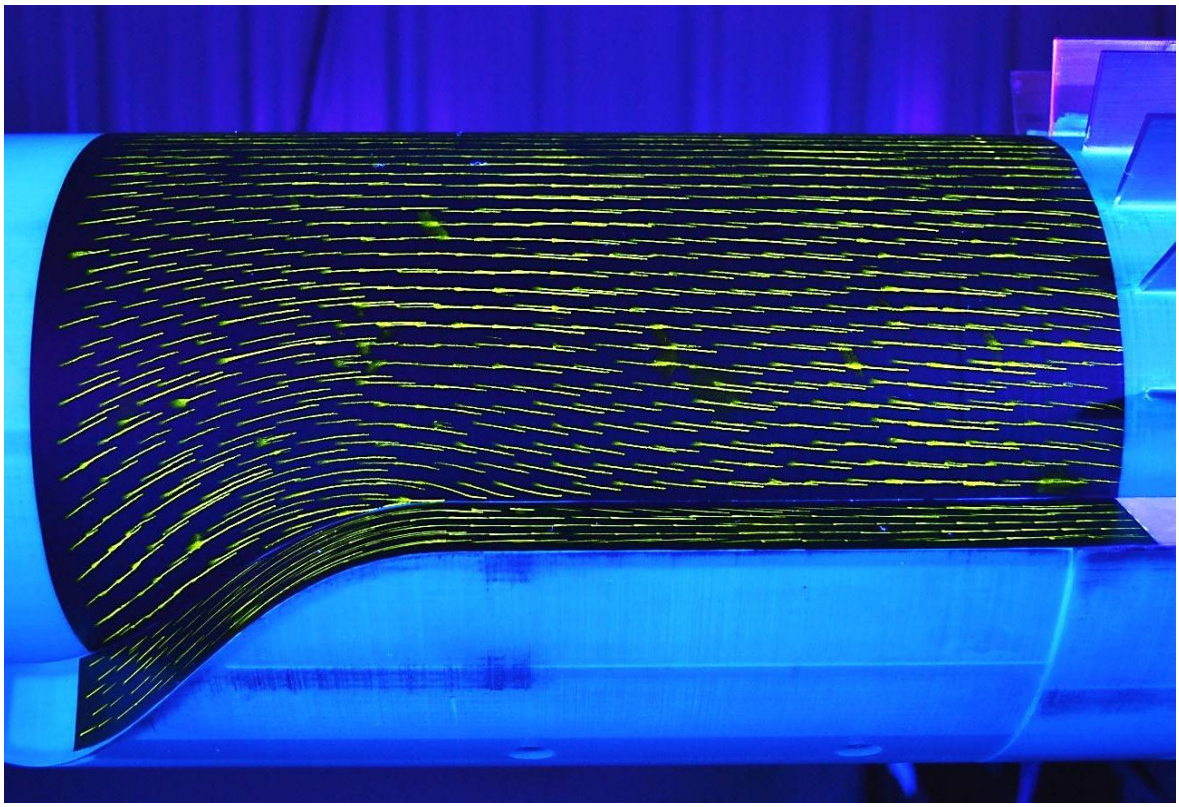

Fig. 3.11 Surface oil-flow visualization on the baseline model configuration.

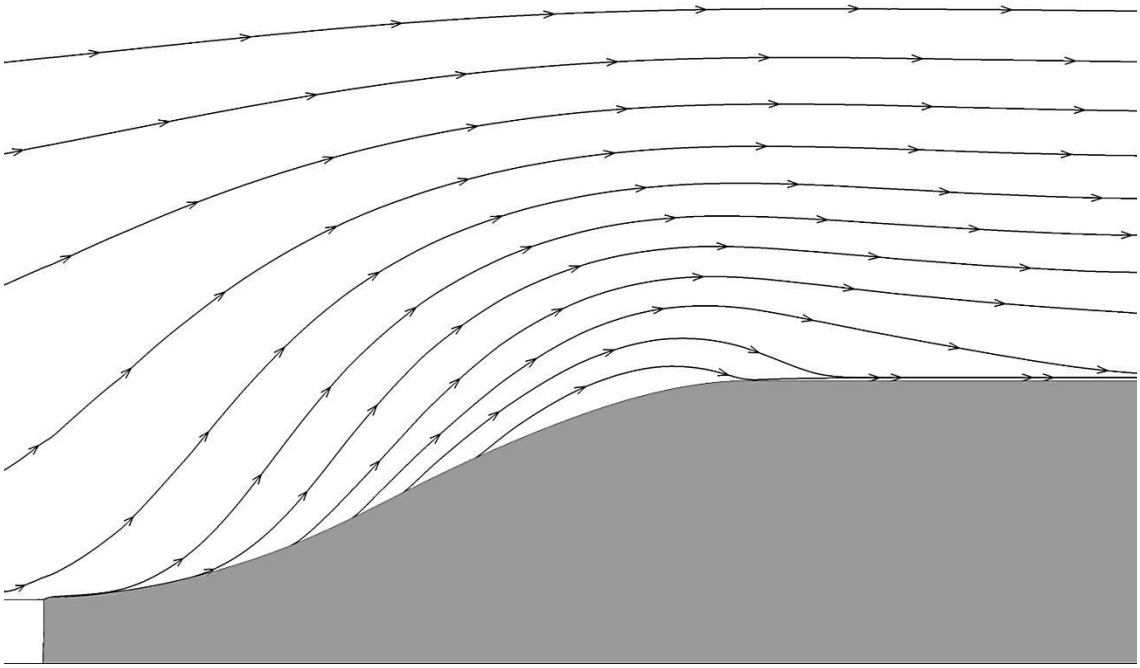

(a)

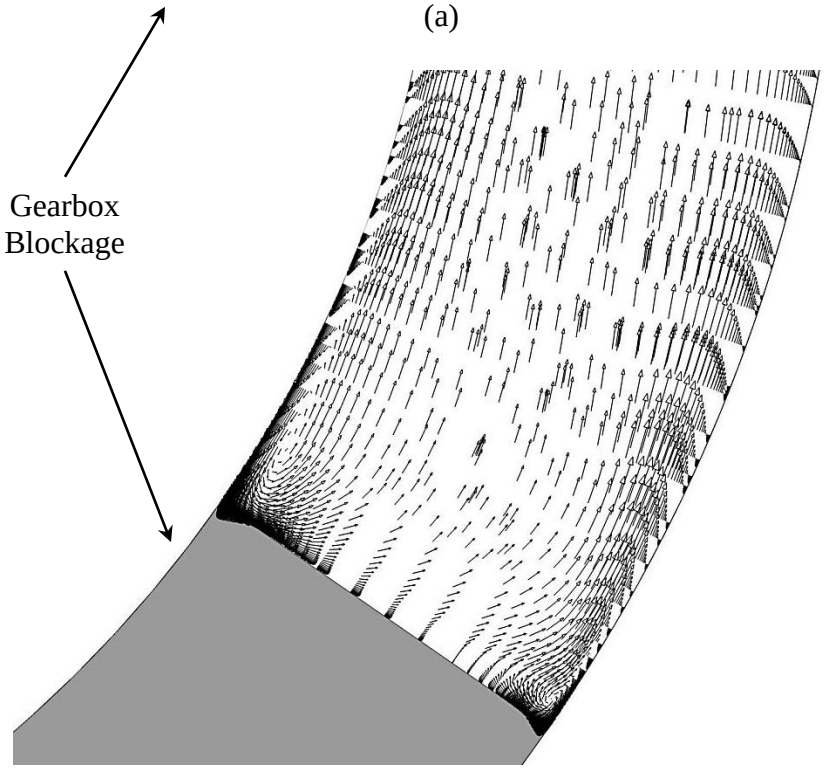

(b)

Fig. 3.12 Computational simulation of (a) shear stress streamlines along the model centerbody and (b) in-plane velocity vectors near the gearbox at MP1.[20,29]

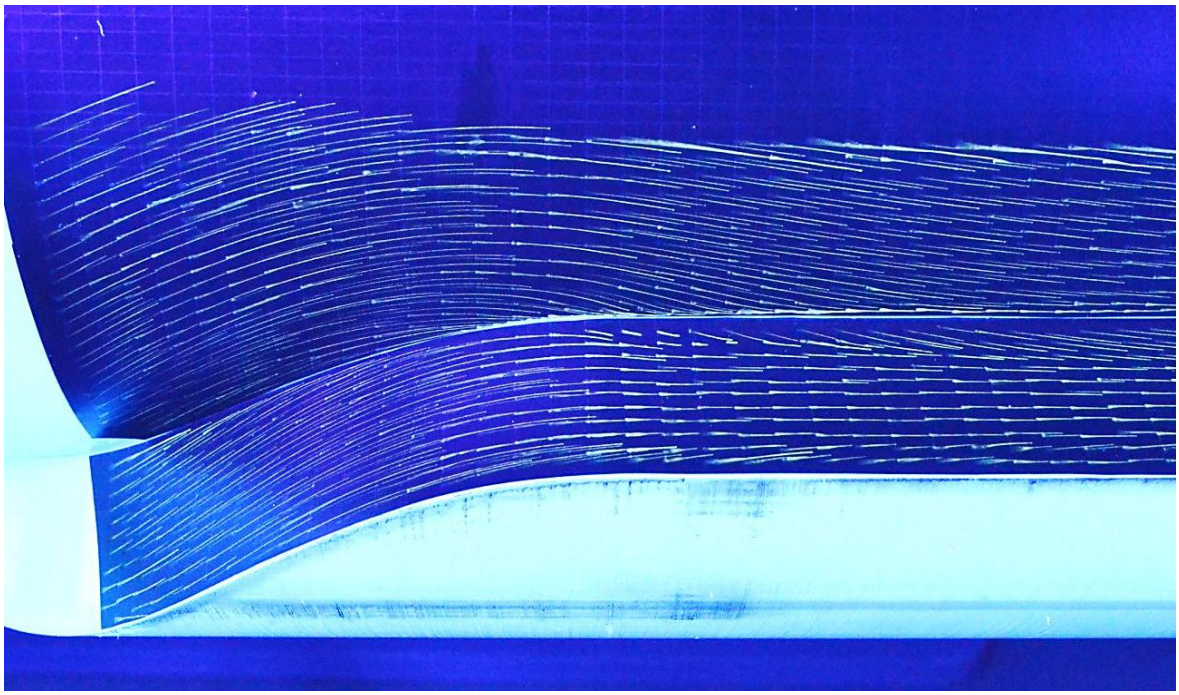

Fig. 3.13 Surface oil-flow visualization at the gearbox/centerbody junction.

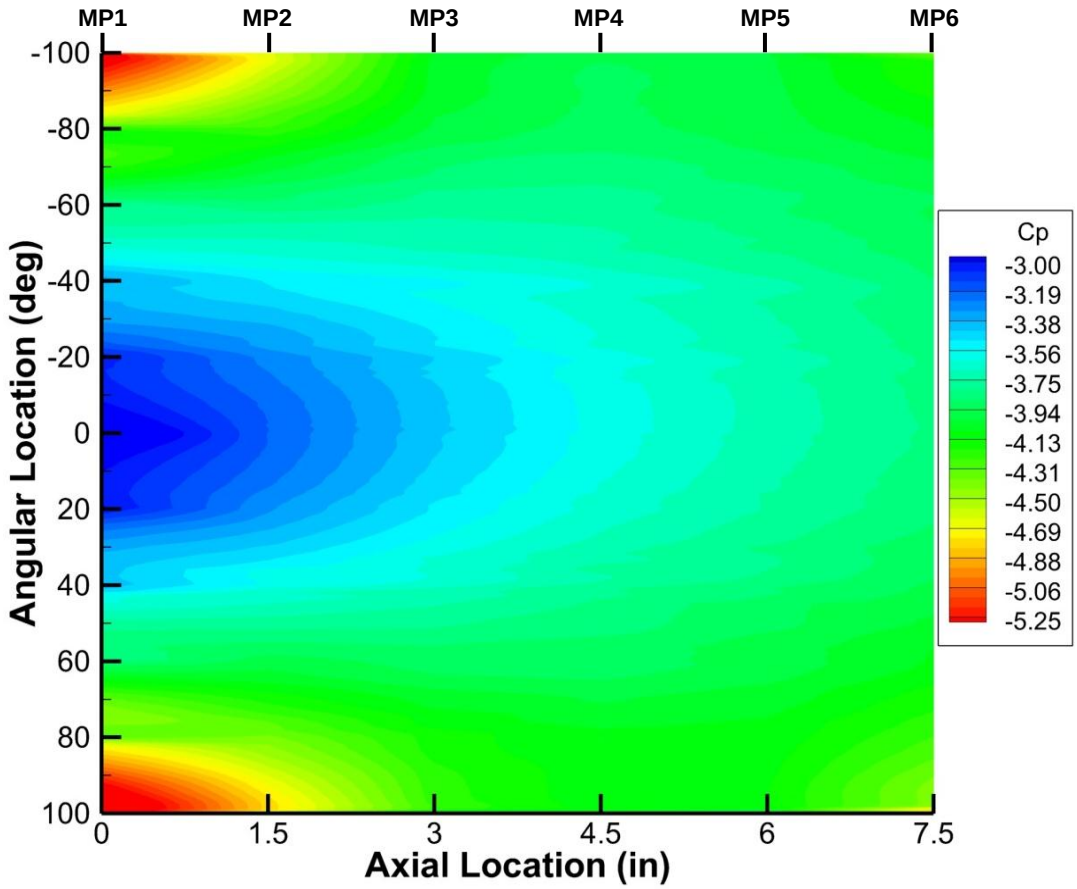

Fig. 3.14 Static pressure distribution in the constant-area blocked section for the vaned model configuration.

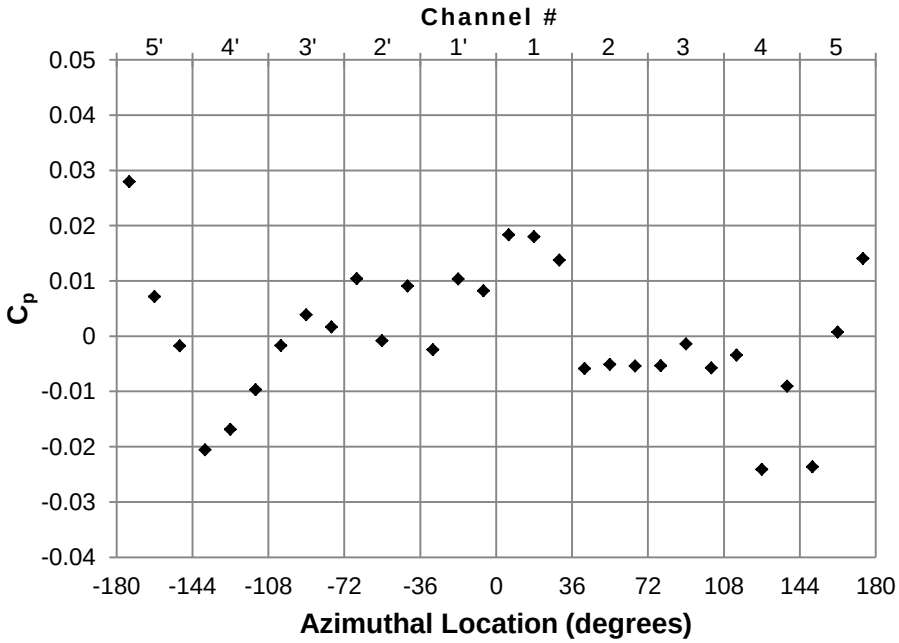

Fig. 3.15 Azimuthal static pressure distribution at MP0 for the vaned model configuration.

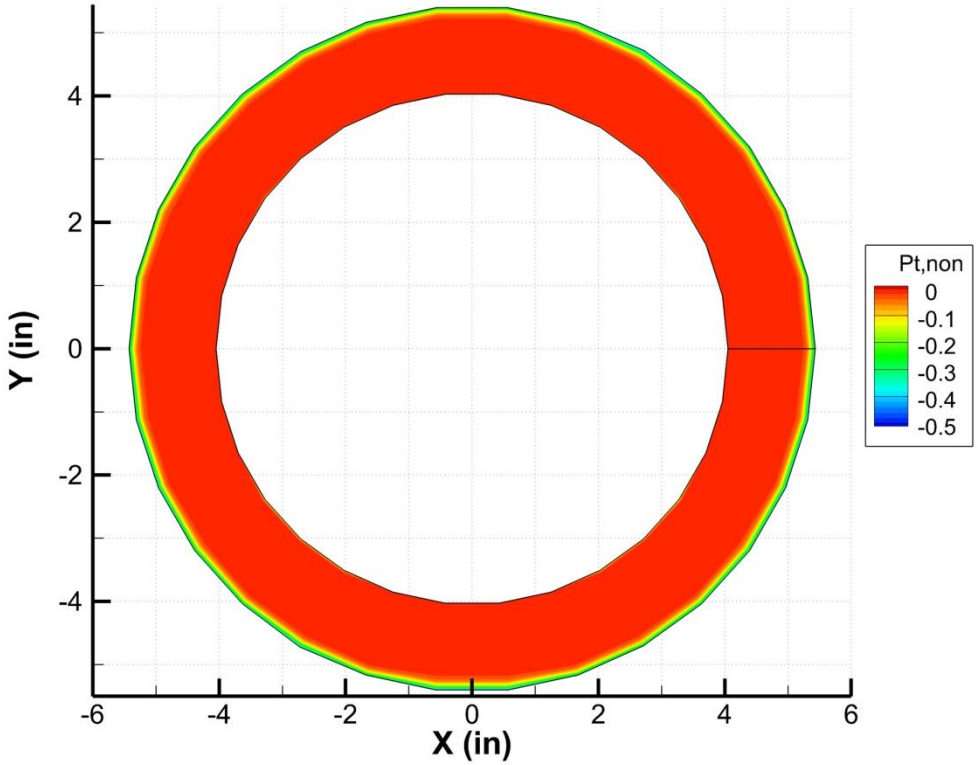

Fig. 3.16 Nondimentionalized total pressure contour at MP0 for the vaned configuration.

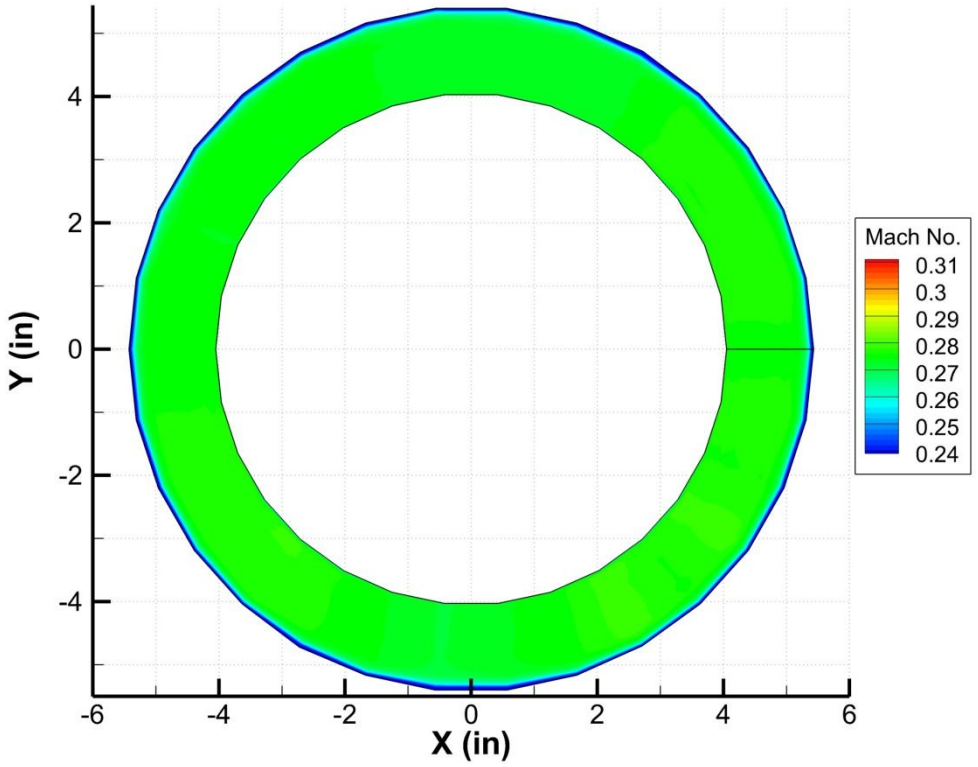

Fig. 3.17 Mach number contour at MP0 for the vaned configuration.

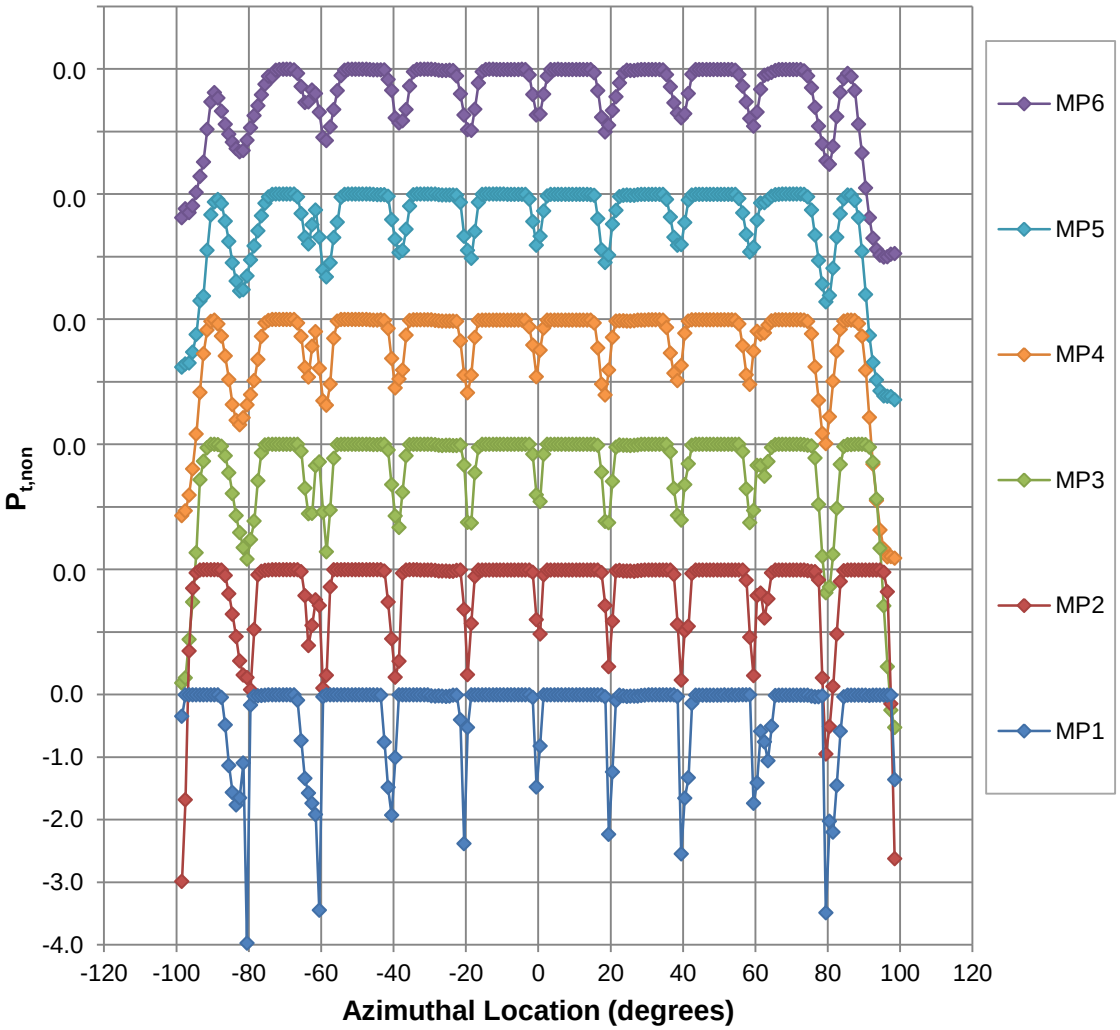

Fig. 3.18 Azimuthal total pressure surveys within the constant-area blocked section aft of the forward guide vanes. (Data collected at R*=0.5.)

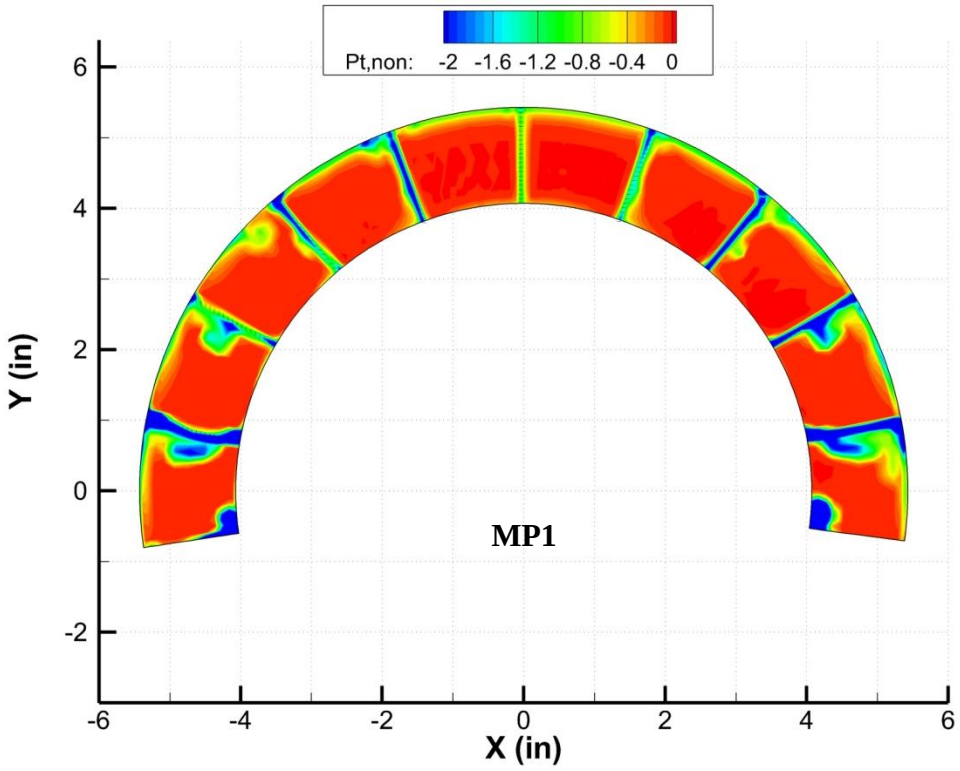

(a)

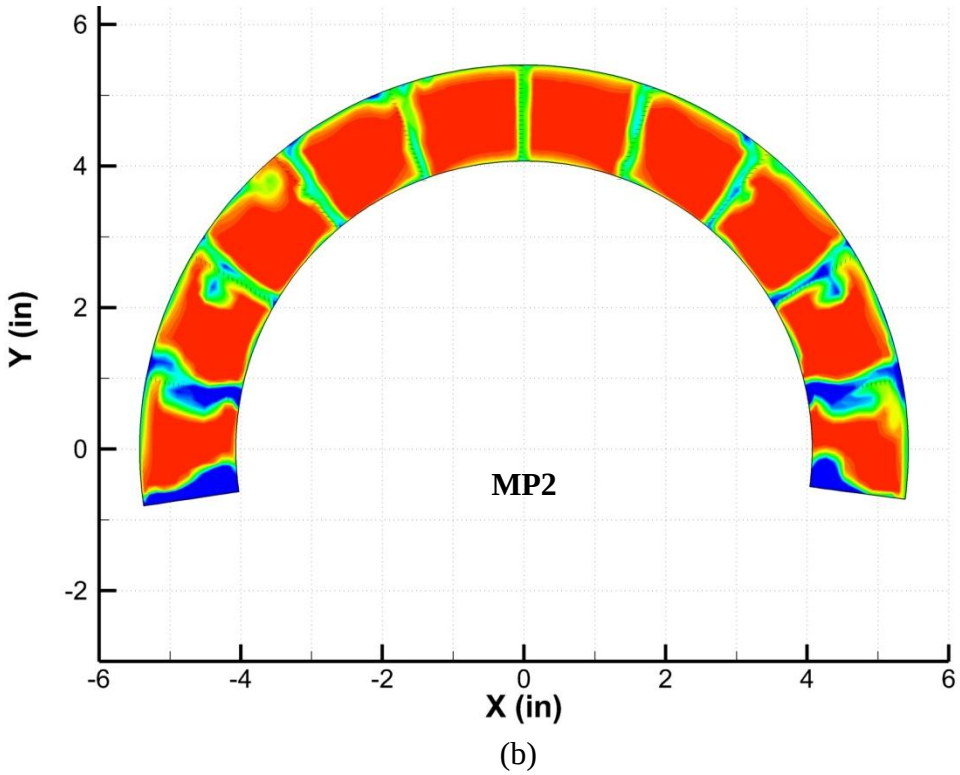

(b)

Fig. 3.19 Total pressure contours within the constant-area blocked section for the vaned configuration.

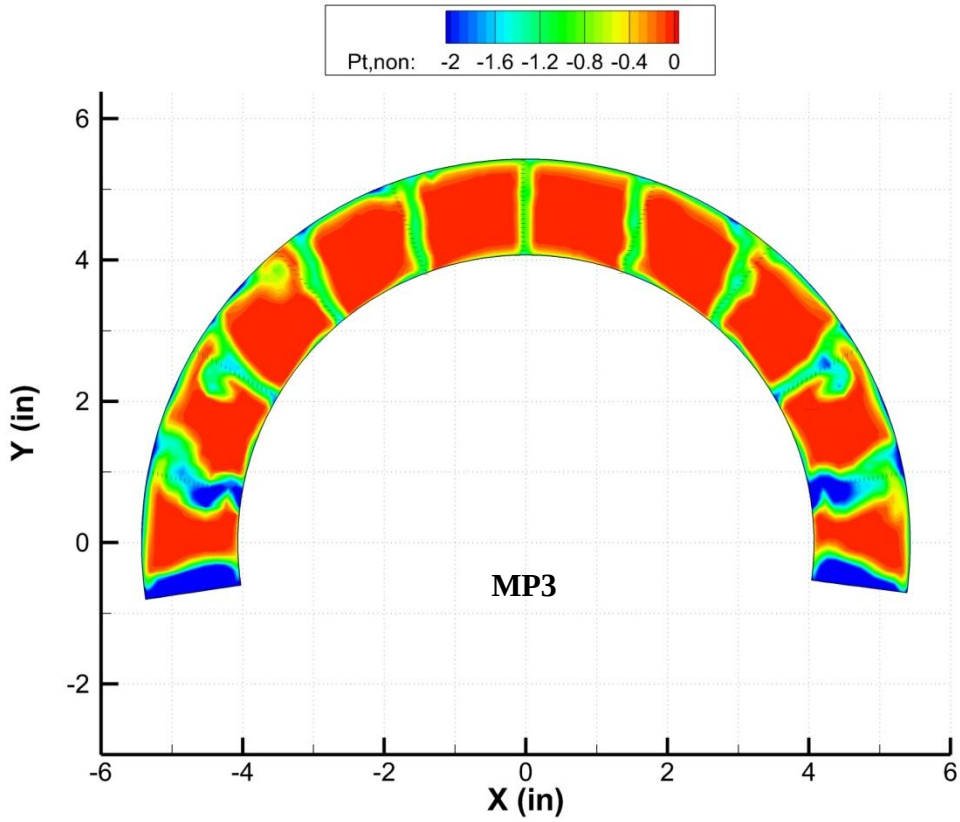

(c)

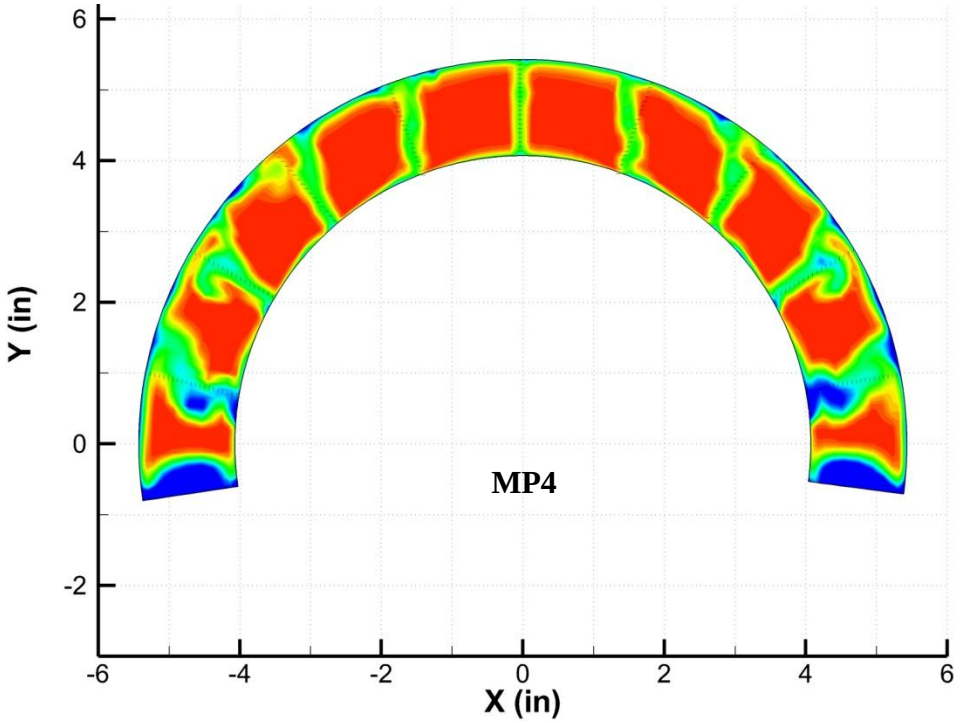

(d)

Fig. 3.19 (continued)

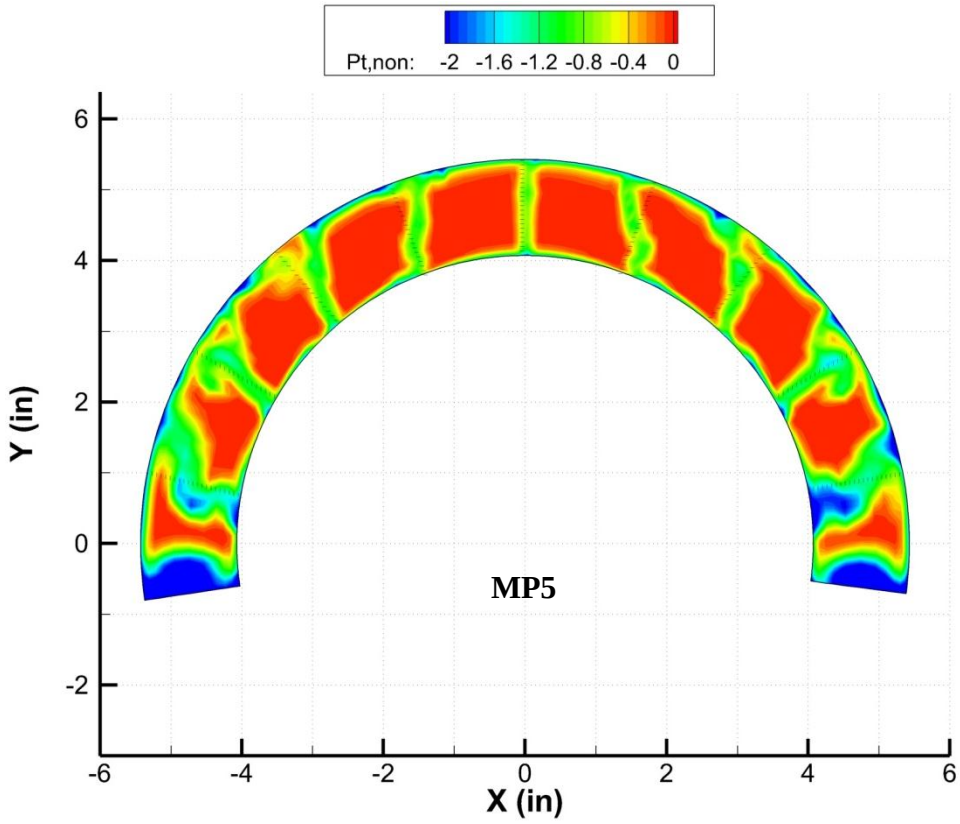

(e)

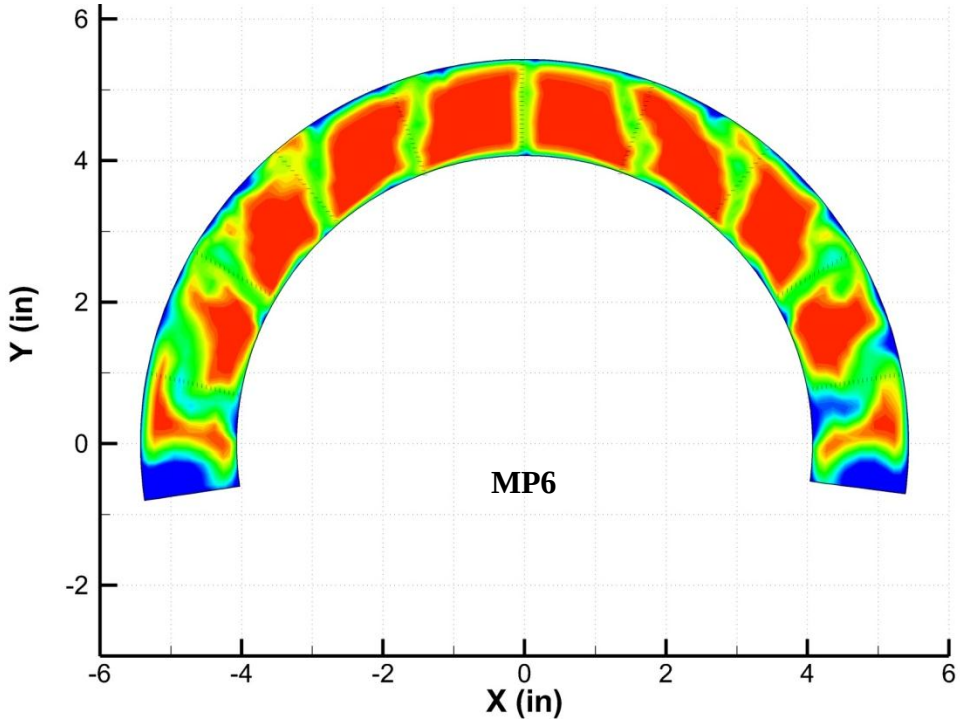

(f)

Fig. 3.19 (continued)

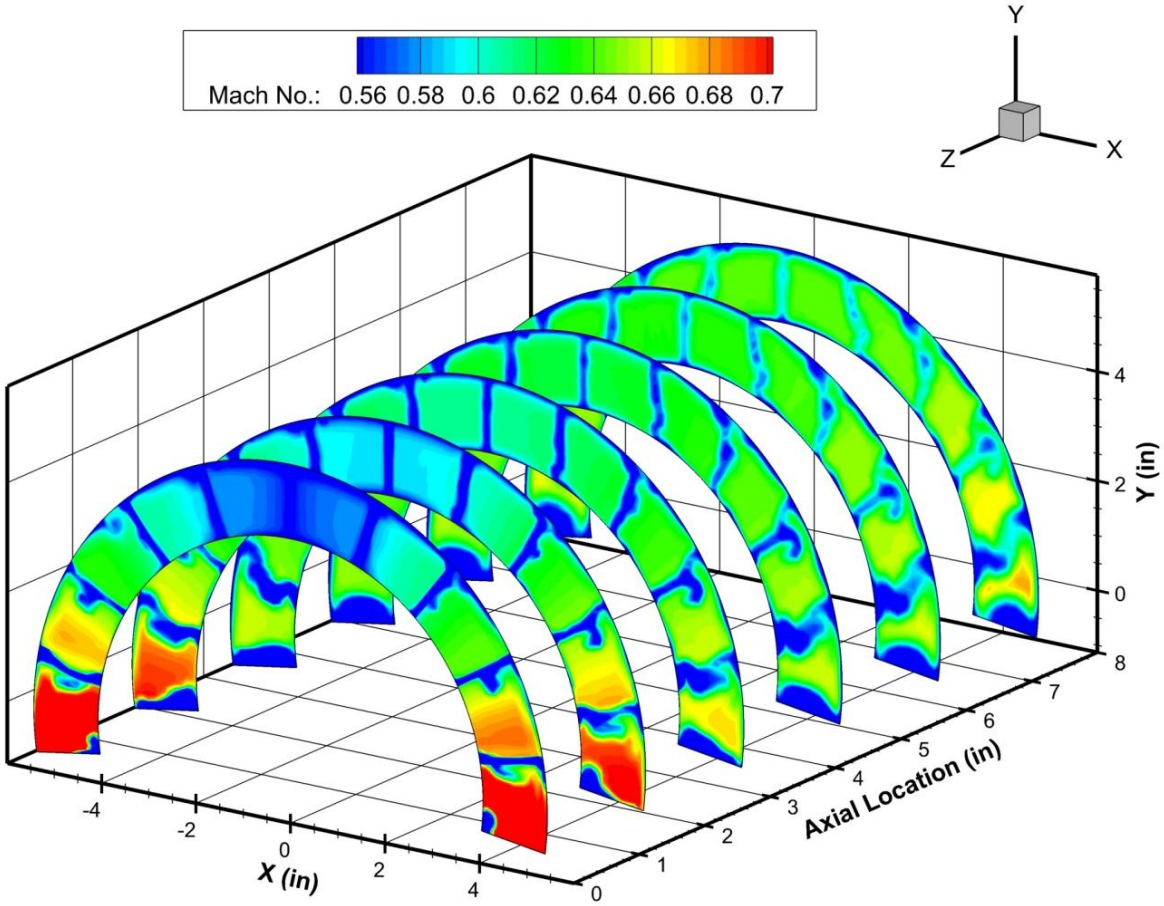

Fig. 3.20 Mach number contours within the constant-area blocked section for the vaned configuration.

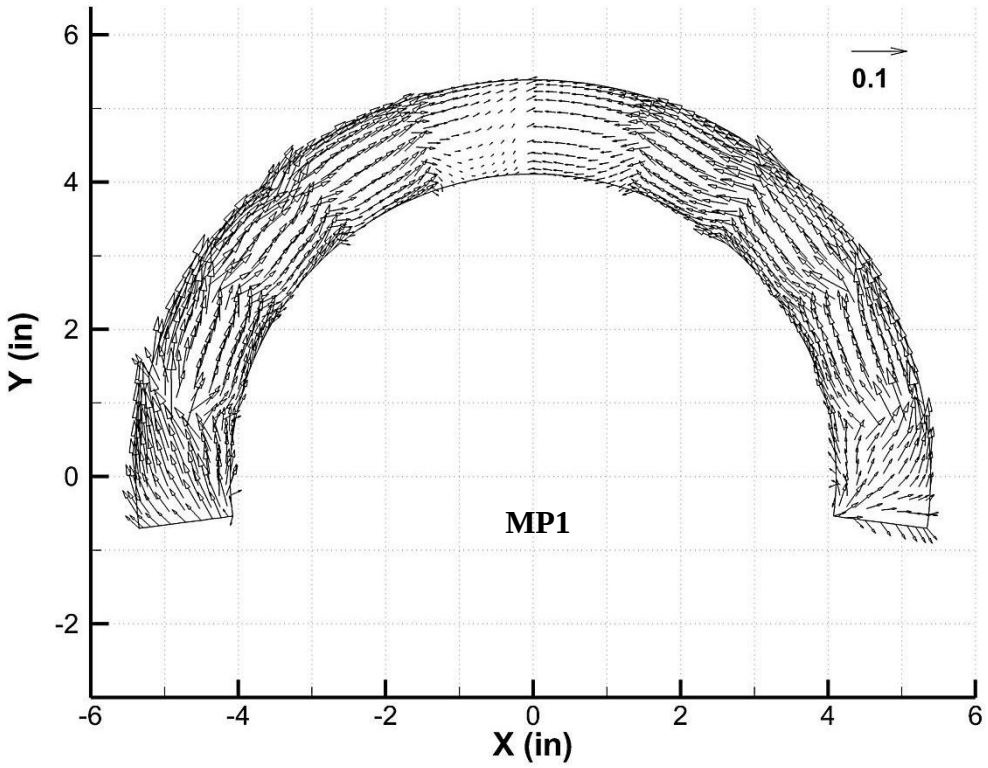

(a)

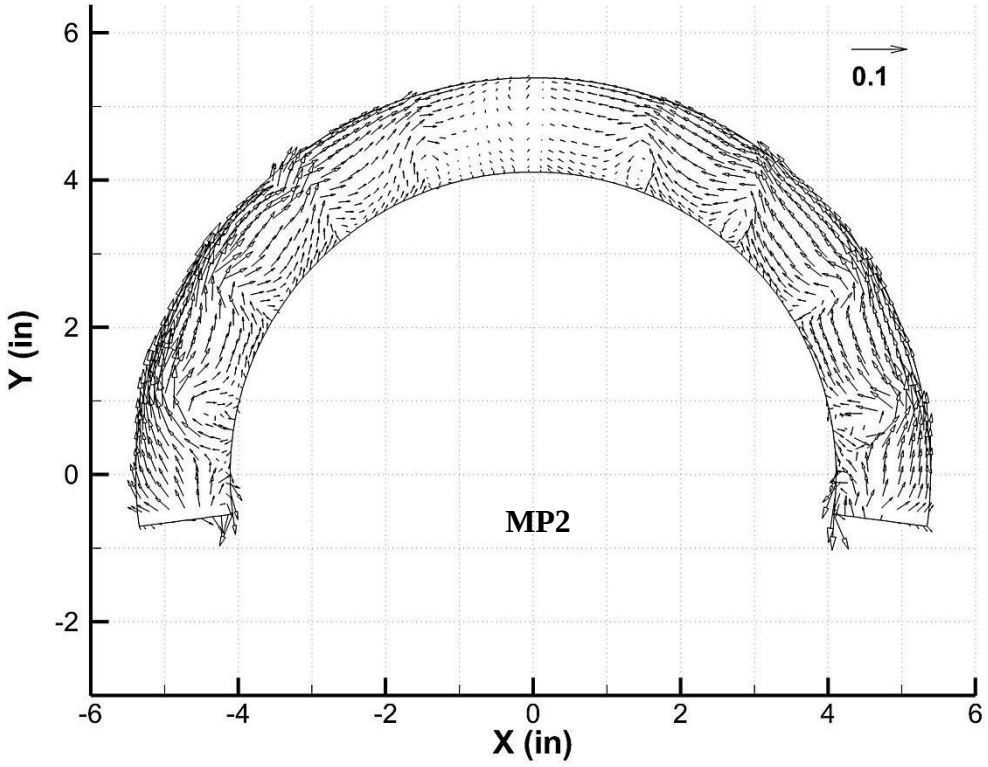

(b)

Fig. 3.21 In-plane Mach vectors measured with the five-hole probe for the vaned model configuration.

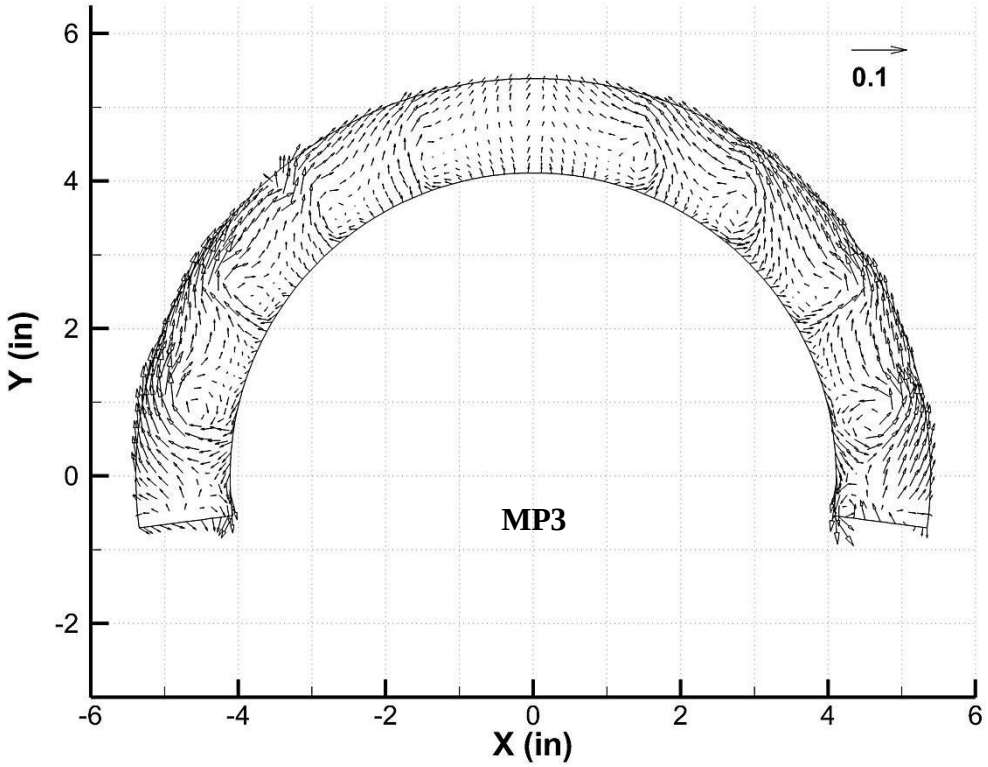

(c)

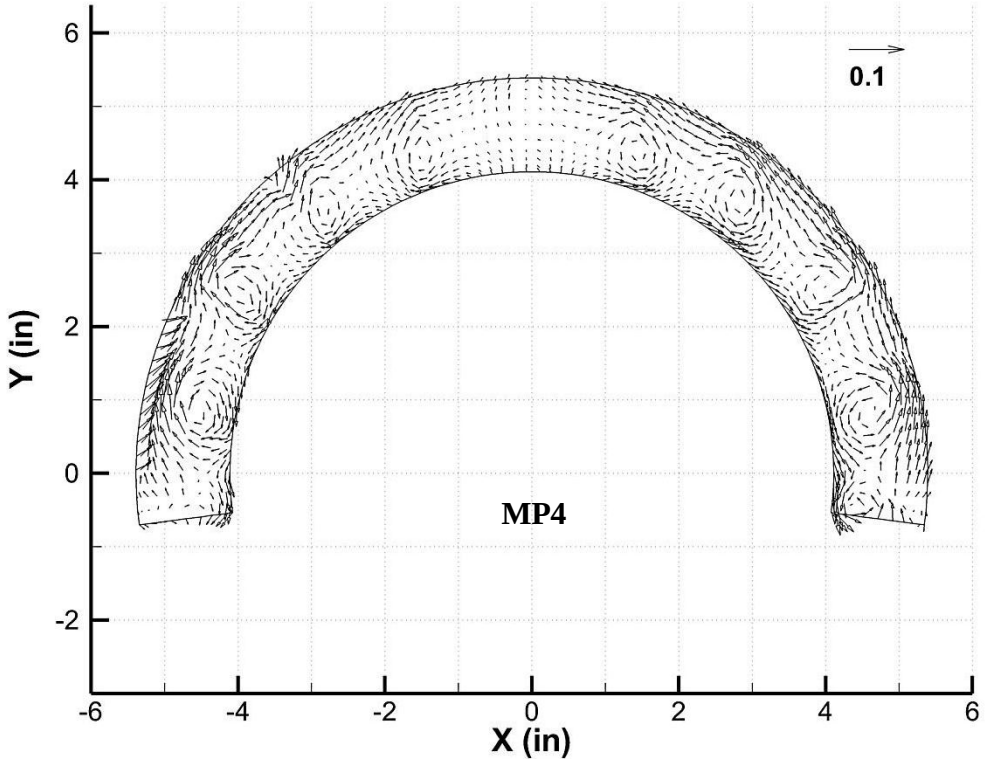

(d)

Fig. 3.21 (continued)

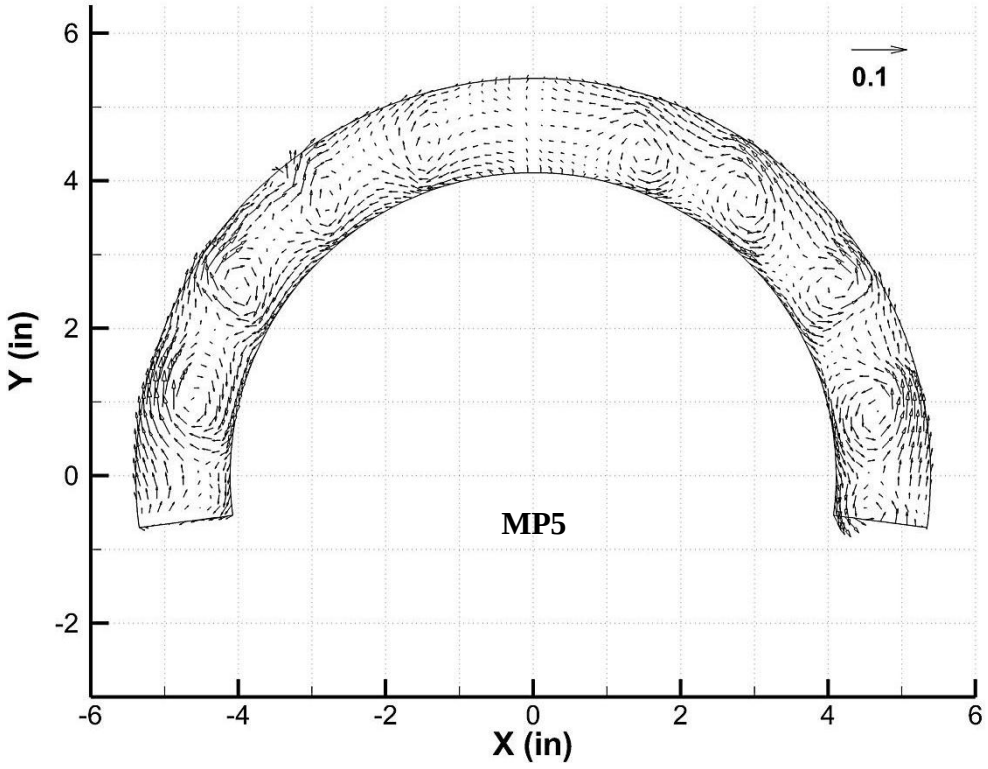

(e)

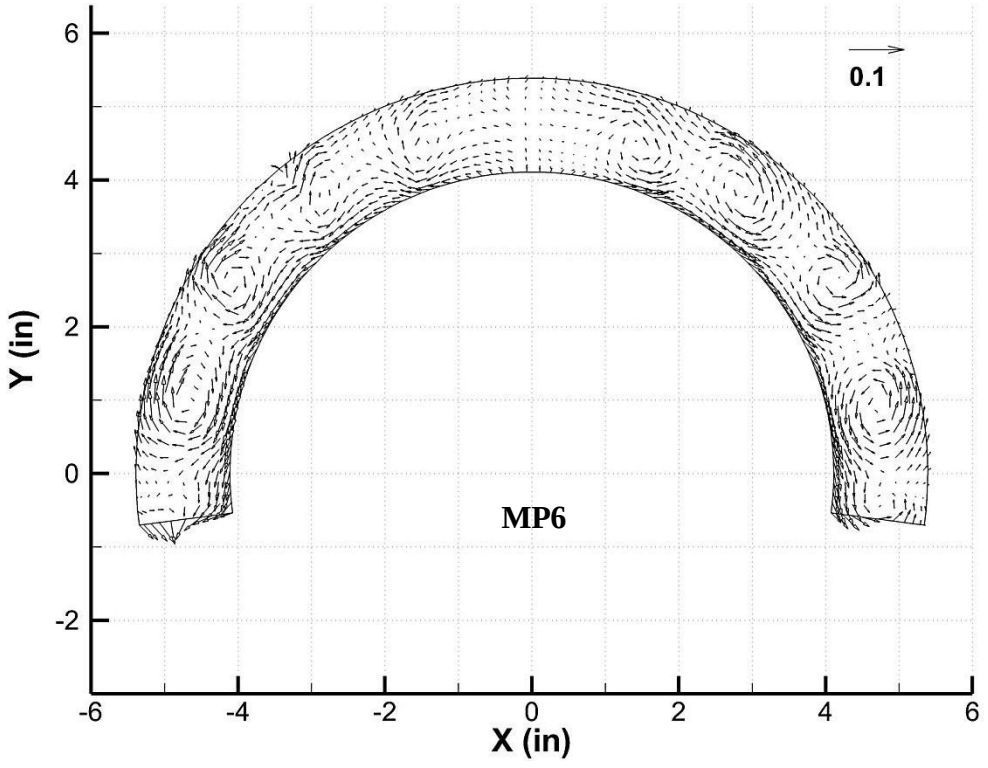

(f)

Fig. 3.21 (continued)

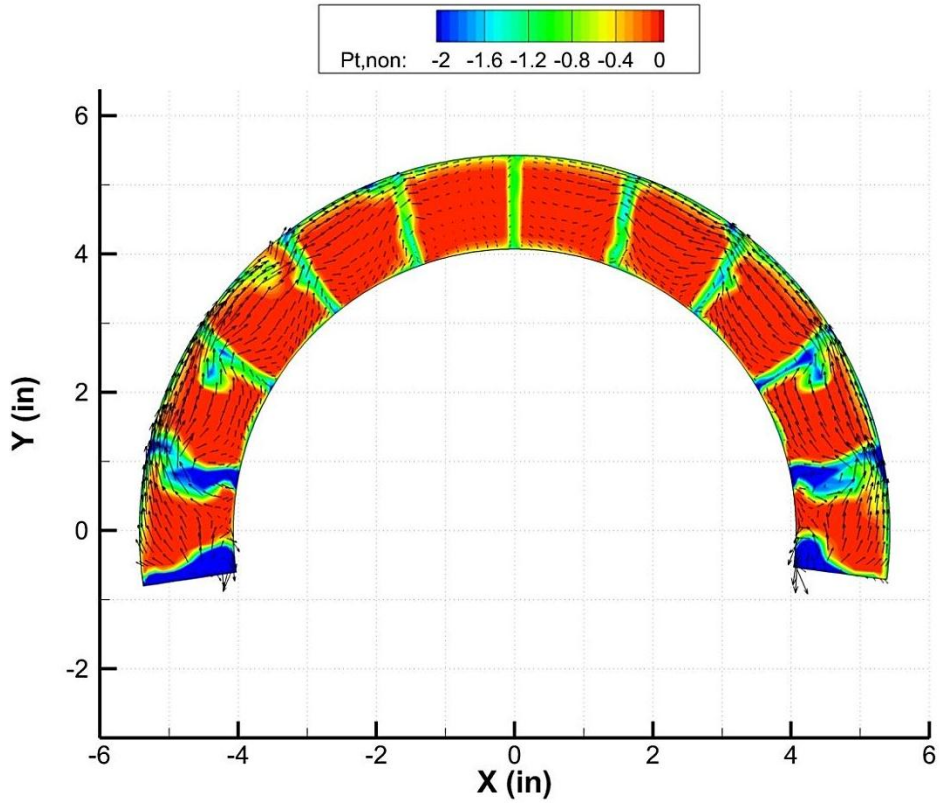

Fig. 3.22 In-plane Mach vectors superimposed with normalized total pressures at MP2.

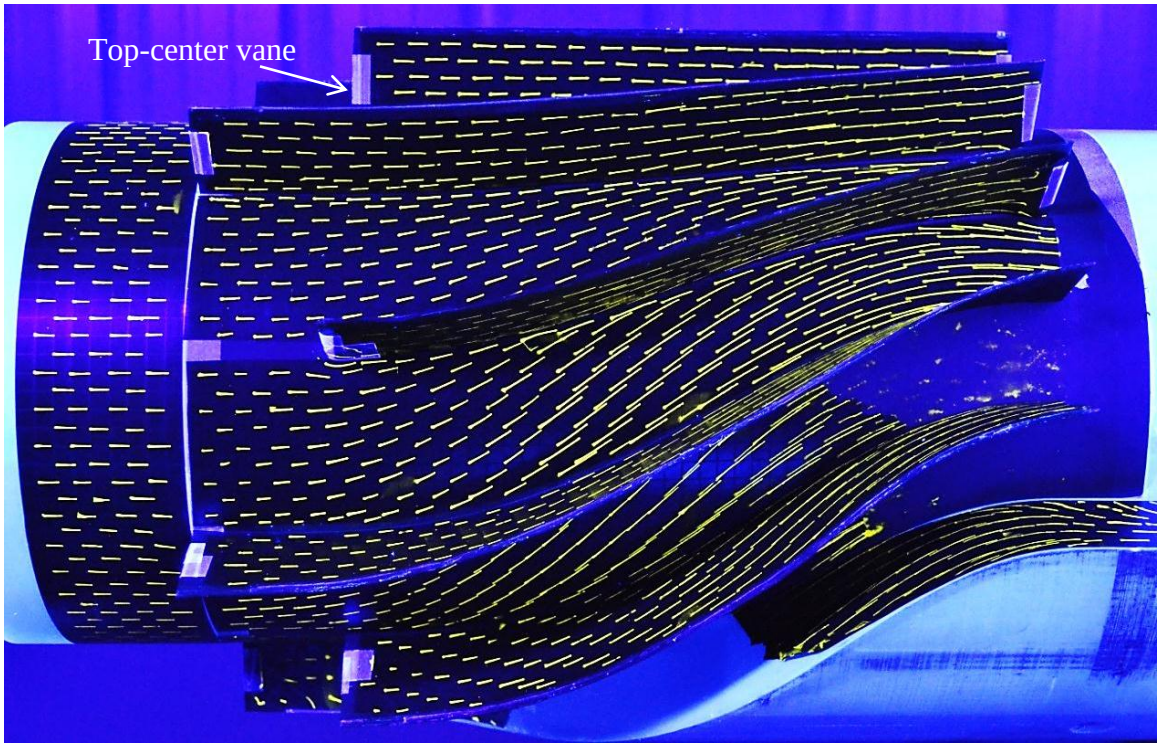

Fig. 3.23 Surface oil-flow visualization on the vaned model configuration.

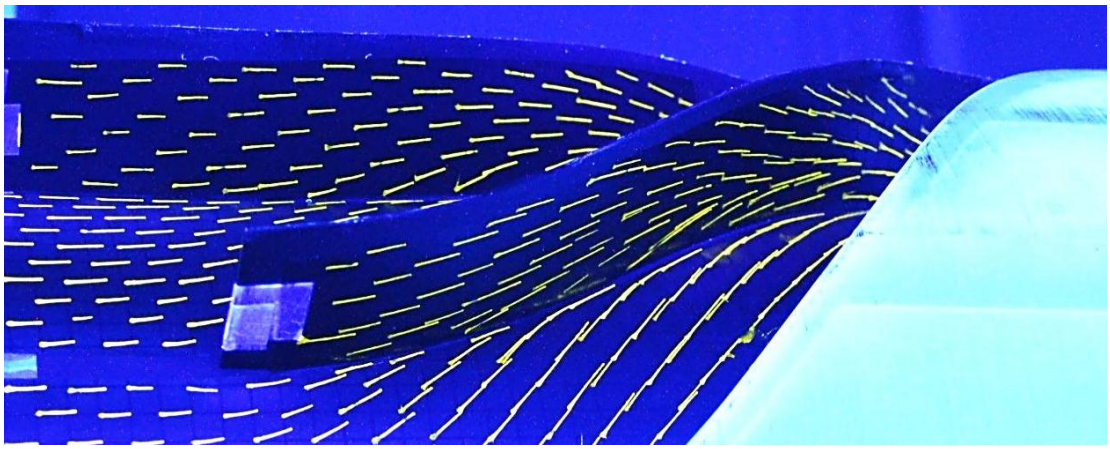

Fig. 3.24 Surface oil-flow visualization on the underside of the two most highly-curved vanes.

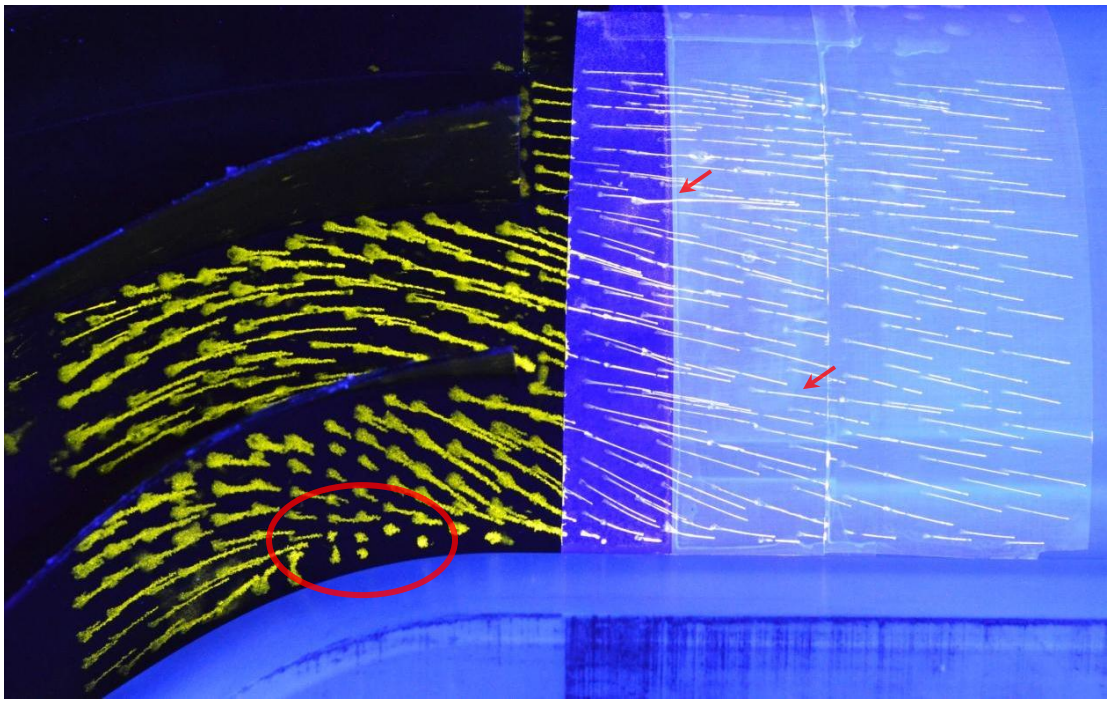

Fig. 3.25 Surface oil-flow visualization at the exit of channels 4 and 5.

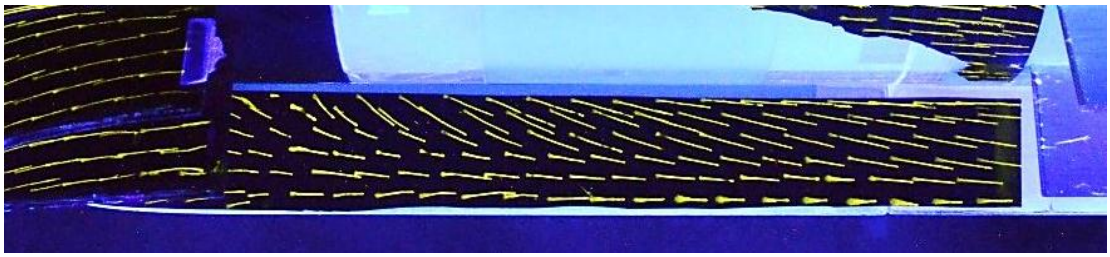

Fig. 3.26 Surface oil-flow visualization along the gearbox fairing wall.

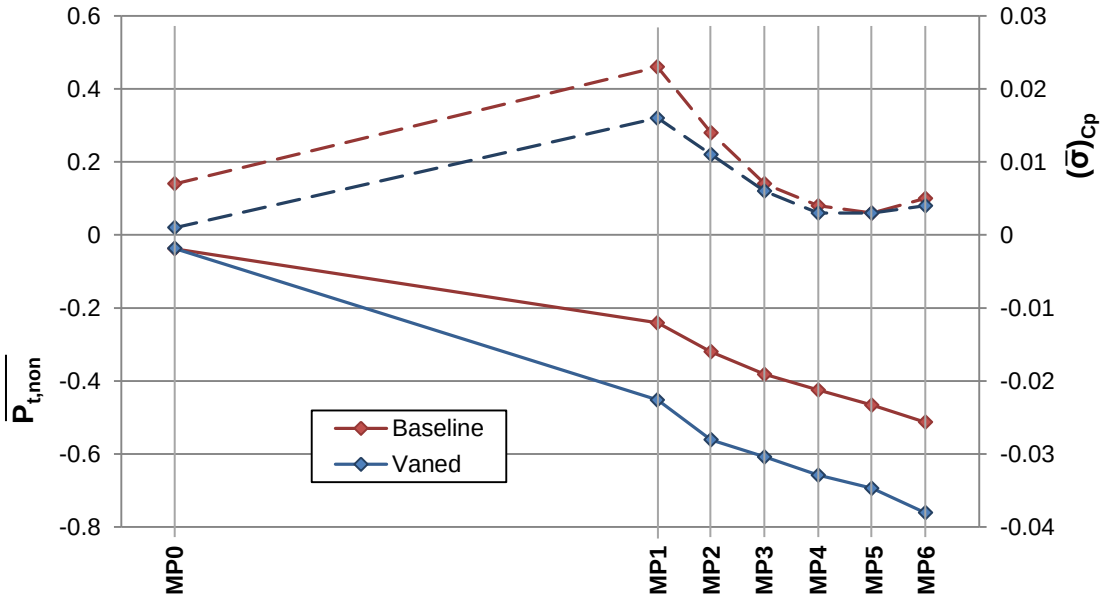

Fig. 3.27 Area-averaged pressure characteristics for both model configurations.

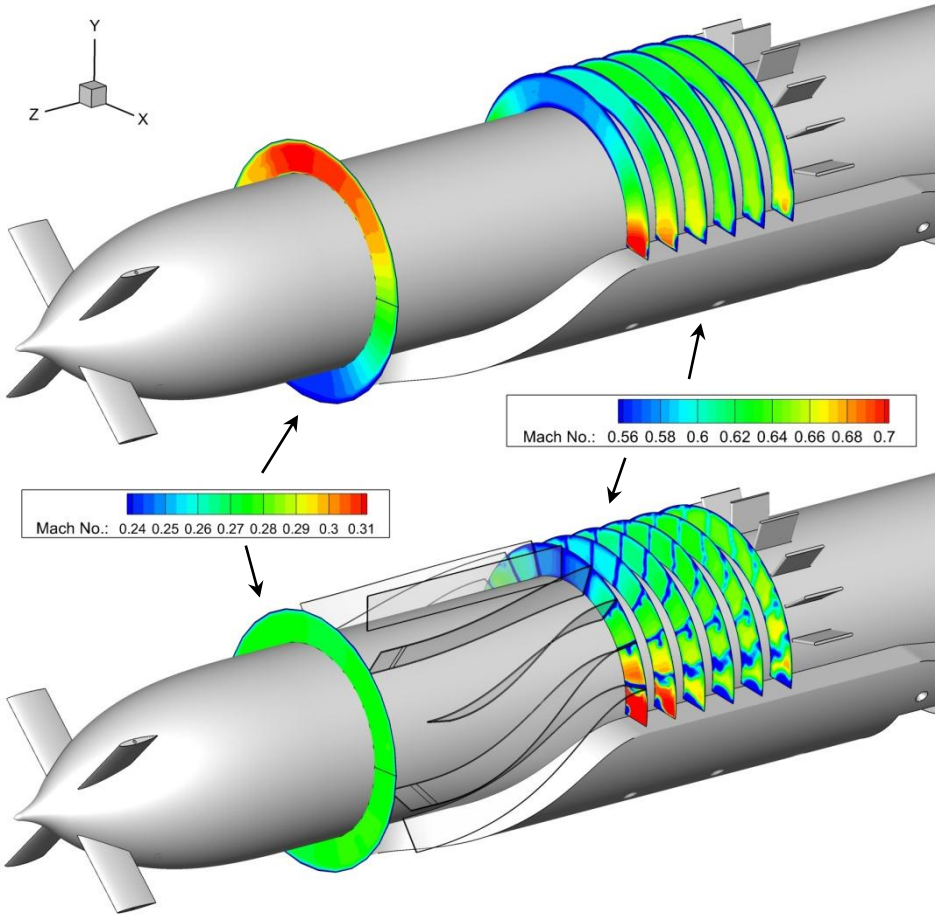

Fig. 3.28 Mach number comparison for both model configurations.

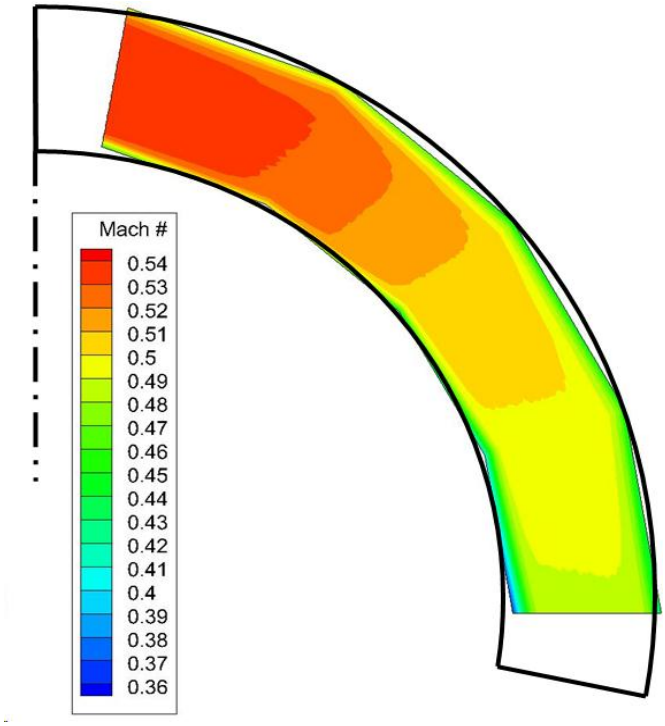

(a)

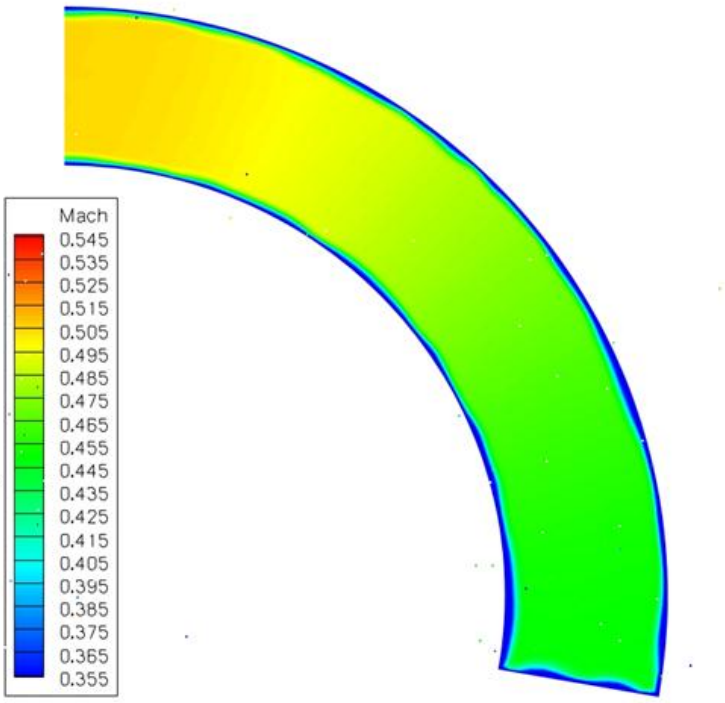

(b)

Fig. 3.29 Mach number contours at MP6 taken from the (a) experimental and (b) computational simulations of the aft bypass geometry.[22,23]

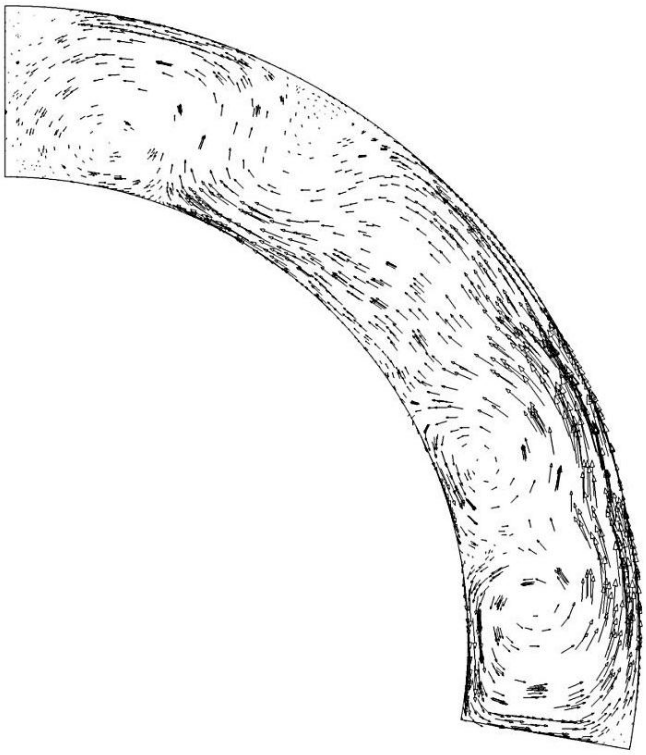

(a)

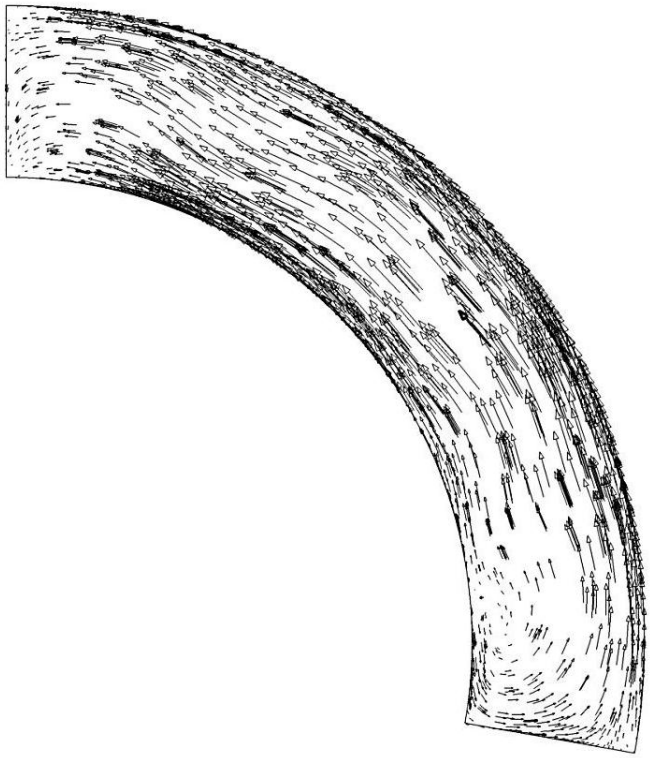

(b)

Fig. 3.30 In-plane velocity vectors taken from a computational simulation of the full engine geometry at (a) MP2 and (b) MP5.[23]

Appendix A

Wind Tunnel Speed Improvements

At the onset of the current study, the existing wind tunnel facility had achieved preliminary data for upstream and downstream Mach number profiles on a previous bypass model design. These data, however, were collected for a preliminary model with flow conditions at approximately half of the true design speed, at which point, the existing axial fan and motor system reached its operational limit. While axial fans are designed primarily for large volume flow rates, they are also limited in the pressure they can recover across each fan stage. As seen in many fan/compressor systems, in order for axial fans to achieve large pressure recoveries, they are typically arranged in series. This compounds the capabilities for each of the fans so the entire system can provide the needed pressure recovery throughout the fluid system. This section will detail the fan replacement process and describe the measures taken to increase the speed of the tunnel to the proposed design condition for the modified bypass model.

A.1 Existing Capabilities

For the existing model, which incorporated a 110-degree gearbox blockage with no guide vane system, the maximum Mach numbers achieved at the inlet plane were approximately 0.17. At the axial location for this measurement, the flow had already been diverted to a full, 360-degree annulus, similar to the upstream measurement plane in the modified model. Based upon the proposed design from GAC, the flow speed at this location was intended to be near Mach 0.40, requiring a 120-percent increase in speed capability. The speed-limiting factor of the original wind tunnel was the axial fan/motor system, which was operating at full speed for these initial tests.

In order to fully examine the performance of the fan/motor system, the United Sensor Corp. pitot-static probe was inserted approximately one foot upstream of the fan

inlet plane, with the aim of measuring the local static and total pressures through a range of fan speeds. As a standard for determining fan performance of a given fluid system, a relationship can be found between the volumetric flow rate and the pressure recovery capabilities of the fan; this is called a fan system curve. In order to determine the fan pressure recovery, a differential total pressure was measured with the probe at the fan inlet with respect to the ambient stagnation pressure in the lab. This value represented the pressure recovered by the fan to return the flow to ambient stagnation conditions. In addition to the pressure recovery, the volume flow rate was calculated using the centerline velocity, measured by static and total pressures from the pitot-static probe, in conjunction with the cross-sectional area of the fan inlet duct. Then, with the corresponding pressure recovery and flow rate data collected at various fan speeds, a system curve could be formulated for the wind tunnel with the original bypass model installed.

Using the appropriate pressure and volume flow rate data measured upstream of the axial fan, and recognizing that pressure losses through any system tend to increase with the square of velocity, the total pressure losses through the wind tunnel were extrapolated to the desired flow rate of approximately 7700 cfm. The measured system curve and extrapolated system curve are shown in Fig. A.1. By fitting a curve though the measured data, the pressure losses through the system were estimated at approximately 1.90 psi, with the tunnel operating at the intended design flow rate. This extrapolated curve was then used to select a new fan system that would be capable of achieving the proposed operating point.

A.2 Blower Selection

As mentioned previously, axial fan systems are primarily intended to provide high flow rate capabilities with relatively low pressure recovery. However, with the large losses expected from the bypass model, primarily from the separation region behind the gearbox blockage, alternative designs were explored further, including multi-stage axial fans and centrifugal-type blowers. Based upon the power available in ARL, however, a multi-stage system was not feasible due to the requirement of having several high-power motors running simultaneously. Therefore, focus was placed on centrifugal-type blowers, which are designed for lower flow rates and significantly higher pressure recovery than their axial

counterparts. Fig. A.2 provides a general comparison of the operating regions for centrifugal blowers and axial fans. The regions shown in the figure do not represent a specific fan or blower and are only intended to present the difference between the two types of systems.

Using the limited amount of data taken from the axial fan configuration, the extrapolated data were used to select a sufficiently-sized blower/motor system. In order to account for the modified model design, with a 160-degree blockage, the system curve was increased by 15 percent with the intent of accounting for increased pressure losses due to the larger separation region aft of the gearbox. Therefore, the blower was required to provide nearly 7700 cfm of air flow, with pressure recovery capabilities of approximately 2.20 psi.

Because blower performance is based upon several factors (volume flow rate, inlet pressure, motor power capabilities, etc.), the selection process was not a simple matter. For instance, the pressure recovery performance of a blower depends upon the suction pressure at its inlet. With the blower located downstream of the acquired losses, the blower inlet pressure depends heavily upon the air speed of the tunnel, or in other words, the volume flow rate. Also, while a blower can run at a range of speeds, the maximum power capability of the motor varies with its loading ratio. For example, if a motor is rated at 150 hp for 3000 rpm, the maximum power available at 1500 rpm is only 75 hp. Due to these various interdependencies, the selection of a blower could only be achieved after several iterations.

Using the target design parameters, a blower/motor system was eventually selected through the Cincinnati Fan Company that provided pressure recovery and flow rate capabilities near those estimated for the bypass system. More specifically, the direct drive system was capable of operating at a maximum rpm of 4000 at 125 hp, while providing pressure recovery near 2.50 psi and supplying nearly 8,000 cfm of air flow. Additionally, in contrast to the existing axial fan, which exhausted along the same axis of the rest of the tunnel, the centrifugal blower was designed to exhaust vertically into the high-bay area. With the diffuser ducting in place, the exit velocities of the exhaust were expected to be reasonably low, allowing for the flow to be safely directed toward the ceiling.

Because this blower/motor system was chosen specifically for this wind tunnel configuration, the flexibility of using the same system with a future experiment is very limited. Any system utilizing the same blower/motor combination would require relatively low flow rates and high pressure losses throughout the tunnel. Options for such investigations might include highly-blocked or three-dimensional, internal flows with low cross-sectional areas.

A.3 Installation and Validation

In order to allow ample space for the new blower/motor system, the existing tunnel diffuser sections were disconnected from the axial fan. Once a suitable location was found, the blower/motor system was mounted on the steel support frame with the assistance of six spring vibration isolation mounts, with the new tunnel centerline near that of the original wind tunnel. Fig. A.3 shows the new blower mounted in ARL with respect to the existing axial fan. (Refer to Fig. 2.1 for a CAD model of the entire wind tunnel facility.) The new tunnel sections were then arranged as required to couple the blower with the test section and to allow for proper flow deceleration at the blower exhaust. With all the required electrical connections made, the blower was first run at low speeds and slowly ramped up to full speed in order to check for any mechanical irregularities or vibrational issues that could have arisen.

After the initial check for operability, which produced positive results, the existing bypass model was assembled and inserted into the test section and a pitot-static probe was placed directly upstream of the blower inlet. This measurement was again used to determine the total losses through the system, in order to relate the volume flow rate with the total pressure losses and to formulate a true system curve up to the intended design speed.

As seen in Fig. A.4, the actual system required higher pressure recovery than the estimated system curve with the additional 15% buffer. The source of this discrepancy was most likely due to one or more of three factors: (1) limited data available from the axial fan system curve, which would have magnified errors through quadratic extrapolation, (2) volume flow rate measurements calculated using a single speed measurement at the center

of the cylindrical flow region, or (3) compressibility effects within the high-speed portions of the bypass model.

Nevertheless, while the actual operating point was very near the estimated operating point, the increase in pressure recovery requirements limited the capability of the blower and resulted in a slower flow than the desired design condition. By measuring the inlet flow of the annular bypass region with a pitot-static probe, the core annular flow reached an average speed of approximately Mach 0.35. While this was not the Mach 0.40 flow designed for this location within the test region, the two-fold increase in tunnel speed was a significant improvement from the values obtained with the axial fan.

Tests were run with the existing model in order to validate the previous results from the off-design experiment. Flow measurements at both the upstream and downstream measurement planes exhibited similar characteristics as the previous low-speed case, as evidenced by the upstream Mach number profiles in Fig. A.5. Note the change in scales between the two contours, as the Mach number values nearly doubled for the updated blower configuration.

A.4 New Tunnel Capabilities

Because the aim of the current study was to focus on the modified bypass design, with 160 degrees of blockage, the new model was installed in the wind tunnel for a simple speed investigation. Two factors were initially considered before testing the modified model design. First, because the diameter of the centerbody decreased, the intended volume flow rate would increase in order to maintain equivalent speed capabilities. Second, with the truncated design of the gearbox fairing, the size of the separation region aft of the blockage was expected to increase; therefore, the overall pressure losses through the system were expected to increase as well. Both of these factors were expected to contribute negatively to the speed capability of the tunnel, since the centrifugal blower design could be limited by both flow rate and pressure recovery. Note, however, that with the new bypass model, the goal for a design speed had been modified such that the Mach number within the constant-area blocked section was now the driving factor in the design. With this change, the flow speed in this region was designed to be Mach 0.70; therefore,

using the isentropic relations for a quasi-one-dimensional flow yielded a new goal for the average inlet speed at Mach 0.31.

Considering this decrease in inlet design speed, measurements were again taken at the upstream measurement plane in order to compare the maximum inlet speed of the modified bypass model with that of the existing model and the updated design goal. Using the pitot-static probe, the maximum flow speed at the upstream measurement plane was found to be Mach 0.29, near the top center location within the annulus. Recognizing that the airspeed varied azimuthally at this axial location, the average speed was expected to be somewhat lower than this single measured value. In order to increase the tunnel speed to a value closer to the intended design speed, a reduction in total pressure losses from the bypass model was required to improve the volume flow rate capabilities of the facility.

Because the modified model incorporated a truncated gearbox design, the region assumed to produce the majority of the pressure losses was the recirculation region within the base flow region. In order to reduce the losses in this portion of the tunnel, the azimuthal extent of the flow separation required a reduction from the full 160-degree blockage. Therefore, with the assistance of an undergraduate student, a supplemental study was completed that tested three separate boat-tail fairing designs, with various diffusing angles.[30] Using two-dimensional diffuser theory, three angles were chosen: one with a standard, 3.5-degree half-angle and two others with half-angles of 7 and 10 degrees. Due to axial space limitations within the tunnel, the three fairings were each 6.25 inches in length. Therefore, assuming all three fairings performed efficiently, the 10-degree fairing would reduce the size of the separation region more than the other two designs. In fact, the 10-degree fairing would reduce the size of the base flow from 160 degrees to approximately 133 degrees if the flow remained fully-attached along the length of the fairing. Fig. A.6 shows the geometry and orientation of the boat-tail fairing with respect to the other gearbox components.

Once installed in the tunnel, an azimuthal total pressure survey was taken for each of the fairings at the mid-radial location in the flow annulus. Using these data, the size of the recirculation region was measured and an approximation of total pressure recovery was also gathered. Fig. A.7 provides an illustration of the differential total pressures around the circumference of the test region, measured with respect to the ambient lab pressure. This

figure presents data within half of the test region, since the behavior is nearly symmetric about the vertical mid-plane. Note that an azimuthal location of 0 degrees represents the top center location of the flow region and the ±180-degree location is positioned within the base flow of the truncated fairing. Data from Fig. A.7 indicated improved flow attachment for the more aggressive fairing designs, along with an overall reduction in total pressure losses within the recirculation region aft of the fairing. In addition to the total pressure profiles collected at this plane, the bypass inlet Mach number was also recorded for each of the fairings within the upstream measurement plane. While running the tunnel near its maximum speed, the maximum inlet Mach numbers achieved were 0.30, 0.31, and 0.32 for the 3.5, 7, and 10-degree fairings, respectively.

From the total pressure and Mach number data, the 10-degree fairing was shown to most effectively diffuse the flow and reduce the total pressure losses aft of the gearbox fairing. In fact, when compared to the case without a boat-tail fairing, the 10-degree fairing decreased the azimuthal extent of the separation region by approximately 20 degrees (10 degrees on each side of the model), provided a 25-percent reduction in total pressure losses in the base flow region, and enabled an 8-percent increase in the maximum inlet Mach number. Therefore, this fairing was used for all remaining bypass tests, in both the baseline and vaned model configurations.

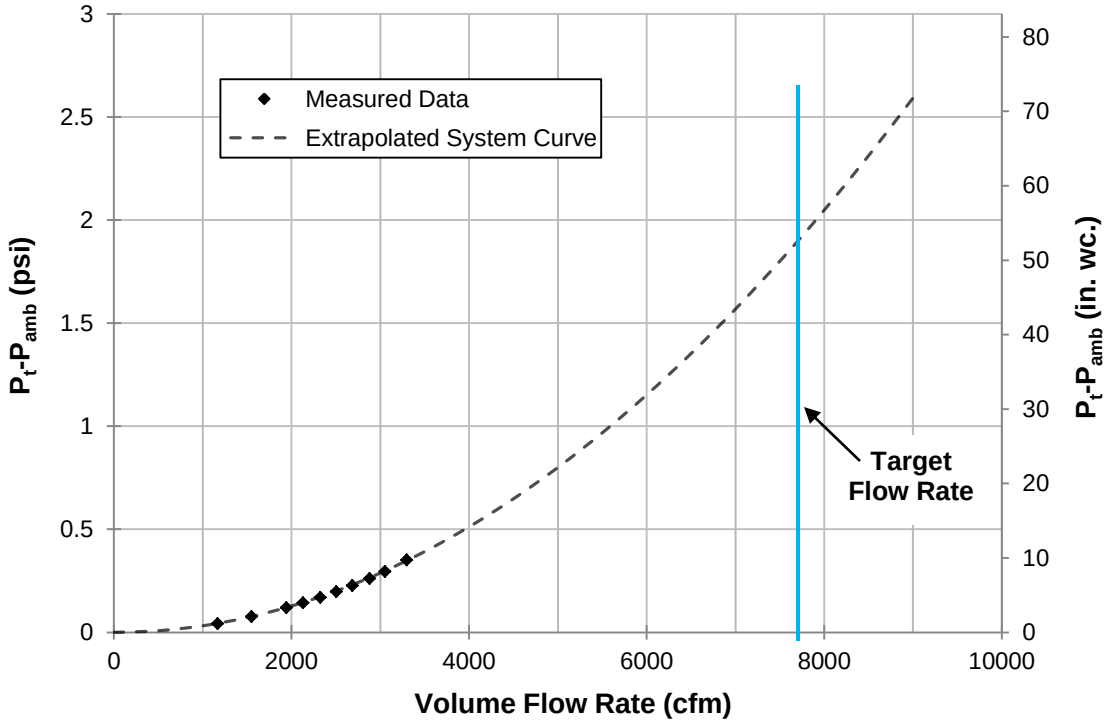

Fig. A.1 System curve for the original bypass model.

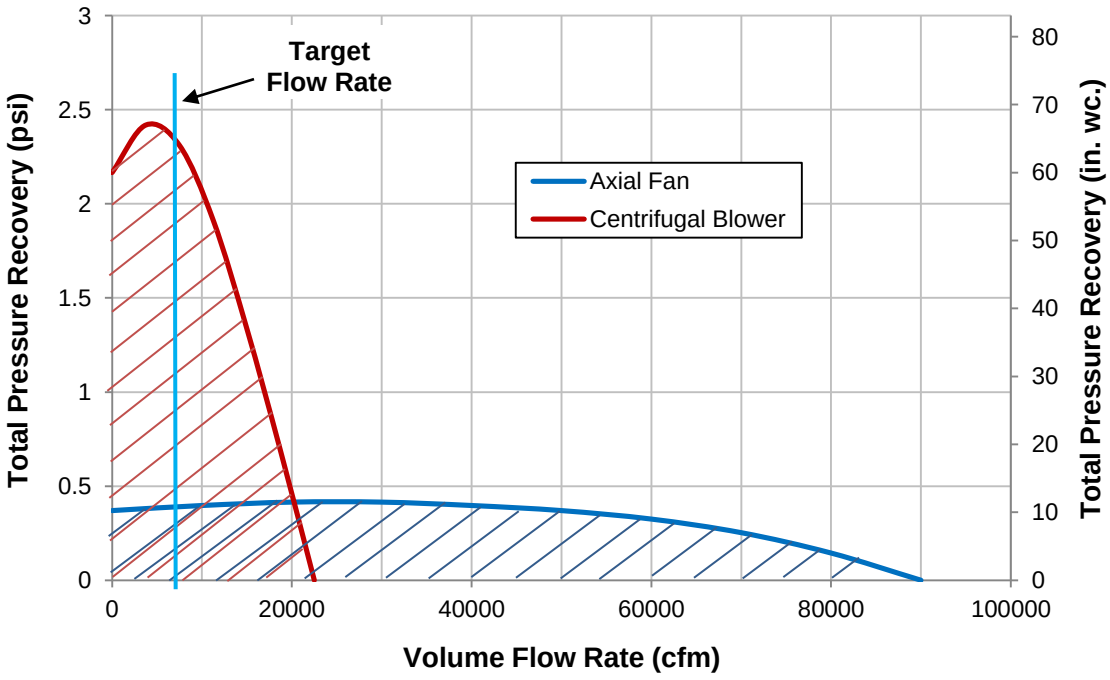

Fig. A.2 Typical fan/blower operating regions.

Fig. A.3 Centrifugal blower installed in the Aerodynamics Research Lab.

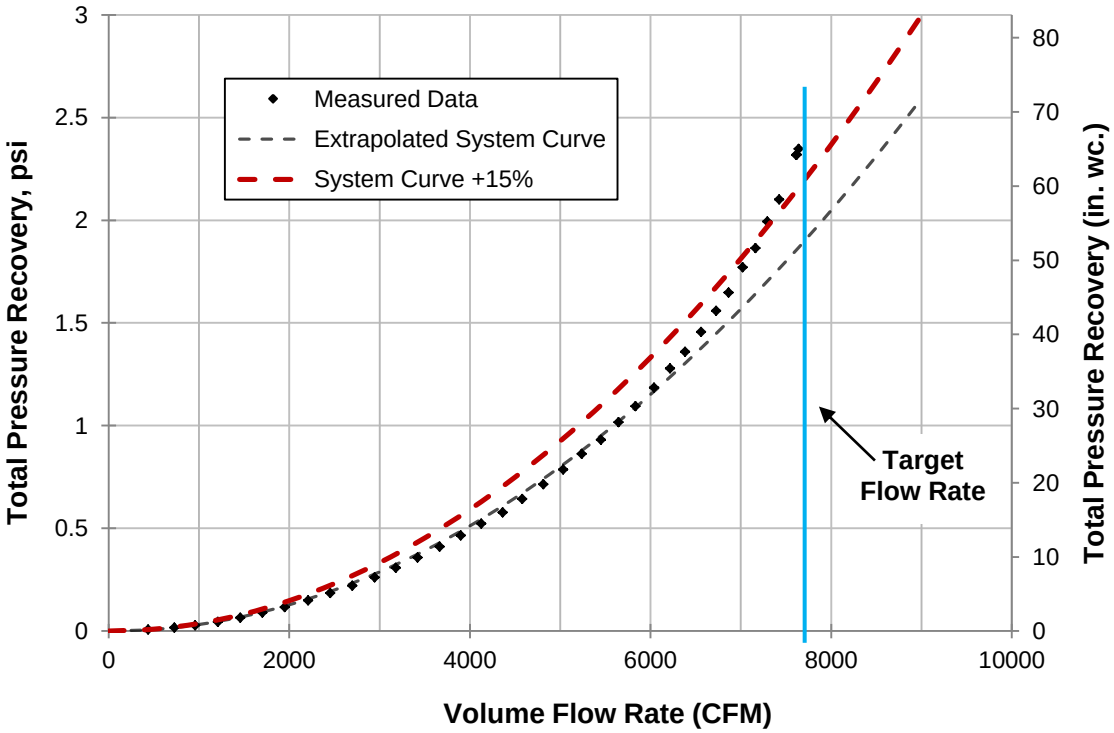

Fig. A.4 Actual system curve for the existing bypass model.

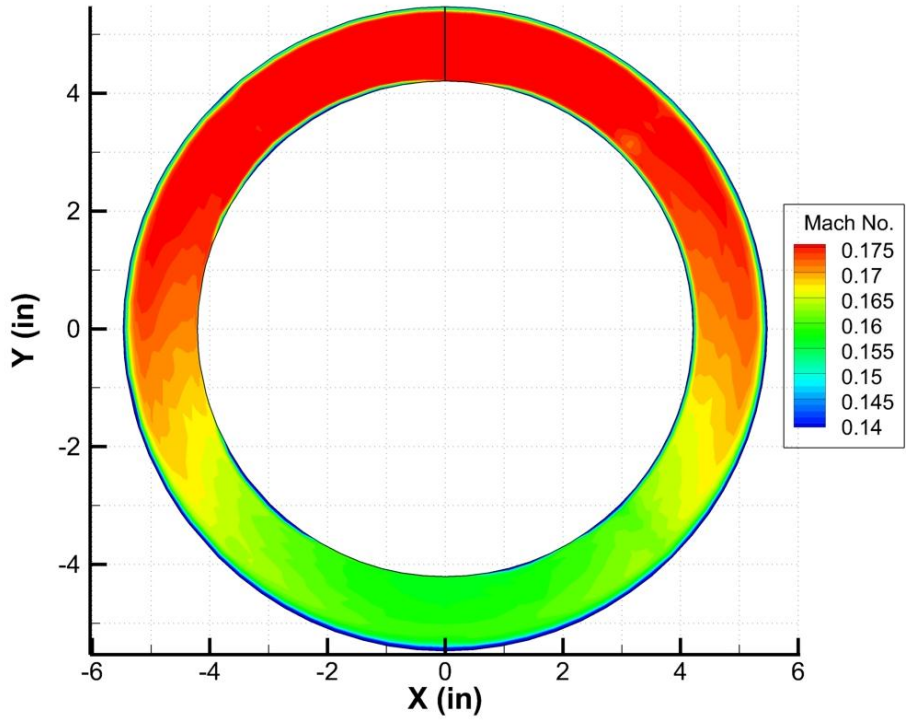

(a)

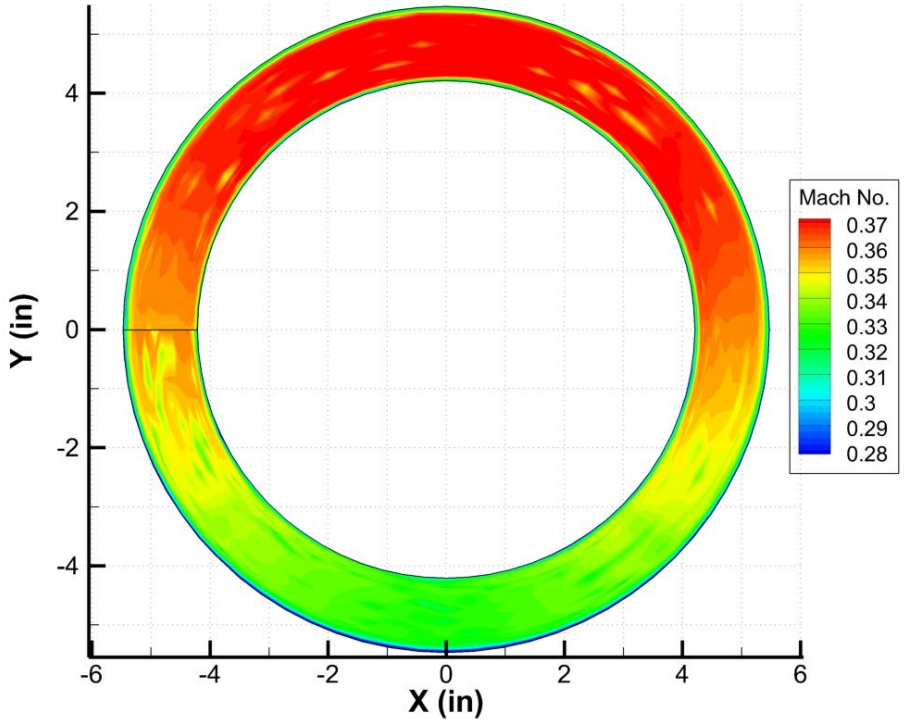

(b)

Fig. A.5 Inlet Mach number contours for the original model with the (a) axial fan and (b) centrifugal blower. (Note the change in scales.)

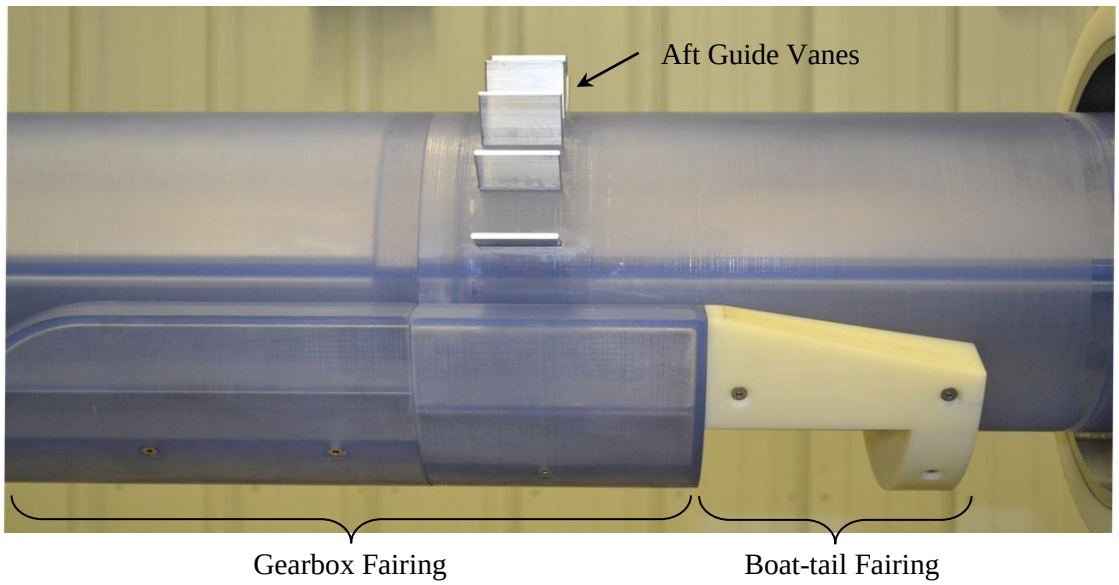

Fig. A.6 Ten-degree boat-tail fairing aft of the gearbox blockage components.

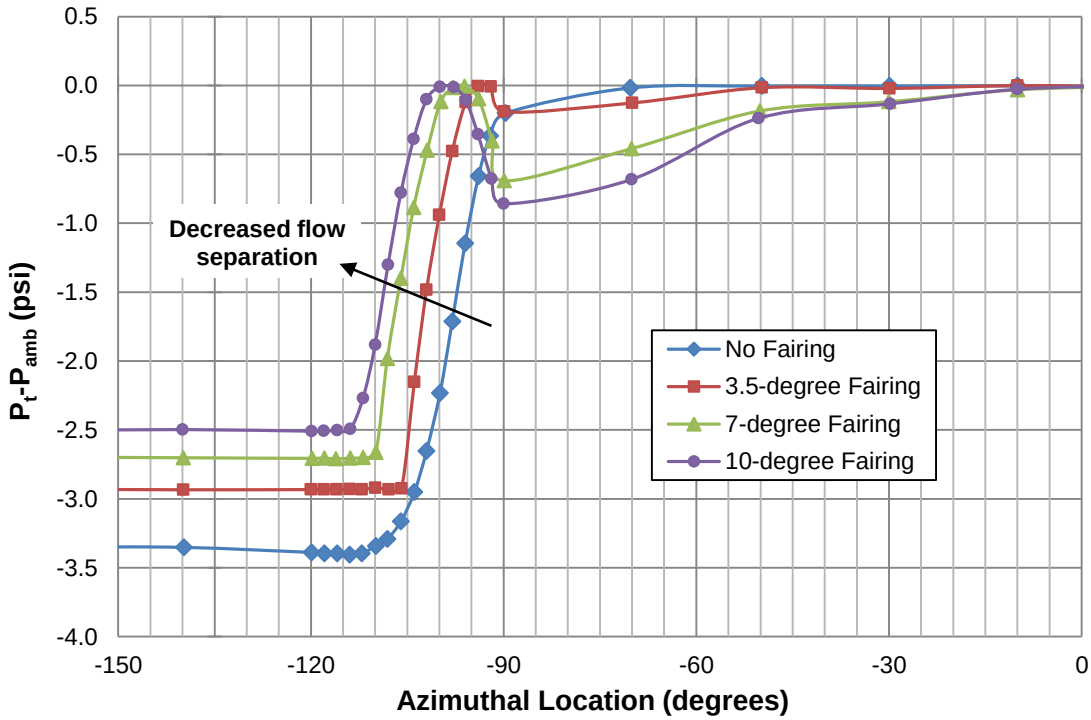

Fig. A.7 Total pressure profiles aft of the boat-tail fairing components.

Appendix B

Five-Hole Probe Calibration

While surveying total pressure profiles within the test section provided a sufficient gauge of flow speed and potential pressure losses, the single total pressure, chamfered-tip probe geometry could not provide flow direction information within the annular bypass region. In order to determine the magnitude and direction of any non-axial flow, a multi-directional pressure probe was calibrated and inserted at the various measurement ports along the test section. The probe used in this study utilized five pressure ports arranged on a conical tip. Using relationships between the pressures measured at each port, the five-hole probe was capable of determining flow speed and direction within the flow.

For the previous, low-speed bypass study, the five-hole probe was calibrated for Mach 0.20 freestream flow. For the current application, the probe required calibration for a more representative range of speeds encountered within the bypass region. Therefore, using a separate wind tunnel facility, the five-hole probe was calibrated for use in the bypass flow.

B.1 Theory of Operation

In order to characterize highly-complex flowfields, a variety of multi-directional pressure probes have been introduced that measure local flow directionality characteristics. For example, three pressure readings from a spherical tip can use known pressure coefficient data from a sphere to determine flow direction within a single plane. In order to collect three-dimensional flow direction measurements, five-hole and seven-hole probes use a center pressure port and four or six ports distributed on the probe tip to determine the flow direction, based upon relationships between the separate and distinct pressure readings. For the United Sensor Corp. five-hole probe used in this study, two holes were located above and below the central port and two holes were located to the left and right of

the central port. This configuration allowed for predictions of yaw and pitch angles with respect to the axial orientation of the probe. Schematics of the angular orientation of the probe as well as the port numbering scheme are shown in Fig. B.1. In order to provide an accurate representation of an unknown flowfield, the five-hole probe required calibration in a uniform flow of known speed and direction. Using several calibrations at different speeds and a range of flow angles, an overall calibration could then be used to determine unknown flow characteristics.

After several calibration procedures were analyzed, a high-order multiple regression model, similar to that used in Gonsalez and Arrington, was utilized for the current study.[31] This specific method utilized three independent coefficients to predict four dependent variables related to flow speed and direction (total pressure, static pressure, and pitch and yaw angles). The pressure coefficients, C_α and C_β, are defined below, and provided information on the probe's sensitivity to pitch and yaw, respectively.

$$C_\alpha = \frac{P_4 - P_5}{P_1 - \overline{P}_{2-5}} \tag{B.1}$$

$$C_\beta = \frac{P_3 - P_2}{P_1 - \overline{P}_{2-5}} \tag{B.2}$$

(In these and all following equations, $\overline{P}_{2\text{-}5}$ is defined as the average of the pressures measured in ports 2 through 5.) The third variable used in this calibration method was a compressibility coefficient, C_M, which provided information with regard to flow speed. Since variations in the two pressure coefficients were not significant between differing flow speeds, this additional variable was needed to improve the accuracy of the speed predictions.

$$C_M = \frac{P_1 - \overline{P}_{2-5}}{P_1} \tag{B.3}$$

After some post-calibration investigation, the accuracy of the calibration was further improved by using a third pressure coefficient, known here as $C_{\alpha\beta}$. Instead of relating two opposite pressure readings, this third pressure coefficient utilized data collected at two adjacent ports in an attempt to better correlate the data when the probe was at high angles of yaw and pitch simultaneously.

$$C_{\alpha\beta} = \frac{P_4 - P_3}{P_1 - \overline{P}_{2-5}} \tag{B.4}$$

While this definition of $C_{\alpha\beta}$ was not developed or utilized by Gonsalez and Arrington, the addition of a supplemental pressure coefficient facilitated a substantial improvement in prediction accuracy once the calibration data were fully processed.

Using the multiple regression model, the three pressure coefficients and the compressibility coefficient were correlated through a high-order polynomial in order to explicitly determine pitch and yaw angles (α and β) and total and static pressure coefficients (C_o and C_q), which are defined later. Shown below in Eqs. B.5 through B.7 are the fourth-order relationships used to determine these flow variables. (Note that subsequent equations have been abridged for conciseness.)

$$\begin{aligned}\alpha = {} & K_{0_\alpha} + K_{1_\alpha} C_\alpha + K_{2_\alpha} C_\beta + K_{3_\alpha} C_{\alpha\beta} + K_{4_\alpha} {C_\alpha}^2 + K_{5_\alpha} C_\alpha C_\beta + K_{6_\alpha} C_\alpha C_{\alpha\beta} \\ & + K_{7_\alpha} {C_\beta}^2 + K_{8_\alpha} C_\beta C_{\alpha\beta} + K_{9_\alpha} {C_{\alpha\beta}}^2 + K_{10_\alpha} {C_\alpha}^3 + K_{11_\alpha} {C_\alpha}^2 C_\beta \\ & + K_{12_\alpha} {C_\alpha}^2 C_{\alpha\beta} + K_{13_\alpha} C_\alpha {C_\beta}^2 + K_{14_\alpha} C_\alpha C_\beta C_{\alpha\beta} + K_{15_\alpha} C_\alpha {C_{\alpha\beta}}^2 \\ & + K_{16_\alpha} {C_\beta}^3 + K_{17_\alpha} {C_\beta}^2 C_{\alpha\beta} + K_{18_\alpha} C_\beta {C_{\alpha\beta}}^2 + K_{19_\alpha} {C_{\alpha\beta}}^3 + K_{20_\alpha} {C_\alpha}^4 \\ & + K_{21_\alpha} {C_\alpha}^3 C_\beta + K_{22_\alpha} {C_\alpha}^3 C_{\alpha\beta} + K_{23_\alpha} {C_\alpha}^2 {C_\beta}^2 + K_{24_\alpha} {C_\alpha}^2 C_\beta C_{\alpha\beta} \\ & + K_{25_\alpha} {C_\alpha}^2 {C_{\alpha\beta}}^2 + K_{26_\alpha} C_\alpha {C_\beta}^3 + K_{27_\alpha} C_\alpha {C_\beta}^2 C_{\alpha\beta} + K_{28_\alpha} C_\alpha C_\beta {C_{\alpha\beta}}^2 \\ & + K_{29_\alpha} C_\alpha {C_{\alpha\beta}}^3 + K_{30_\alpha} {C_\beta}^4 + K_{31_\alpha} {C_\beta}^3 C_{\alpha\beta} + K_{32_\alpha} {C_\beta}^2 {C_{\alpha\beta}}^2 \\ & + K_{33_\alpha} C_\beta {C_{\alpha\beta}}^3 + K_{34_\alpha} {C_{\alpha\beta}}^4 + K_{35_\alpha} C_M + K_{36_\alpha} {C_M}^2 + K_{37_\alpha} {C_M}^3\end{aligned} \tag{B.5}$$

$$\beta = K_{0_\beta} C_\alpha + K_{1_\beta} C_\beta + K_{2_\beta} C_{\alpha\beta} + K_{3_\beta} {C_\alpha}^2 + \ \ldots \ + K_{36_\beta} {C_M}^2 + K_{37_\beta} {C_M}^3 \tag{B.6}$$

$$C_o = K_{0_{C_o}} C_\alpha + K_{1_{C_o}} C_\beta + K_{2_{C_o}} C_{\alpha\beta} + K_{3_{C_o}} {C_\alpha}^2 + \ \ldots \ + K_{36_{C_o}} {C_M}^2 + K_{37_{C_o}} {C_M}^3 \tag{B.7}$$

$$C_q = K_{0_{C_q}} C_\alpha + K_{1_{C_q}} C_\beta + K_{2_{C_q}} C_{\alpha\beta} + K_{3_{C_q}} {C_\alpha}^2 + \ \ldots \ + K_{36_{C_q}} {C_M}^2 + K_{37_{C_q}} {C_M}^3 \tag{B.8}$$

After some analysis, the polynomials depicted above seemed to produce very reliable and accurate predictions of both flow angle and flow speed. Although they contained 38 distinct terms, the accuracy of the predictions was deemed a higher priority than computational efficiency.

In order to determine flow speed from the multiple regression model, two additional variables were used to calculate total and static pressure in the flow and are defined as shown below.

$$C_o = \frac{P_1 - P_t}{P_1 - \overline{P}_{2-5}} \tag{B.9}$$

$$C_q = \frac{P_1 - \overline{P}_{2-5}}{P_t - P_s} \tag{B.10}$$

As seen here, these total and static pressure coefficients utilized relationships between the five-hole probe pressures and the local total and static pressures, and were, therefore, not determined explicitly from the multiple regression model. Instead, the coefficients were determined through the regression model and the values of total and static pressure were found implicitly through them.

Equation B.11 summarizes Eqs. B.5 through B.8 in simple matrix form. Here, matrix [A] represents the flow variables (α, β, C_o, and C_q), matrix [C] represents the fourth-order arrangement of the pressure and compressibility coefficients (C_α, C_β,…, $C_M{}^3$), and matrix [K] represents the calibration constants (e.g. $K_{0,\alpha}$, $K_{1,\alpha}$,…, $K_{37,\alpha}$).

$$[A] = [C][K] \tag{B.11}$$

In order to produce a representative matrix of calibration constants, a full calibration was required in which all flow variables were known (e.g. pitch and yaw angles and total and static pressures). By collecting pressure data at a variety of flow conditions, the calibration constants could be established using Eq. B.11. Then, once [K] was known, the same equation could be used with five-hole probe pressure data to predict the speed and direction of an unknown flowfield.

B.2 Experimental Setup

Because the flow features within the constant-area blocked section of the bypass model were of the most interest in the current study, the five-hole probe required calibration for flow speeds that would be representative of this region. Using flow speed data collected with the total pressure probe, the flow Mach numbers in this region were expected to range between 0.55 and 0.75. Therefore, the five-hole probe required a calibration in a wind tunnel facility capable of operating at several speeds within this range.

The facility chosen for the probe calibration was a 1-inch diameter jet within an anechoic chamber (see Fig. B.2). The open jet flow was supplied by a set of compressed air tanks and was commonly run at speeds exceeding Mach 0.90. For the calibration tests, the jet was expected to provide flows near and below Mach 0.70 in a nearly continuous manner. In order to determine the speed of the jet flow, a single total pressure measurement was monitored at a location upstream of the jet exit plane. Using this total pressure data, in conjunction with the ambient static pressure within the chamber, a real-time approximation of the jet speed could be determined through isentropic flow relations. Additional details of the jet facility can be found in Fontaine.[32]

In order to calibrate the five-hole probe, a device was fabricated to allow horizontal and vertical rotation of the probe, while also keeping the probe tip at a fixed location. Because flow quality and behavior was expected to vary across the jet diameter, keeping the tip of the probe in a fixed position allowed for consistent measurements at all angles of pitch and yaw. Therefore, the probe mounting device consisted of two rotation stages, which permitted motion about the vertical and horizontal axes, as shown in Fig. B.3. Using this calibration setup, the probe tip was positioned at the center of the jet and 2 inches (two probe diameters) downstream of the jet exit plane. At this location, the core flow was expected to maintain a sufficient diameter to ensure the probe tip was located within the high-speed core at all times throughout a given test. Fig. B.4 illustrates the positioning of the probe with respect to the jet.

To collect the required pressures from the five-hole probe, the polyurethane pressure tubing was connected to a Pressure Systems Inc., model 9016 NetScanner™ pressure transducer. This transducer had a pressure range of ±5 psid, with an accuracy of 0.0025 psi, and required an 80-psi supply of nitrogen to assist in an internal calibration. Using an Ethernet connection, the output of the NetScanner™ was interfaced with a LabVIEW program, allowing the instantaneous pressures measured by the probe to be monitored continuously. Also within the LabVIEW code, the instantaneous upstream jet pressure and ambient static pressure could be collected simultaneously with the probe pressure data in order to properly correlate the measurements with respect to the actual jet flow speed.

B.3 Test Procedure

Using the existing Mach 0.20 calibration, five-hole probe measurements taken within the high-speed bypass region indicated radial flow angles (pitch) of ±3 degrees and azimuthal flow angles (yaw) of ± 10 degrees. Therefore, recognizing the potential inaccuracies induced by the off-speed calibration, a test grid was developed that included 1-degree increments for pitch angles of ±5 degrees and yaw angles of ±20 degrees and 2-degree increments for yaw angles between ±20 and ±30 degrees. Due to the small radial extent of the bypass annulus, the pitch angles were expected to be small when compared to the azimuthal behavior of the flow. Therefore, this grid pattern was intended to provide sufficient data to accurately represent the expected range of flow angles within the bypass flow.

During a given test, three sets of 30 pressure measurements were collected at each pitch and yaw combination in order to ensure consistency and minimize the influence of outlying data points. Then, after collecting three sets of measurements, the probe was rotated manually to the next orientation angle using the rotation stages. In some cases, based on the capabilities of the air supply tanks and compressor, the speed of the jet flow would fluctuate during a test. Therefore, before each data point was collected, the indicated speed of the jet was adjusted accordingly by either opening or closing the jet supply valve. This data acquisition procedure was completed for a total of three jet speeds, including Mach 0.60, 0.65, and 0.70.

In order to determine the true total and static pressures at the location of the probe tip, a pitot-static probe was mounted in the same location as the five-hole probe. The speed of the jet was then varied near each of the calibration speeds in order to correlate the indicated upstream total pressure and the actual total pressure measured by the probe. In effect, these measurements were taken in order to determine a pressure recovery factor as the air exited the jet. Also, when conducting the primary calibration tests, the speed of the jet was calculated based upon the ambient static pressure within the anechoic chamber, assuming the static pressure did not vary throughout the profile of the jet. With the static pressure measurements from the pitot-static probe, however, the ambient static pressure and the true static pressure within the core flow were expected to vary slightly.

B.4 Calibration Results

Using pressure data collected with the pitot-static probe, the actual total and static pressures were determined for each of the three calibrations speeds. Shown in Fig. B.5 is the relationship between the upstream jet total pressure and the total and static pressures measured with the probe. Throughout the range of speeds used in the calibration, a consistent total pressure discrepancy of approximately 0.05 percent was found two jet diameters downstream of the jet exit plane, while the static pressures varied by differing amounts at the various jet speeds. Using these adjusted pressure correlations, the actual calibration jet speeds were determined to be Mach 0.606, 0.654, and 0.699, with a variation of approximately ±0.005, which were not far from the intended calibration speeds.

Once accurate total and static pressures were established, the data collected by the five-hole probe were analyzed in order to illustrate the direct effects of non-axial flow on the five pressure readings. Shown in Fig. B.6 is a sample of the data collected at a fixed pitch angle and through a variety of yaw angles. Because the range of pitch angles was small compared to that of yaw angles, the measured pressures had a much larger dependence on probe yaw orientation. Therefore, data have been plotted with respect to the probe yaw angle.

Using data collected for each of the tests, it was apparent that the probe may not have been aligned properly in the probe mounting device. This was found by analyzing the pressure readings for the $\alpha=0$, $\beta=0$ configuration. Assuming the probe was free of defects and aligned directly into the flow, ports 2 through 5 should have indicated equivalent pressure readings. However, this was not the case for the measurements collected during the calibration. Without a fixed reference for the axis of the jet, however, the probe was assumed to be fabricated axisymmetrically and the data for the angular orientation of the probe were adjusted 1.25 degrees in the yaw direction to account for this slight discrepancy in the pressure readings.

With the full set of calibration data, a matrix of calibration constants was found using the procedure described above. Then, in order to determine the accuracy of the calibration, the original known data points were analyzed using only the probe pressure data and the derived calibration constants. Errors in predicted pitch and yaw angle are

illustrated in Fig. B.7a and indicate angular prediction accuracies of ±0.60 degrees in both yaw and pitch. Also shown in Fig. B.7b is the distribution of Mach number errors, which indicate accuracies of ±0.005. (Note that the prediction errors followed a nearly Gaussian distribution, with the quoted accuracy values representing a 95% confidence interval.)

Because these accuracy checks were performed on the data used to create the calibration matrix, this method may have, in fact, indicated less error than would be present in an unknown flowfield. Without additional data, however, the procedure described above was deemed sufficient for a general qualitative analysis of the bypass flow.

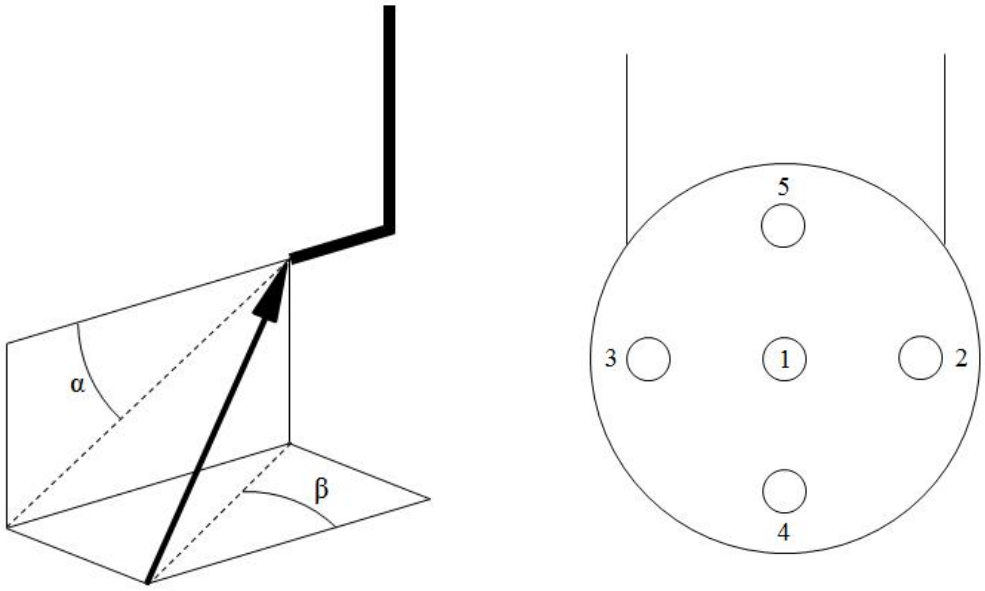

(a) (b)

Fig. B.1 Schematics detailing (a) probe orientation angles and (b) port arrangement.

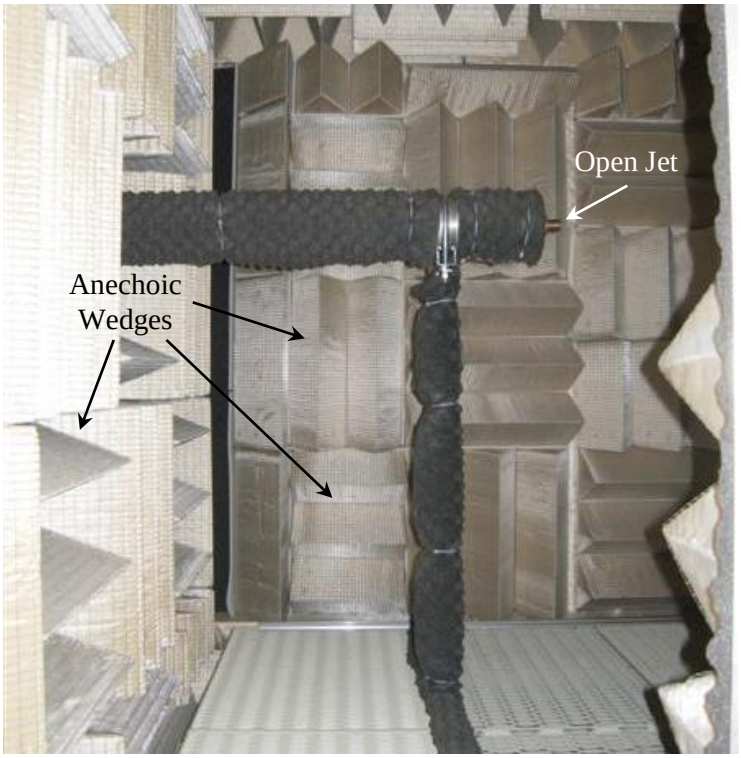

Fig. B.2 Anechoic chamber facility with 1-inch diameter jet flow.

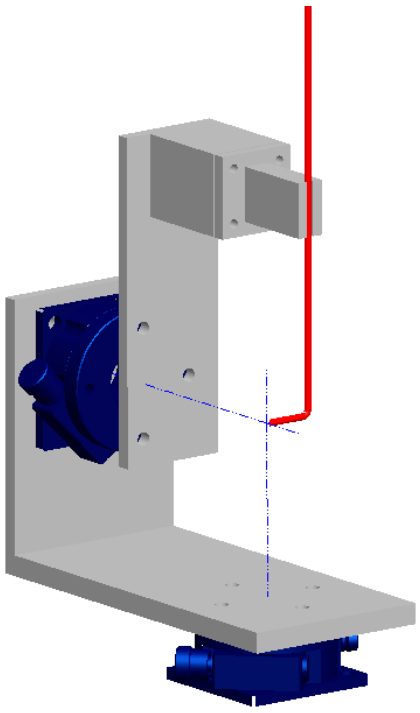

Fig. B.3 Probe calibration setup allowing pitch and yaw rotation.

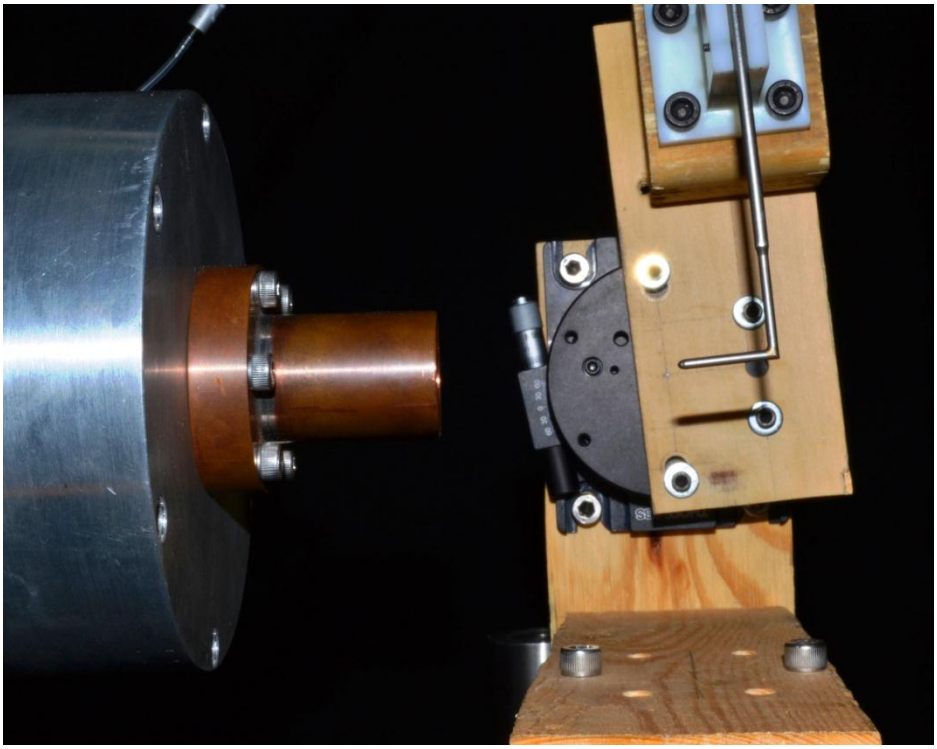

Fig. B.4 Calibration setup mounted in the jet facility.

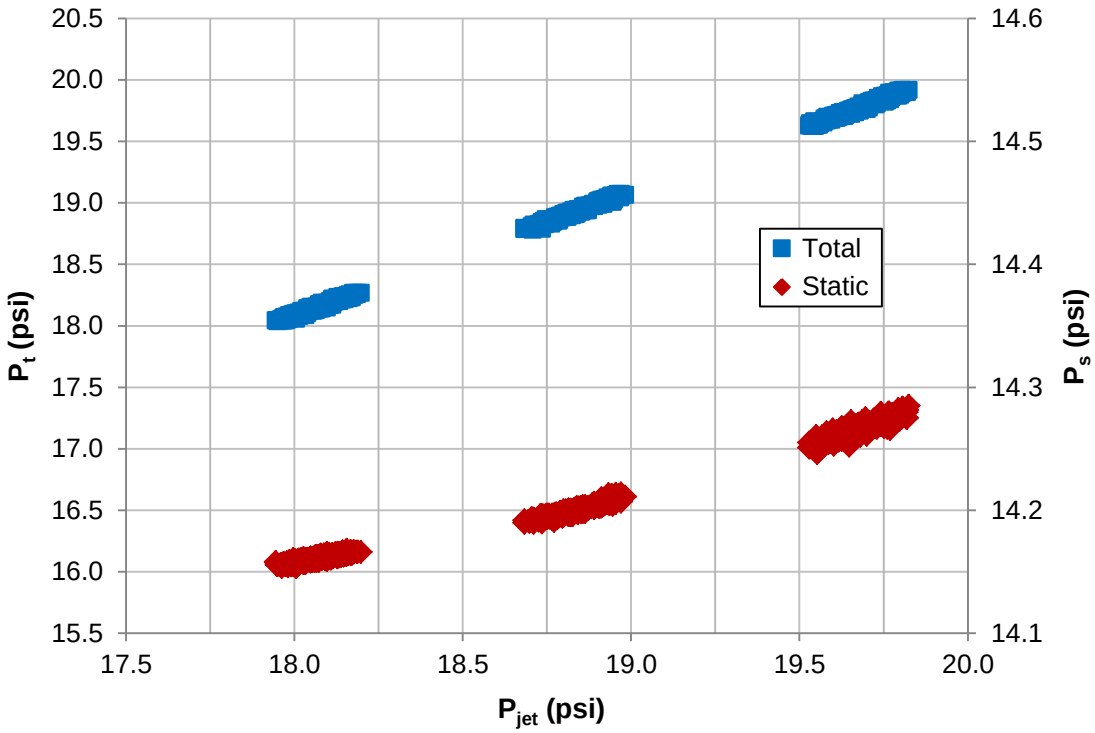

Fig. B.5 Total and static pressures with respect to indicated jet pressure.

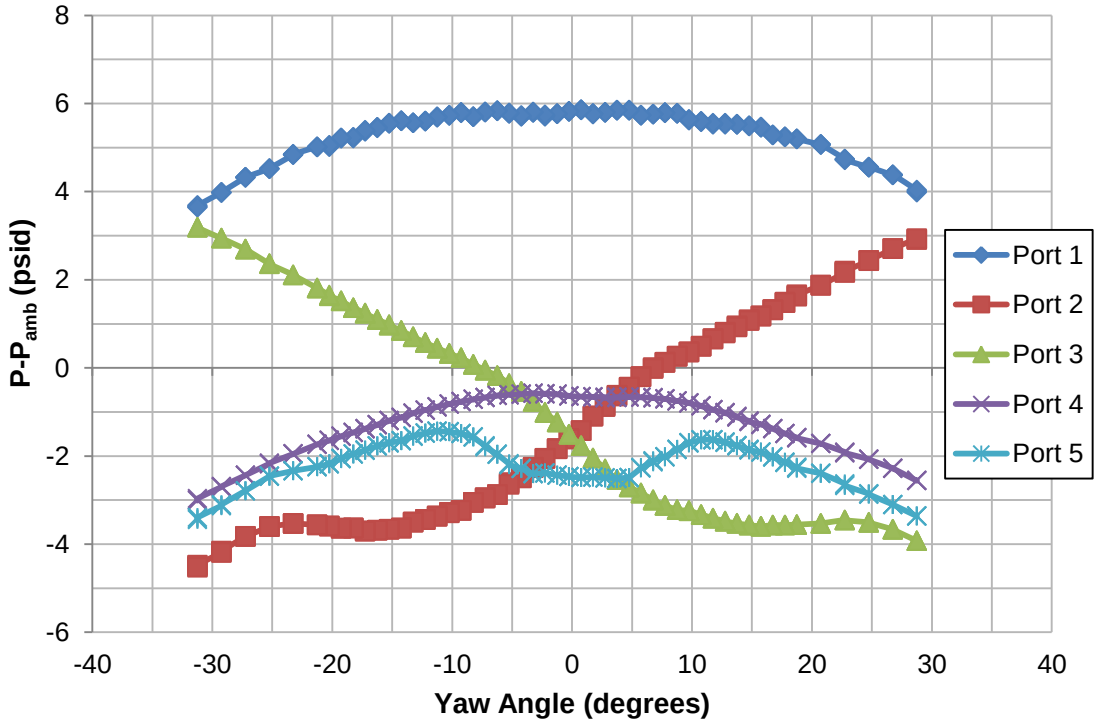

Fig. B.6 Sample calibration data for M=0.70 and α=5 degrees.

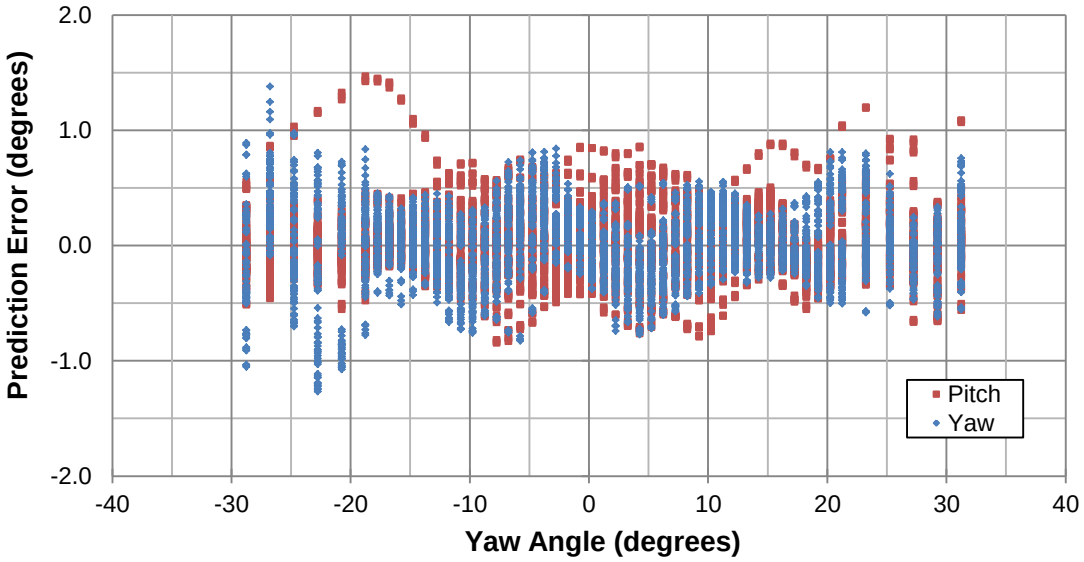

(a)

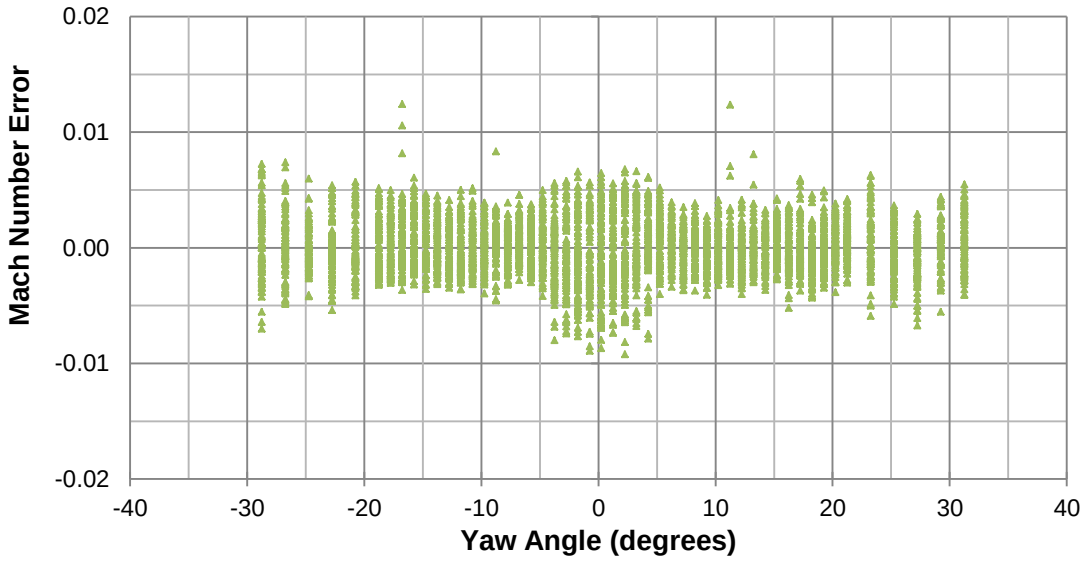

(b)

Fig. B.7 (a) Yaw, pitch, and (b) Mach number errors after probe calibration.

Appendix C

Uncertainty Analysis

In any experimental analysis, there exist errors in measurements collected with experimental devices due to both the precision of the specific device or a bias induced by manufacturing errors or a poor calibration. These errors are propagated through derived variables and may become amplified throughout multiple calculations. The method used to analyze the uncertainties encountered in this study is a very common technique described in detail by Kline and McClintock.[33] This method was formulated based upon the concept of a single-sample experiment, where statistical analysis of multiple measurements is unavailable or unfeasible. This fits well with the present study, where one measurement plane incorporates up to 2600 measurement points.

In general, this method assumes that a derived result, denoted here as R, is a function of several measured and/or derived variables, x_1, x_2,…,x_n. Shown in Equation C.2 is the resulting experimental uncertainty of R, incorporating the errors due to each of the underlying variables, denoted by U_{xi}.

$$R = R(x_1, x_2, \dots, x_n) \tag{C.1}$$

$$U_R = \sqrt{\sum_{i=1}^{n} \left(\frac{\partial R}{\partial x_i} U_{x_i}\right)^2} \tag{C.2}$$

This method will be utilized for each of the variables calculated to describe flow characteristics within the bypass region.

C.1 Ambient Conditions

While the ambient temperature and pressure are not derived variables, they are utilized throughout many of the calculations determining flow characteristics. In fact, they

are used, most directly, to determine the air density for the mass flow calculation in Eq. 2.12. The ambient pressure, read from the Setra absolute pressure transducer, has a measurement uncertainty of 0.008 psi, while the ambient temperature, measured in the lab with a thermocouple, has an uncertainty of 1 degree F. Using these uncertainties, the total uncertainty of the stagnation density is given below, followed by the partial derivatives with respect to the variables of interest.

$$U_{\rho_o} = \sqrt{\left(\frac{\partial \rho_o}{\partial P_{amb}} U_{P_{amb}}\right)^2 + \left(\frac{\partial \rho_o}{\partial T_{amb}} U_{T_{amb}}\right)^2} \tag{C.3}$$

$$\frac{\partial \rho_o}{\partial P_{amb}} = \frac{1}{R T_{amb}} \tag{C.4}$$

$$\frac{\partial \rho_o}{\partial T_{amb}} = -\frac{P_{amb}}{R {T_{amb}}^2} \tag{C.5}$$

C.2 Absolute Pressure

Because the ESP modules collect a differential pressure, the uncertainty in absolute pressure values must account for both the error in the ESP module as well as the ambient pressure reading from the Setra transducer. To simplify pressure error analysis, the uncertainty of absolute pressure values will be used in future calculations, rather than keeping the differential and ambient pressures separate. The measured differential pressure, dP, is defined such that

$$P = dP + P_{amb} \tag{C.6}$$

Errors in differential pressure measurements come from two sources: (1) the precision of the ESP module itself and (2) the calibration procedure through the System 8400. According to the manufacturer, the ±5-psid module uncertainty was 0.05 percent of the full-scale pressure and the calibration uncertainty was an additional 0.02 percent of the full-scale. Therefore, the total uncertainty for pressure measurement with the ±5-psid module was 0.0027 psi.

Due to the simplicity of Equation C.6, the uncertainty calculation can be simplified to a root-sum-square (RSS) formulation, since the two required derivatives are equal to unity.

$$U_P = \sqrt{{U_{dP}}^2 + {U_{P_{amb}}}^2} \tag{C.7}$$

Consequently, the uncertainty of all absolute pressure measurements is 0.0085 psi.

C.3 Tunnel Speed

The tunnel speed was set by the ratio of the static pressure measurements at the upstream measurement plane to the ambient pressure in the lab. Using the two uncertainties, which were found using Eq. C.7 above, the overall uncertainty in the tunnel speed parameter is defined as shown below.

$$U_{\frac{P_\infty}{P_{amb}}} = \sqrt{\left(\frac{\partial \frac{P_\infty}{P_{amb}}}{\partial P_{US1}} U_{P_{US1}}\right)^2 + \cdots + \left(\frac{\partial \frac{P_\infty}{P_{amb}}}{\partial P_{US15}} U_{P_{US15}}\right)^2 + \left(\frac{\partial \frac{P_\infty}{P_{amb}}}{\partial P_{amb}} U_{P_{amb}}\right)^2} \tag{C.8}$$

$$\frac{\partial \frac{P_\infty}{P_{amb}}}{\partial P_{USi}} = \frac{1}{15}\left(\frac{1}{P_{amb}}\right) \tag{C.9}$$

$$\frac{\partial \frac{P_\infty}{P_{amb}}}{\partial P_{amb}} = -\frac{1}{15}(P_{US1} + P_{US2} + \cdots + P_{US15})\left(\frac{1}{{P_{amb}}^2}\right) \tag{C.10}$$

C.4 Static and Total Pressure Coefficients

To determine uncertainties of the pressure coefficients, the uncertainty of the dynamic pressure was determined using the equations below. Note that the uncertainty in Mach number is found in Section C.5.

$$U_{q_\infty} = \sqrt{\left(\frac{\partial q_\infty}{\partial P_\infty} U_{P_\infty}\right)^2 + \left(\frac{\partial q_\infty}{\partial M_\infty} U_{M_\infty}\right)^2} \tag{C.11}$$

$$\frac{\partial q_\infty}{\partial P_\infty} = \frac{\gamma}{2} {M_\infty}^2 \tag{C.12}$$

$$\frac{\partial q_\infty}{\partial M_\infty} = \gamma P_\infty M_\infty \tag{C.13}$$

Then, using the uncertainty in dynamic pressure, the uncertainty of the static pressure coefficients and nondimensionalized total pressures can be found as follows:

$$U_{C_p} = \sqrt{\left(\frac{\partial C_p}{\partial P} U_P\right)^2 + \left(\frac{\partial C_p}{\partial P_\infty} U_{P_\infty}\right)^2 + \left(\frac{\partial C_p}{\partial q_\infty} U_{q_\infty}\right)^2} \tag{C.14}$$

$$\frac{\partial \rho}{\partial P} = \frac{1}{q_\infty} \tag{C.15}$$

$$\frac{\partial \rho}{\partial P_\infty} = -\frac{1}{q_\infty} \tag{C.16}$$

$$\frac{\partial \rho}{\partial q_\infty} = \frac{(P_\infty - P)}{{q_\infty}^2} \tag{C.17}$$

$$U_{P_{t,non}} = \sqrt{\left(\frac{\partial P_{t,non}}{\partial P_t} U_{P_t}\right)^2 + \left(\frac{\partial P_{t,non}}{\partial P_{amb}} U_{P_{amb}}\right)^2 + \left(\frac{\partial P_{t,non}}{\partial q_\infty} U_{q_\infty}\right)^2} \tag{C.18}$$

$$\frac{\partial P_{t,non}}{\partial P_t} = \frac{1}{q_\infty} \tag{C.19}$$

$$\frac{\partial P_{t,non}}{\partial P_{amb}} = -\frac{1}{q_\infty} \tag{C.20}$$

$$\frac{\partial P_{t,non}}{\partial q_\infty} = \frac{(P_{amb} - P_t)}{{q_\infty}^2} \tag{C.21}$$

C.5 Mach Number

Also determined directly from pressure measurements, the formulation for Mach number must account for both the total and static pressure readings. Using Eq. 2.11, the uncertainty of the Mach number is as follows:

$$U_M = \sqrt{\left(\frac{\partial M}{\partial P_t} U_{P_t}\right)^2 + \left(\frac{\partial M}{\partial P} U_P\right)^2} \tag{C.22}$$

$$\frac{\partial M}{\partial P_t} = \frac{1}{\gamma P}\left(\frac{P_t}{P}\right)^{-1/\gamma}\left\{\frac{2}{\gamma - 1}\left[\left(\frac{P_t}{P}\right)^{\frac{\gamma-1}{\gamma}} - 1\right]\right\}^{-1/2} \tag{C.23}$$

$$\frac{\partial M}{\partial P} = -\frac{1}{\gamma P}\left(\frac{P_t}{P}\right)^{(\gamma-1)/\gamma}\left\{\frac{2}{\gamma - 1}\left[\left(\frac{P_t}{P}\right)^{\frac{\gamma-1}{\gamma}} - 1\right]\right\}^{-1/2} \tag{C.24}$$

C.6 Mass Flow Rate

In order to determine the mass flow rate through the measurement planes, the local density must first be determined through isentropic relations shown in Eq. 2.8. The uncertainty for this density is given below.

$$U_\rho = \sqrt{\left(\frac{\partial \rho}{\partial \rho_o} U_{\rho_o}\right)^2 + \left(\frac{\partial \rho}{\partial P} U_P\right)^2 + \left(\frac{\partial \rho}{\partial P_{amb}} U_{P_{amb}}\right)^2} \tag{C.25}$$

$$\frac{\partial \rho}{\partial \rho_o} = \left(\frac{P}{P_{amb}}\right)^{1/\gamma} \tag{C.26}$$

$$\frac{\partial \rho}{\partial P} = \frac{\rho_o}{\gamma P}\left(\frac{P}{P_{amb}}\right)^{1/\gamma} \tag{C.27}$$

$$\frac{\partial \rho}{\partial P_{amb}} = -\frac{\rho_o}{\gamma P_{amb}}\left(\frac{P}{P_{amb}}\right)^{1/\gamma} \tag{C.28}$$

Then, combining Eqs. 2.12 through 2.14 yields the relationship used to determine the local mass flow rate, as shown below, where the local cross sectional area is defined by the location of the probe within the annulus and the spacing of the measurement grid.

$$\dot{m}_i = M_i A_i \sqrt{\gamma \rho_i P_i} \tag{C.29}$$

Therefore, the uncertainty in mass flow rate can be determined by the following:

$$U_{\dot{m}_i} = \sqrt{\left(\frac{\partial \dot{m}_i}{\partial M} U_M\right)^2 + \left(\frac{\partial \dot{m}_i}{\partial \rho} U_\rho\right)^2 + \left(\frac{\partial \dot{m}_i}{\partial P} U_P\right)^2} \tag{C.30}$$

$$\frac{\partial \dot{m}_i}{\partial M} = A\sqrt{\gamma \rho P} \tag{C.31}$$

$$\frac{\partial \dot{m}_i}{\partial \rho} = \frac{MA}{2}\sqrt{\gamma \cdot \frac{P}{\rho}} \tag{C.32}$$

$$\frac{\partial \dot{m}_i}{\partial P} = \frac{MA}{2}\sqrt{\gamma \cdot \frac{\rho}{P}} \tag{C.33}$$

Because the mass flow rate is determined locally, the total mass flow is simply the summation of the individual values across the entire cross-section of the measurement plane. Therefore, the uncertainty of the total mass flow rate is simplified with the RSS formulation, as shown below, where n is the number of measured points in a given measurement plane.

$$U_{\dot{m}} = \sqrt{\sum_{i=1}^{n} U_{m_i}{}^2} \tag{C.34}$$

(The same RSS method can be used for the area-averaged values of pressure coefficient and Mach number, where $\dot{m}$ in Eq. C.34 above can be replaced by C_p, $P_{t,non}$, M, or any other variable requiring an area-average.)

C.7 Flow Direction

Using the calibration method outlined in Appendix B, the above procedure for determining uncertainty of flow direction predictions would be overly complex and time consuming due to the large number of calibration coefficients and flow variables calculated. Therefore, a "jitter" method developed by Moffat (and used by Zilliac for a seven-hole probe calibration) was incorporated into the computer-based calibration code.[34,35] The premise of the jitter method is to determine the contribution of uncertainty in a result from each of the independent variables by utilizing a repeating loop embedded in the overall calibration code. Fig. C.1 provides a flow diagram of the implementation of the jitter method.

Due to the complexity of the equations associated with the five-hole probe, this method was very useful in that it did not require analytical determinations of the partial derivatives for each of the independent variables. Instead, the uncertainty contribution of each variable was determined numerically using Eq. C.35, where Δx is very small, on the order of measurement uncertainties.

$$\frac{\partial R}{\partial x} = \frac{R_{x+\Delta x} - R_x}{\Delta x} \tag{C.35}$$

C.8 Sample Uncertainties

The following values are examples of uncertainties calculated for the vaned model configuration. Relative uncertainties are also provided in order to illustrate the magnitude of the uncertainties with respect to the measured values.

Table C.1 Sample uncertainties for variables utilized for general tunnel operation.

Variable	Reference Value	Absolute Uncertainty	Relative Uncertainty (%)
T_{amb}	528.3 R	±1.0 R	±0.1893
P_{amb}	14.287 psi	±0.008 psi	±0.0560
ρ_o	0.00227 slug/ft^3	±3.11 x 10^{-8} slug/ft^3	±0.0014
P_∞/P_{amb}	0.949	±0.0053	±0.5635
M_∞	0.275	±0.0023	±0.8539
q_∞	0.716 psi	±0.0122	±1.7087

Table C.2 Sample uncertainties for flow variables within MP1 near the 100-degree location.

Variable	Reference Value	Absolute Uncertainty	Relative Uncertainty (%)
C_p	-5.375	±0.1112	±2.0676
$P_{t,non}$	-5.841	±0.1017	±1.7411
M	0.705	±0.0012	±0.1746
ρ	0.00180 slug/ft^3	±1.31 x 10^{-6} slug/ft^3	±0.0727
$\dot{m}_i$	0.0039 lb$_m$/s	±5.49 x 10^{-6} lb$_m$/s	±0.1404

Table C.3 Sample uncertainties for area-averaged values within MP1.

Variable	Reference Value	Absolute Uncertainty	Relative Uncertainty (%)
$\dot{m}$	7.035 lb$_m$/s	±1.25 x 10^{-4} lb$_m$/s	±0.0018
M	0.607	±0.0007	±0.1188
$P_{t,non}$	-0.451	±0.0129	±2.8497

In addition to these values, uncertainties were also calculated for the five-hole probe measurements. Using the jitter method as portrayed in Fig. C.1, and the accuracy of the probe calibration procedure (see Fig. B.7), total errors in predicted flow angle within MP1 were determined to be approximately ±2.6 degrees and ±1.4 degrees in yaw and pitch, respectively. From these values, approximately 0.6 degrees were a direct result of the bias in the probe calibration, while the remainder of the uncertainty is due to random measurement errors. These uncertainties remained nearly constant across the entire measurement plane, regardless of the magnitude of the flow angularity. Therefore, in locations with small deviations from the axial direction, relative errors could be very large.

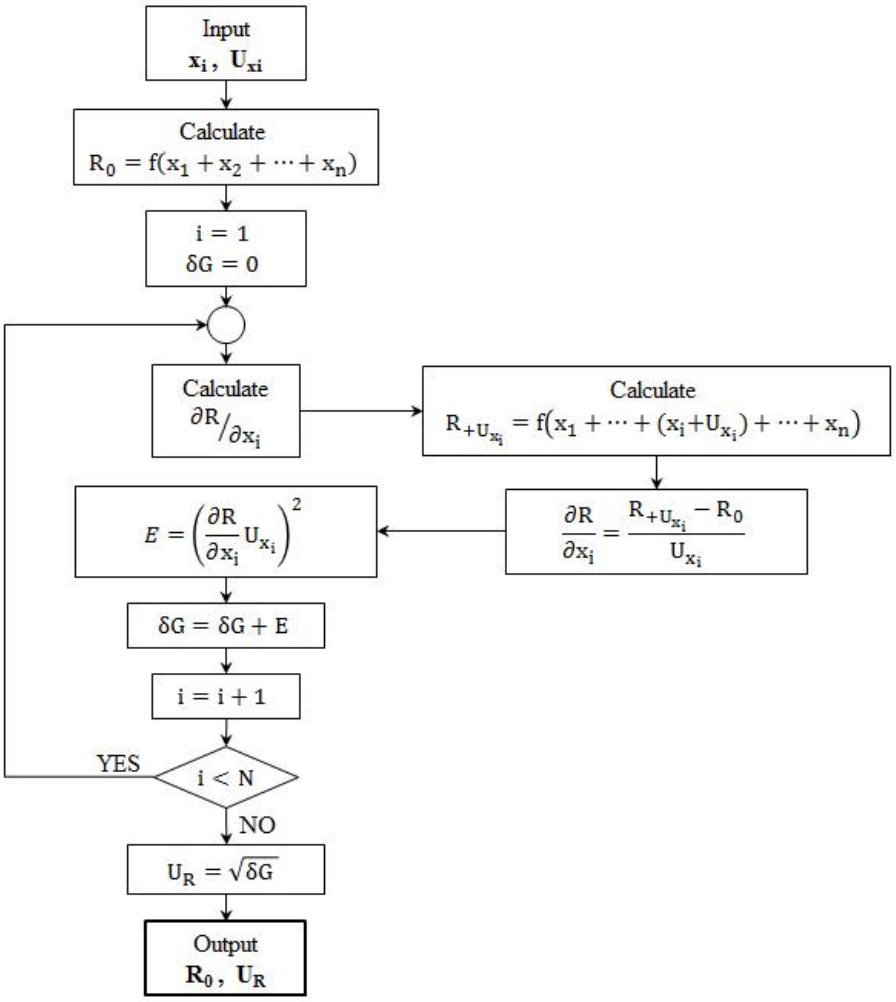

Fig. C.1 Flow diagram of the "jitter" uncertainty method. (Adapted from Moffat.[34])